

The Official Journal of the Chinese Stomatological Association (CSA)



# Chinese Journal of Dental Research

# CJDR

V  
O  
L  
U  
M  
E

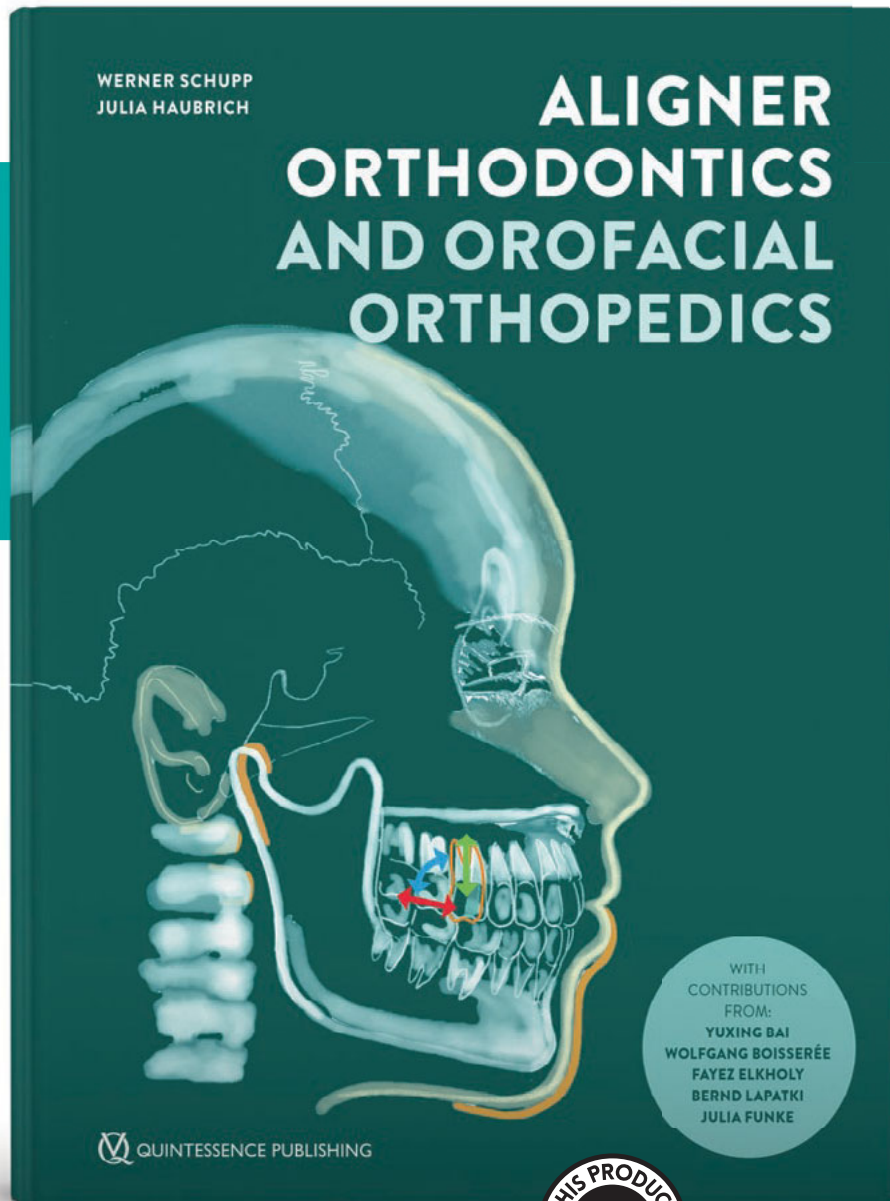
**26**

**2  
0  
2  
3**

N  
U  
M  
B  
E  
R

**2**

# USEFUL AND PRACTICAL MANUAL



Werner Schupp | Julia Haubrich

### Aligner Orthodontics and Orofacial Orthopedics

2nd Edition, 672 pages, 3,500 illus  
ISBN 978-1-78698-106-6  
€248

This book presents useful tips and strategies on how to integrate aligner orthodontics successfully into clinical practice, whether outsourced or with in-office aligner treatment. This second edition sees the authors review the diagnostic protocols and the biomechanics of aligners before presenting aligner orthodontics protocols. Supported by accompanying case documentation, the discussion of each malocclusion includes information on the associated symptoms, the rationale behind the selected treatment approaches, and the various outcomes achieved. The separation into sections on each malocclusion helps patients and clinicians in deciding whether this system can provide optimal treatment outcomes for a particular clinical situation. This is a practical manual for any clinician interested in the treatment modality of aligner orthodontics.



[www.quint.link/aligner](http://www.quint.link/aligner)



[books@quintessenz.de](mailto:books@quintessenz.de)



+49 (0)30 761 80 667

QUINTESSENZ PUBLISHING



# Chinese Journal of Dental Research

The Official Journal of the Chinese Stomatological Association (CSA)





# Chinese Journal of Dental Research

The Official Journal of the Chinese Stomatological Association (CSA)

## Original article

- 69 Small Molecule Nitazoxanide Inhibits Osteogenic Differentiation and Promotes Adipogenic Differentiation of Bone Marrow Mesenchymal Stem Cells  
Chan Yuan JIN, Yan Yan GUO, Xiao Mei HOU, Zhi Hui TANG
- 77 Complications and Peri-operative Characteristics of Flaps for Reconstruction of Defects after Ablation of Squamous Cell Carcinoma of the Floor of the Mouth  
Qu DENG, Qiu Sheng XU, Xu Hui ZHANG, Jing Chan XIE, Yi Fang ZHAO, Yan Ping HU, Jun JIA
- 83 Quantitative Assessment of Dimensional Evaluation and Artefacts from Filling Materials with CBCT Using Standard Phantom Roots  
Xiao Bo CHEN, Zhe Jun WANG, Ya SHEN, Andrea ESTEVES, He LIU, Gui Bin HUANG, Xiao Yan WANG, Lin YUE, Markus HAAPASALO
- 93 Evolutionary and Pan-genome Analysis of Three Important Black-pigmented Periodontal Pathogens  
Pei Qi MENG, Qian ZHANG, Yun DING, Jiu Xiang LIN, Feng CHEN
- 105 Application Value of 64-slice Multidetector Spiral CT Contrast-enhanced Scan in Maxillofacial Soft Tissue Hypervascular Tumours  
Wen Xin ZHANG, Seyiti PAKEZHATI, Shu LIU, Xiao Feng HUANG, Guo Wen SUN, Tie Mei WANG

## Case report

- 113 Novel Digital Mouth Preparation Technique for Fabricating Implant-Retained Removable Partial Dentures with Distal Extension: a Case Report  
Wan Rong WANG, Rui XIE, Li Na NIU, Zhi Hong FENG, Yi Min ZHAO



# Chinese Journal of Dental Research

CN 10-1194/R • ISSN 1462-6446 • eISSN 1867-5646 • Quarterly

The Official Journal of the Chinese Stomatological Association

Co-sponsor: Peking University School of Stomatology, Quintessenz Verlag

## Editor-in-Chief

**Chuan Bin GUO** Beijing, P.R. China

## Chief-Editor Emeritus

**Zhen Kang ZHANG** Beijing, P.R. China  
**Xing WANG** Beijing, P.R. China  
**Xu Chen MA** Beijing, P.R. China  
**Guang Yan YU** Beijing, P.R. China  
**Xue Dong ZHOU** Chengdu, P.R. China

## Executive Associate Editor

**Qian Ming CHEN** Hangzhou, P.R. China

## Executive Editors

**Ye Hua GAN** Beijing, P.R. China  
**Hong Wei LIU** Beijing, P.R. China

## Associate Editors

**Li Juan BAI** Beijing, P.R. China  
**Zhuan BIAN** Wuhan, P.R. China  
**Fa Ming CHEN** Xi'an, P.R. China  
**Bin CHENG** Guangzhou, P.R. China  
**Xu Liang DENG** Beijing, P.R. China  
**Xin Quan JIANG** Shanghai, P.R. China  
**Tie Jun LI** Beijing, P.R. China  
**Hong Chen SUN** Changchun, P.R. China  
**Song Ling WANG** Beijing, P.R. China  
**Ling YE** Chengdu, P.R. China  
**Zhi Yuan ZHANG** Shanghai, P.R. China  
**Yi Min ZHAO** Xi'an, P.R. China  
**Yong Sheng ZHOU** Beijing, P.R. China

## Editorial Board

**Tomas ALBREKTSSON** Gothenburg, Sweden  
**Conrado APARICIO** Barcelona, Spain  
**Daniele BOTTICELLI** Rimini, Italy  
**Lorenzo BRESCHI** Bologna, Italy  
**Francesco CAIRO** Florence, Italy  
**Tong CAO** Singapore  
**Jack G. CATON** Rochester, USA  
**Yang CHAI** Los Angeles, USA  
**Wan Tao CHEN** Shanghai, P.R. China  
**Zhi CHEN** Wuhan, P.R. China  
**Bruno CHRCANOVIC** Malmö, Sweden  
**Kazuhiro ETO** Tokyo, Japan  
**Bing FAN** Wuhan, P.R. China  
**Zhi Peng FAN** Beijing, P.R. China  
**Alfio FERLITO** Udine, Italy  
**Roland FRANKENBERGER** Marburg, Germany

**Xue Jun GAO** Beijing, P.R. China  
**Sufyan GAROUSHI** Turku, Finland  
**Reinhard GRUBER** Vienna, Austria  
**Gaetano ISOLA** Catania, Italy  
**Søren JEPSEN** Bonn, Germany  
**Li Jian JIN** Hong Kong SAR, P.R. China  
**Yan JIN** Xi'an, P.R. China  
**Newell W. JOHNSON** Queensland, Australia  
**Thomas KOCHER** Greifswald, Germany  
**Ralf-Joachim KOHAL** Freiburg, Germany  
**Niklaus P. LANG** Bern, Switzerland  
**Junying LI** Ann Arbor, USA  
**Yi Hong LI** New York, USA  
**Wei LI** Chengdu, P.R. China  
**Huan Cai LIN** Guangzhou, P.R. China  
**Yun Feng LIN** Chengdu, P.R. China

**Hong Chen LIU** Beijing, P.R. China  
**Yi LIU** Beijing, P.R. China  
**Edward Chin-Man LO** Hong Kong SAR, P.R. China  
**Jeremy MAO** New York, USA  
**Tatjana MARAVIC** Bologna, Italy  
**Claudia MAZZITELLI** Bologna, Italy  
**Mark MCGURK** London, UK  
**Li Na NIU** Xi'an, P.R. China  
**Jan OLSSON** Gothenburg, Sweden  
**Gaetano PAOLONE** Milan, Italy  
**No-Hee PARK** Los Angeles, USA  
**Peter POLVERINI** Ann Arbor, USA  
**Lakshman SAMARANAYAKE** Hong Kong SAR, P.R. China  
**Keiichi SASAKI** Miyagi, Japan  
**Zheng Jun SHANG** Wuhan, P.R. China  
**Song SHEN** Beijing, P.R. China

**Song Tao SHI** Guangzhou, P.R. China  
**Richard J. SIMONSEN** Downers Grove, USA  
**Manoel Damião de SOUSA-NETO** Ribeirão Preto, Brazil  
**John STAMM** Chapel Hill, USA  
**Lin TAO** Chicago, USA  
**Tiziano TESTORI** Ann Arbor, USA  
**Cun Yu WANG** Los Angeles, USA  
**Hom-Lay WANG** Ann Arbor, USA  
**Zuo Lin WANG** Shanghai, P.R. China  
**Heiner WEBER** Tuebingen, Germany  
**Xi WEI** Guangzhou, P.R. China  
**Yan WEI** Beijing, P.R. China  
**Ray WILLIAMS** Chapel Hill, USA  
**Jie YANG** Philadelphia, USA  
**Quan YUAN** Chengdu, P.R. China  
**Jia Wei ZHENG** Shanghai, P.R. China

## Publication Department

**Production Manager:** Megan Platt (London, UK)  
**Managing Editor:** Xiao Xia ZHANG (Beijing, P.R. China)

**Address:** 4F, Tower C, Jia 18#, Zhongguancun South Avenue, HaiDian District, 100081, Beijing, P.R. China.  
**Tel:** 86 10 82195785, **Fax:** 86 10 62173402  
**Email:** editor@cjdrcsa.com

**Manuscript submission:** Information can be found on the Guidelines for Authors page in this issue. To submit your outstanding research results more quickly, please visit: <http://mc03.manuscriptcentral.com/cjdr>

**Administrated by:** China Association for Science and Technology

**Sponsored by:** Chinese Stomatological Association and Popular Science Press

**Published by:** Popular Science Press

**Printed by:** Beijing ARTRON Colour Printing Co Ltd

**Subscription (domestically)** by Post Office

Chinese Journal of Dental Research is indexed in MEDLINE.

For more information and to download the free full text of the issue, please visit [www.quint.link/cjdr](http://www.quint.link/cjdr)  
<http://www.cjdrcsa.com>

# Acknowledgements

We would like to express our gratitude to the peer reviewers for their great support to the journal in 2022.

|  |                                     |                                   |
|--|-------------------------------------|-----------------------------------|
| Abi Rached-Junior, Fuad Jacob (Brazil)   | Hajeer, Mohammad Y. (Syrian Arab)   | Özel, Şelale (Turkiye)            |
| Al-Nuaimi, Nassr (United States)         | Hou, Ben Xiang (China)              | Pan, Shao Xia (China)             |
| Ashour, Hossam M. (United States)        | Huang, Ding Ming (China)            | Pertek Hatipoglu, Fatma (Turkiye) |
| Baeza, Mauricio (Chile)                  | Huang, Xiao Bin (United States)     | Piagkou, M. (Greece)              |
| Banoon, Shaima (Iraq)                    | Huang, Xiao Jing (China)            | Pradies, Guillermo (Spain)        |
| Baraka, Osama (Egypt)                    | Jiang, Xin Quan (China)             | Rong, Qi Guo (China)              |
| Benson, Philip E. (United Kingdom)       | Jin, Zuo Lin (China)                | Saito, Hanae (United States)      |
| Bolbolian, Marjan (Iran)                 | Kau, Chung How (United States)      | Sarialioglu Gungor, Ayça (Turkey) |
| Bulut, Sule (Turkiye)                    | Kavitha G. (India)                  | Shao, Jin Long (China)            |
| Cai, Zhi Gang (China)                    | Kou, Xiao Xing (China)              | Si, Yan (China)                   |
| Canullo, Luigi (Switzerland)             | Kurtulmus-Yilmaz, Sevcan (Turkiye)  | Silva, Erick Ricardo (Brazil)     |
| Cao, Huojun (United States)              | Lai, Wen Li (China)                 | Sun, Yu Chun (China)              |
| Chen, Fa Ming (China)                    | Lapinska, Barbara (Poland)          | Tallarico, Marco (Italy)          |
| Chen, Feng (China)                       | Lee, Jong-Ho (Korea)                | Tosun, Büsra (Turkiye)            |
| Chen, Ji Hua (China)                     | Li, Gang (China)                    | Tzanetakakis, Giorgos N. (Greece) |
| Chen, Peng (China)                       | Li, Guo Ju (China)                  | Uzunoglu-Ozyurek, Emel (Turkey)   |
| Cheng, Yong (China)                      | Li, Tie Jun (China)                 | Wang, Chin-Wei (United States)    |
| Chrcanovic, Bruno Ramos (Sweden)         | Li, Xuefeng (United States)         | Wang, Chun Xiao (China)           |
| Clark, Wendy Auclair (United States)     | Li, Ze Han (China)                  | Wang, Xiao Yan (China)            |
| Contreras, Adolfo (Colombia)             | Li, Zhi Min (China)                 | Wang, Yi Xiang (China)            |
| Dede, Dogu Omur (Turkiye)                | Liu, Da Wei (China)                 | Xie, Hai Feng (China)             |
| Deng, Peng (United States)               | Liu, Deng Gao (China)               | Xu, Li (China)                    |
| Deng, Xu Liang (China)                   | Liu, Xue Nan (China)                | Xu, Tian Min (China)              |
| Du, Rennan Yanlin (China)                | Liu, Yan (China)                    | Yang, Jie (United States)         |
| El-Abd, Mohammed (Kuwait)                | Liu, Yao (China)                    | Yang, Yan Qi (China)              |
| Erdemir, Uğur (Turkiye)                  | Luan, Qing Xian (China)             | Yu, Xi Jiao (China)               |
| Fan, Yuan (China)                        | Mashyakhy, M (Saudi Arabia)         | Zhang, Cheng Fei (China)          |
| Fang, Bing (China)                       | Mei, Lei (China)                    | Zhang, Lei (China)                |
| Faustino-Silva, Daniel Demetrio (Brazil) | Meng, Jia Lin (China)               | Zhang, Lei (China)                |
| Gao, Xue Jun (China)                     | Menini, Maria (Italy)               | Zhang, Ling Lin (China)           |
| Gao, Xue Mei (China)                     | Micheline, Daniela (United Kingdom) | Zhang, Wei Guang (China)          |
| Gao, You Shui (China)                    | Niu, Li Na (China)                  | Zhao, Irene Shuping (China)       |
| Gu, Yan (China)                          | Ocak, Mevlüt Sinan (Turkiye)        | Zheng, Ning Bo (China)            |
|  | Oktay, Husamettin (Turkiye)         | Zheng, Shu Guo (China)            |
|  |                                     | Zhou, Shuang Ying (China)         |

Editorial Office  
*Chinese Journal of Dental Research*



# Small Molecule Nitazoxanide Inhibits Osteogenic Differentiation and Promotes Adipogenic Differentiation of Bone Marrow Mesenchymal Stem Cells

Chan Yuan JIN<sup>1#</sup>, Yan Yan GUO<sup>1#</sup>, Xiao Mei HOU<sup>1</sup>, Zhi Hui TANG<sup>1</sup>

**Objective:** To investigate the potential effect of small molecule nitazoxanide (NTZ) on the osteogenic and adipogenic differentiation of bone marrow mesenchymal stem cells (BMSCs).

**Methods:** Cell counting Kit-8 assay was used to examine the effect of NTZ on proliferation of BMSCs. Quantitative reverse transcription polymerase chain reaction (qRT-PCR) and Western blot analysis were used to measure the expression of osteogenic and adipogenic marker gene. Alkaline phosphatase (ALP) staining and activity assay and Alizarin Red S (ARS) staining were used to investigate the effect of NTZ on osteogenesis. Oil red O (ORO) staining assay was used to assess the impact of NTZ on adipogenesis.

**Results:** NTZ significantly suppressed the osteogenic differentiation but promoted the adipogenic differentiation of BMSCs. Mechanistically, NTZ regulated osteogenic/adipogenic differentiation of BMSCs by inhibiting the Wnt/ $\beta$ -catenin signalling pathway. The addition of Wnt/ $\beta$ -catenin signalling pathway activator, lithium chloride, could reverse the effect of NTZ on BMSCs.

**Conclusion:** NTZ affected osteogenic and adipogenic differentiation of BMSCs with the involvement of Wnt/ $\beta$ -catenin signalling pathway. This finding expanded the understanding of NTZ pharmacology and indicated that NTZ might have an adverse effect on bone homeostasis.

**Key words:** adipogenesis, bone marrow mesenchymal stem cells, nitazoxanide, osteogenesis, Wnt/ $\beta$ -catenin pathway

*Chin J Dent Res* 2023;26(2):69–75; doi: 10.3290/j.cjdr.b4128019

In recent years, monoclonal antibodies, small molecule drugs and nanozymes have attracted widespread attention from scientific researchers and clinicians due to their broad application prospects in targeted therapies<sup>1-8</sup>. Small molecule nitazoxanide or 2-(acetyloxy)-N-(5-nitro-2-thiazolyl) benzamide, usually shortened to NTZ, was first successfully synthesized in the 1970s and initially used as an antiparasitic drug for intestinal protozoa and helminths<sup>9-11</sup>. Since the late 1990s, NTZ has been found to have antiviral activity against a brand range of both RNA and DNA viruses, includ-

ing coronaviruses, hepatitis B virus (HBV), influenza and other viruses<sup>12-14</sup>. Recently, NTZ was found to exhibit efficient antiviral activity against severe acute respiratory syndrome coronavirus 2 (SARS-CoV-2), a pandemic RNA virus belonging to the genera of betacoronaviridae. Many studies have demonstrated that NTZ, an FDA approved, safe and inexpensive old drug, has great application potential for repurposing against coronavirus disease 2019 (COVID-19)<sup>15-17</sup>. Many small molecule drugs have been found to have an effect on differentiation of bone marrow mesenchymal stem cells (BMSCs)<sup>18</sup>. Our research group previously found the small molecule anti-inflammatory drug sulfasalazine could promote osteogenic differentiation of BMSCs<sup>19</sup>; however, it is unclear whether NTZ affects osteogenic and adipogenic differentiation of BMSCs.

BMSCs are multipotent cells that have the potential to differentiate into various kinds of cell types, for example osteoblasts, adipocytes, chondrocytes and myoblasts<sup>20-23</sup>. Normally, there is a reciprocal balance between adipogenesis and osteogenesis, which is some-

1 Second Dental Center, Peking University School and Hospital of Stomatology, National Center for Stomatology, National Clinical Research Center for Oral Diseases, Beijing, P.R. China.

# These two authors contributed equally to this work.

**Corresponding authors:** Dr Xiao Mei HOU and Dr Zhi Hui TANG, The Second Clinical Division of Peking University School and Hospital of Stomatology, B5 Anli Garden, #66 Anli Road, Chao Yang District, Beijing 100101, P.R. China. Tel: 86-10-82196299; Fax: 86-10-64907970. Email: houxiaomei1108@163.com; tang\_zhihui@live.cn

times disrupted in various human disorders including osteoporosis and obesity<sup>24-28</sup>. Numerous studies have shown that complex signalling pathways, including the Wnt/ $\beta$ -catenin and Hedgehog signalling pathways, were involved in regulating the osteogenic and adipogenic differentiation of BMSCs<sup>29-33</sup>. The Wnt/ $\beta$ -catenin signalling pathway has been found to promote osteogenic differentiation of BMSCs and plays a crucial role in bone homeostasis. It is activated when the Wnt ligands bind to the cell surface receptors and induces the accumulation of  $\beta$ -catenin in the cytoplasm and its final translocation into the nucleus. Consequently,  $\beta$ -catenin interacts with T-cell factor/lymphoid enhancing factor (TCF/LEF) to upregulate the expression of various target genes<sup>34,35</sup>.

In the present study, we investigated the effects of NTZ on the osteogenic/adipogenic differentiation of BMSCs in vitro and suggested the potential effect of NTZ on bone health.

## Materials and methods

### *Cell culture and reagent treatment*

BMSCs were obtained from ScienCell Research Laboratories (Carlsbad, CA, USA). The proliferation medium (PM) consisted of Dulbecco's Modified Eagle Medium (DMEM), supplemented with 10% foetal bovine serum and 1% penicillin/streptomycin (all from Gibco, Grand Island, NY, USA), in a humidified incubator with an atmosphere containing 5% CO<sub>2</sub> at 37°C. The osteogenic medium (OM) was composed of PM supplemented with 100 nM dexamethasone, 0.2 mM ascorbic acid and 10 mM  $\beta$ -glycerophosphate (all from Sigma, St Louis, MO, USA). Similarly, adipogenic medium (AM) was composed of standard PM supplemented with 50 nM insulin, 100 nM dexamethasone, 0.5 mM 3-isobutyl-1-methylxanthine and 200 mM indomethacin (all from Sigma). Lithium chloride (LiCl) (5 mmol/L) was used to activate Wnt/ $\beta$ -catenin signalling<sup>36</sup>. The medium was refreshed every 2 days. All cell-based experiments were performed more than three times.

### *Cell counting kit-8 (CCK8) assay*

Once 80% confluence had been achieved, BMSCs were seeded in 96-well plates, then the plates were incubated in an incubator with standard culture conditions (37°C, 5% CO<sub>2</sub> and 95% humidity) for 24 hours. Afterwards, they were treated with NTZ (0, 1, 10, 20 or 50  $\mu$ M) in the presence of PM for 48 hours. The medium was replaced with fresh DMEM supplemented with 10% CCK8 solu-

tion (Bioscience, Shanghai, China), then the absorbance values at a wavelength of 450 nm were detected with the microplate reader (Bio-Rad, Hercules, CA, USA). 10  $\mu$ M of NTZ was used in the following experiment.

### *RNA extraction and quantitative reverse transcription polymerase chain reaction (qRT-PCR) analysis*

Total RNA was isolated from cells using TRIZOL reagent (Invitrogen, Carlsbad, CA, USA), and complementary DNA (cDNA) was synthesised using PrimeScript RT (Reagent Kit Takara, Tokyo, Japan). qRT-PCR was carried out in a 7500 Real-Time PCR assay system (Applied Biosystems, Foster City, CA, USA) with SYBR Green Master Mix (Roche Applied Science, Mannheim, Germany). The thermal cycling conditions were 95°C for 10 minutes, followed by 40 cycles of 95°C for 15 seconds and 60°C for 1 minute. Glyceraldehyde-3-phosphate dehydrogenase (GAPDH) was used as the internal control for the relative mRNA expression levels of target genes. The data was analysed using the 2<sup>- $\Delta\Delta$ Ct</sup> method. The primer sequences used were as follows: GAPDH, (F) GGTCAC-CAGGGCTGCTTTTA, (R) GGATCTCGCTCTGGAAGATG; ALP, (F) ATGGGATGGGTGTCTCCACA, (R) CCACGAA-GGGGAAGCTTGTGTC; RUNX2, (F) CCGCCTCAGTGATT-TAGGGC, (R) GGGTCTGTAATCTGACTCTGTCC; PPAR $\gamma$ , (F) GAGGAGCCTAAGGTAAGGAG, (R) GTCATTTTCGT-TAAAGGCTGA.

### *Alkaline phosphatase (ALP) staining and activity*

After a 7-day culture in PM or OM, the medium was removed. Cells were washed with 1 $\times$  PBS and fixed with 4% paraformaldehyde for 10 minutes at room temperature, followed by incubation with a 5-bromo-4-chloro-3-indolylphosphate/nitro-blue-tetrazolium (BCIP/NBT) staining kit (CW BIO, Beijing, China) solution according to the instructions. The stained cells were observed under an inverted fluorescence microscope (Olympus, Tokyo, Japan).

ALP activity assay was conducted using the ALP Activity Kit (Biovision, Milpitas, CA, USA). The total protein of cells was determined with the BCA method using a Pierce protein assay kit (Thermo Fisher Scientific, Waltham, MA, USA). Finally, the absorbance values at 520 nm were determined using a spectrophotometry reader and normalised to the total protein content.

### *ARS staining and quantification*

After a 14-day culture in PM or OM, cells were washed with 1 $\times$  PBS, fixed with 4% paraformaldehyde for 10

minutes and rinsed with distilled water. After that, cells were stained with 1% ARS solution (Sigma) for 20 minutes at room temperature and images were acquired using a scanner. For ARS quantification, the cells were destained with cetyl-pyridinium chloride (Sigma), then absorbance was measured with a spectrophotometer at 570 nm.

### ORO staining and quantification

After a 14-day culture in PM or AM, cells were washed three times with 1× PBS, fixed for 10 minutes in 4% paraformaldehyde and rinsed with 60% isopropyl alcohol. ORO (Sigma) staining solution was then added to each well for 10 minutes at room temperature. The lipid droplets of cells were observed and imaged under a microscope. For quantitative assessment, they were eluted with 100% isopropyl alcohol and measured with a spectrophotometer at 520 nm.

### Western blot analysis

Cells were harvested, lysed and extracted in the ice-cold radio immunoprecipitation assay (RIPA) lysis buffer (HuaxingBio Science, Beijing, China) with 1:100 volume of PMSF (Sigma). The Pierce BCA protein assay kit was then used to measure the concentrations of the protein samples. Next, equal amounts of total protein from each sample were separated on a 10% sodium dodecyl sulfate polyacrylamide gel electrophoresis (SDS-PAGE) and transferred onto polyvinylidene fluoride (PVDF) membranes (Millipore, Billerica, MA, USA), then the membranes were blocked with fat-free milk in TBST for 60 minutes at room temperature and incubated overnight at 4°C with primary antibodies against  $\beta$ -catenin (1:2000) (Cell Signaling Technology, Beverly, MA, USA), and GAPDH (1:5000) (HuaxingBio Science). After washing three times with TBST, the membranes were incubated with secondary antibodies (HuaxingBio Science) for 60 minutes at room temperature. The immunoreactive bands were detected using the ECL Western Blot Kit (CoWin Biotech, Beijing, China) and the intensity was quantified with ImageJ analysis software (National Institutes of Health, Bethesda, MD, USA).

### Statistical analysis

All statistical analyses were performed using SPSS version 23.0 (SPSS, Chicago, IL, USA). Comparisons between two groups were analysed with independent two-tailed Student *t* tests, and comparisons among three or more groups were analysed using a one-way analysis of vari-

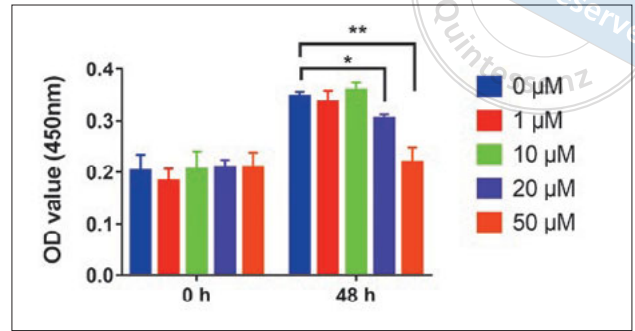


**Fig 1** The effect of NTZ on the proliferation of BMSCs. The cell proliferation curve was observed by CCK8 assay. BMSCs were treated with various concentrations (0, 1, 10, 20 and 50  $\mu$ M) of NTZ for 48 hours. The results were presented as mean  $\pm$  SD (\* $P$  < 0.05, \*\* $P$  < 0.01 compared with 0  $\mu$ M).

ance. Data were expressed as mean  $\pm$  standard deviation (SD).  $P$  < 0.05 was considered statistically significant. All experiments were conducted independently at least three times.

## Results

### The effect of NTZ on cell proliferation of BMSCs

First, we investigated whether NTZ could affect the proliferation of BMSCs using CCK8 assay. BMSCs were treated with different concentrations of NTZ (0, 1, 10, 20 and 50  $\mu$ M) for 48 hours. As shown in Fig 1, NTZ at 20 and 50  $\mu$ M could cause a significant reduction in the proliferation of BMSCs.

### NTZ inhibited osteogenic differentiation of BMSCs

To elucidate whether NTZ has an impact on osteogenic differentiation of BMSCs, we added NTZ into the PM and OM. qRT-PCR showed that the mRNA expression levels of osteogenic marker genes RUNX family transcription factor 2 (RUNX2) and alkaline phosphatase (ALP) were markedly decreased after NTZ treatment (Figs 2a and b). In line with this, ALP and ARS staining demonstrated that NTZ reduced the mineral deposition significantly and inhibited the ALP activity of BMSCs (Figs 2c to f). All these data implied that NTZ suppressed the osteogenic differentiation of BMSCs.

### NTZ promoted adipogenic differentiation of BMSCs

In general, osteogenic and adipogenic differentiation are two reverse directions of differentiation in BMSCs. Next, we assessed the role of NTZ in adipogenic differen-

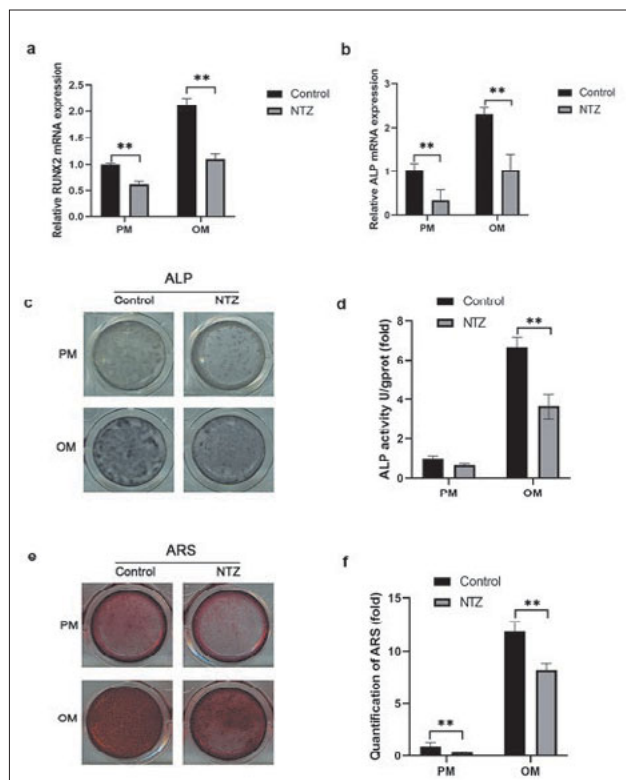


**Fig 2** NTZ suppressed osteogenic differentiation of BMSCs. Cells were treated with proliferation medium (PM) or osteogenic medium (OM) and NTZ (10  $\mu$ M) or DMSO (control) was added to the medium. **(a and b)** Relative mRNA expression levels of osteogenic markers (RUNX2 and ALP) were detected by qRT-PCR at day 5. **(c and d)** Representative images of ALP staining and quantification at day 7. **(e and f)** Representative images of ARS staining and quantification at day 14. The results were presented as mean  $\pm$  SD (\*\* $P$  < 0.01 compared with control).

tiation of BMSCs. As expected, qRT-PCR results showed that the mRNA level of adipogenic marker gene peroxisome proliferator activated receptor  $\gamma$  (PPAR $\gamma$ ) was markedly upregulated in the presence of NTZ (Fig 3a). In line with this result, ORO staining showed the lipid droplets were increased in the NTZ treated group (Figs 3b and c). Taken together, the results of qRT-PCR and ORO staining all suggested that NTZ has a positive effect on the adipogenic differentiation of BMSCs.

*NTZ regulated differentiation of BMSCs via the Wnt/ $\beta$ -catenin pathway*

Previous studies revealed that NTZ inhibited the Wnt/ $\beta$ -catenin signalling pathway in colorectal cancer cells. Thus, we hypothesised that NTZ regulated differentiation of BMSCs with the involvement of the Wnt/ $\beta$ -catenin signalling pathway. To confirm the mechanism, we first

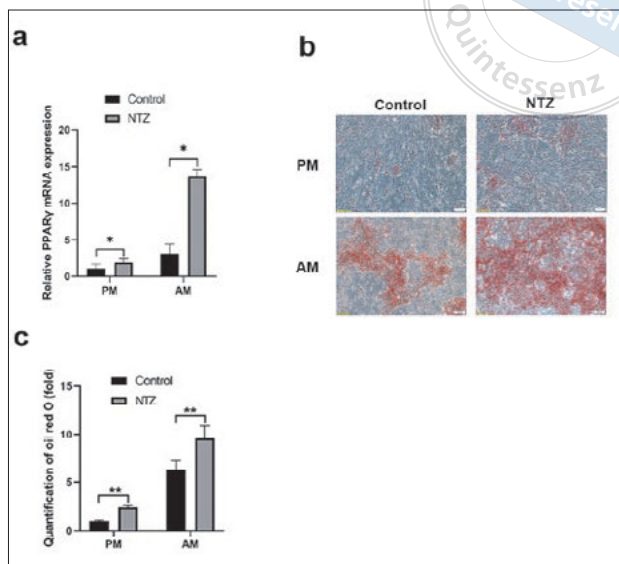


**Fig 3** NTZ promoted adipogenic differentiation of BMSCs. Cells were treated with PM or adipogenic medium (AM) and NTZ (10  $\mu$ M) or DMSO (control) was added to the medium. **(a)** Relative mRNA expression level of PPAR $\gamma$  was detected by qRT-PCR at day 5. **(b and c)** Representative images and quantification analysis of ORO staining at day 14. The results were presented as mean  $\pm$  SD (\* $P$  < 0.05, \*\* $P$  < 0.01 compared with control).

performed western blot analysis to detect the level of  $\beta$ -catenin after NTZ treatment. As shown in Figs 4a and b, the protein level of  $\beta$ -catenin was evidently down-regulated in the NTZ group compared with the control group. Since LiCl is a well-established inhibitor of glycogen synthase kinase-3 and widely used as an agonist to activate Wnt/ $\beta$ -catenin signalling, we treated the NTZ group with LiCl to recover the level of  $\beta$ -catenin. qRT-PCR analyses showed that the effect of NTZ on the expression of RUNX2, ALP and PPAR $\gamma$  was significantly restored by LiCl treatment (Figs 4c to e). Collectively, these results revealed that NTZ suppressed the osteogenic differentiation of BMSCs and promoted the adipogenic differentiation via the Wnt/ $\beta$ -catenin signalling pathway.

**Discussion**

Small molecule NTZ, a thiazolide antiparasitic agent, has been widely commercialised for treating parasitic infection. In recent years, researchers have identified the antiviral activity and antitumoural effect of NTZ. To date, NTZ has been reported to have some common adverse effects, such as diarrhoea, abdominal pain,

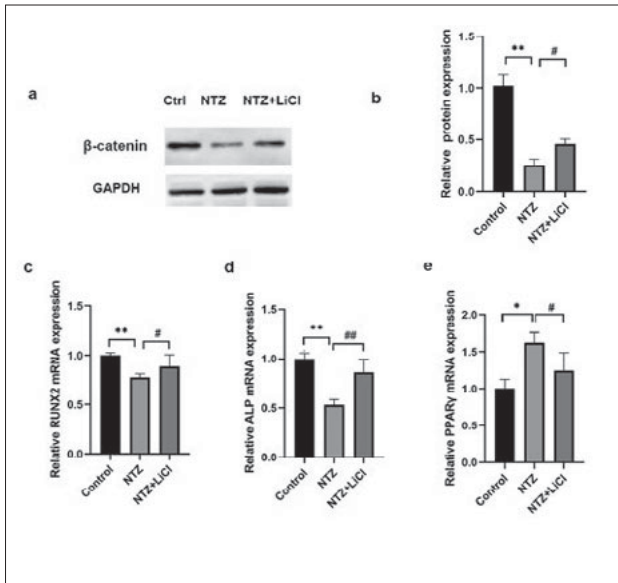


**Fig 4** NTZ regulated differentiation of BMSCs by targeting the Wnt/ $\beta$ -catenin pathway. **(a)** Immunoblot images showing the protein expression of  $\beta$ -catenin after NTZ (10  $\mu$ M) treatment or lithium chloride (LiCl) (5 mmol/L) treatment for 48 hours. DMSO was used as control group. Glyceraldehyde-3-phosphate dehydrogenase (GAPDH) was used as an internal control. **(b)** Quantification of **(a)**. **(c-e)** Relative mRNA expression levels of RUNX2, ALP and PPAR $\gamma$  were examined by qRT-PCR at day 5. The results were presented as mean  $\pm$  SD (\*/#P < 0.05, \*\*/##P < 0.01, \*compared with control, # compared with NTZ group).

headache and nausea<sup>37-42</sup>; however, its effect on BMSCs has not yet been reported.

Small molecule drugs refer to those drugs with a molecular weight  $\leq$  1000 Da. Recently, several small molecule drugs have been demonstrated to regulate osteogenic differentiation of BMSCs. For example, many studies have proved that the widely used cholesterol-lowering drug simvastatin promotes bone repair by upregulating BMP2 expression and activating osteogenesis-related pathways<sup>43</sup>. The conventional anticonvulsant drug valproic acid has recently been found to promote osteogenic differentiation of mesenchymal stem cells by inhibiting histone deacetylase<sup>44</sup>. The most commonly used antidiabetic drug metformin has also been discovered to promote osteogenic differentiation of rat bone marrow mesenchymal stem cells<sup>45</sup>. We wondered whether NTZ had an impact on osteogenic differentiation of BMSCs and performed a series of experiments. The results showed that NTZ negatively regulated osteogenic differentiation and upregulated adipogenic differentiation of BMSCs.

In this study, we found that NTZ regulated osteogenic and adipogenic differentiation through the Wnt/ $\beta$ -

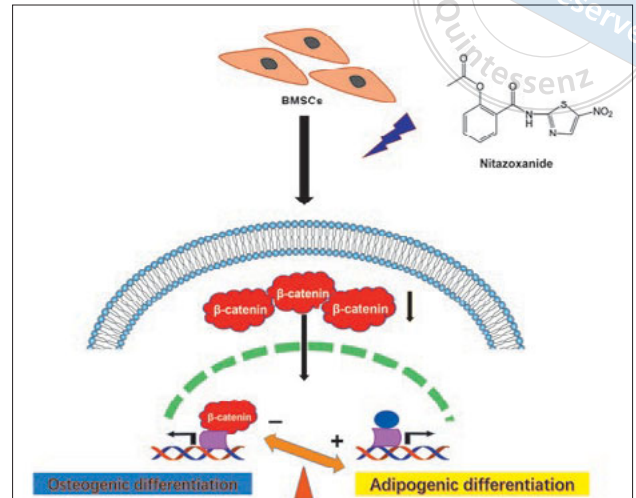


**Fig 5** Schematic diagram of the effect of NTZ on osteogenic and adipogenic differentiation of BMSCs

catenin signalling pathway; however, NTZ has been demonstrated to be able to regulate multiple signalling pathways. For example, Lü et al<sup>46</sup> found that NTZ inhibited the STAT3 pathway, Ye et al<sup>47</sup> found NTZ suppressed the AKT/mTOR pathway in osteosarcoma cells and Khan and Lee<sup>48</sup> revealed that NTZ might exert anti-hepatocellular carcinoma effects by affecting multiple signalling pathways, such as the MAPK signalling pathway. Thus, NTZ might regulate osteogenic and adipogenic differentiation via other signalling pathways. Besides, the effect of NTZ in vivo remains unclear. Further studies including animal experiments are required to clarify the effect and detailed mechanism of NTZ.

## Conclusion

In summary (as shown in Fig 5), we investigated the function of small molecular NTZ in BMSCs and found that NTZ inhibited the osteogenic differentiation and promoted the adipogenic differentiation of BMSCs by inhibiting the Wnt/ $\beta$ -catenin pathway, suggesting that NTZ could pose a potential risk for bone health.

## Conflicts of interest

The authors declare no conflicts of interest related to this study.

## Author contribution

Dr Chan Yuan JIN designed the research, performed the experiments, collected and analysed the data, and drafted and revised the manuscript; Dr Yan Yan GUO per-

formed the experiments, collected the data and drafted the manuscript; Drs Xiao Mei HOU and Zhi Hui TANG supervised the work.

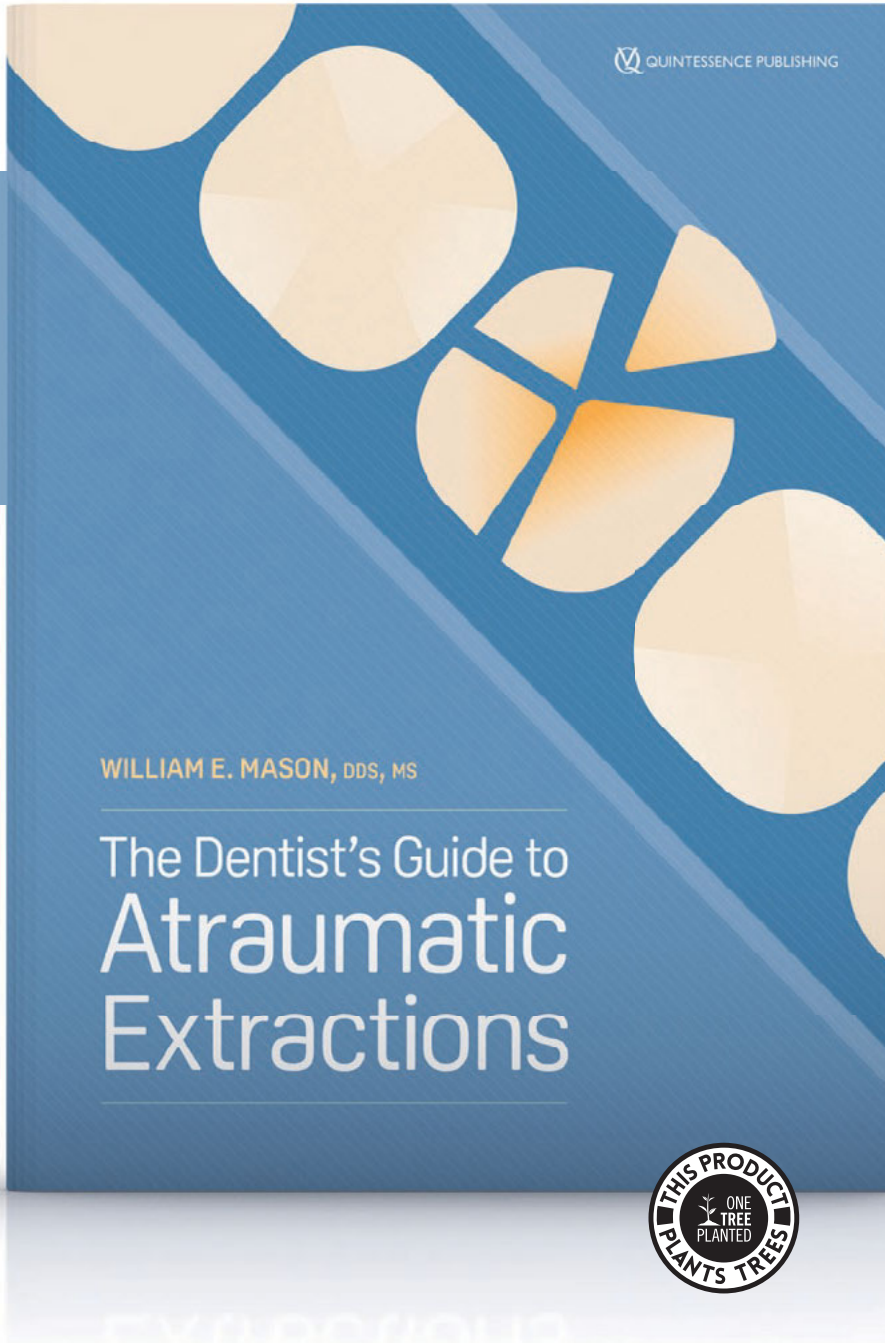
(Received Oct 13, 2022; accepted Mar 06, 2023)

## References

- Castelli MS, McGonigle P, Hornby PJ. The pharmacology and therapeutic applications of monoclonal antibodies. *Pharmacol Res Perspect* 2019;7:e00535.
- Zhuang ZC, Li YH, Yu RH, et al. Reversely trapping atoms from a perovskite surface for high-performance and durable fuel cell cathodes. *Nat Catal* 2022;5:300–310.
- Shi J, Shu R, Shi X, et al. Multi-activity cobalt ferrite/MXene nanoenzymes for drug-free phototherapy in bacterial infection treatment. *RSC Adv* 2022;12:11090–11099.
- Ji SF, Jiang B, Hao HG, et al. Matching the kinetics of natural enzymes with a single-atom iron nanozyme. *Nat Catal* 2021;4:407–417.
- Chen Y, Wang P, Hao H, et al. Thermal atomization of platinum nanoparticles into single atoms: An effective strategy for engineering high-performance nanozymes. *J Am Chem Soc* 2021;143:18643–18651.
- Zhang L, Qin Z, Sun H, et al. Nanoenzyme engineered neutrophil-derived exosomes attenuate joint injury in advanced rheumatoid arthritis via regulating inflammatory environment. *Bioact Mater* 2022;18:1–14.
- Liu ZH, Du Y, Zhang P, Zhuang Z, Wang D. Bringing catalytic order out of chaos with nitrogen-doped ordered mesoporous carbon. *Matter* 2021;4:3161–3194.
- Cheng G, Chen J, Wang Q, et al. Promoting osteogenic differentiation in pre-osteoblasts and reducing tibial fracture healing time using functional nanofibers. *Nano Res* 2018;11:3658–3677.
- Fahmy MA, Abdelaal AA, Hassan SI, et al. Antiparasitic and immunomodulating effects of nitazoxanide, ivermectin and selenium on *Cryptosporidium* infection in diabetic mice. *Rev Bras Parasitol Vet* 2021;30:e012121.
- Goel V, Jain A, Sharma G, et al. Evaluating the efficacy of nitazoxanide in uncomplicated amebic liver abscess. *Indian J Gastroenterol* 2021;40:272–280.
- Rosignol JF. Nitazoxanide: A first-in-class broad-spectrum antiviral agent. *Antiviral Res* 2014;110:94–103.
- Wang YM, Lu JW, Lin CC, et al. Antiviral activities of niclosamide and nitazoxanide against chikungunya virus entry and transmission. *Antiviral Res* 2016;135:81–90.
- Irabuena C, Scarone L, de Souza GE, et al. Synthesis and antiparasitic assessment of nitazoxanide and analogs as new antimalarial candidates. *Med Chem Res* 2022;31:426–435.
- Hickson SE, Margineantu D, Hockenbery DM, Simon JA, Geballe AP. Inhibition of vaccinia virus replication by nitazoxanide. *Virology* 2018;518:398–405.
- Riccio A, Santopolo S, Rossi A, Piacentini S, Rosignol JF, Santoro MG. Impairment of SARS-CoV-2 spike glycoprotein maturation and fusion activity by nitazoxanide: An effect independent of spike variants emergence. *Cell Mol Life Sci* 2022;79:227.
- Cadegiani FA, Goren A, Wambier CG, McCoy J. Early COVID-19 therapy with azithromycin plus nitazoxanide, ivermectin or hydroxychloroquine in outpatient settings significantly improved COVID-19 outcomes compared to known outcomes in untreated patients. *New Microbes New Infect* 2021;43:100915.
- Martins-Filho PR, Barreto-Alves JA, Fakhouri R. Potential role for nitazoxanide in treating SARS-CoV-2 infection. *Am J Physiol Lung Cell Mol Physiol* 2020;319:L35–L36.
- Mitchell J, Lo KWH. Small molecule-mediated regenerative engineering for craniofacial and dentoalveolar bone. *Front Bioeng Biotechnol* 2022;10:1003936.
- Jin C, Zhang P, Zhang M, et al. Inhibition of SLC7A11 by sulfasalazine enhances osteogenic differentiation of mesenchymal stem cells by modulating BMP2/4 expression and suppresses bone loss in ovariectomized mice. *J Bone Miner Res* 2017;32:508–521.
- He JY, Cheng M, Ye JL, et al. YY1-induced lncRNA XIST inhibits cartilage differentiation of BMSCs by binding with TAF15 to stabilizing FUT1 expression. *Regen Ther* 2022;20:41–50.
- Rehman FU, Zhao C, Wu C, et al. Synergy and translation of allogenic bone marrow stem cells after photodynamic treatment of rheumatoid arthritis with tetra sulfonatophenyl porphyrin and TiO<sub>2</sub> nanowhiskers. *Nano Res* 2016;9:3305–3321.
- Yu M, Lei B, Gao CB, et al. Optimizing surface-engineered ultra-small gold nanoparticles for highly efficient miRNA delivery to enhance osteogenic differentiation of bone mesenchymal stromal cells. *Nano Res* 2017;10:49–63.
- Xu C, Xiao L, Cao YX, et al. Mesoporous silica rods with cone shaped pores modulate inflammation and deliver BMP-2 for bone regeneration. *Nano Res* 2020;13:2323–2331.
- Kumar N, Saraber P, Ding Z, Kusumbe AP. Diversity of vascular niches in bones and joints during homeostasis, ageing, and diseases. *Front Immunol* 2021;12:798211.
- Zhang H, Xu R, Li B, et al. LncRNA NEAT1 controls the lineage fates of BMSCs during skeletal aging by impairing mitochondrial function and pluripotency maintenance. *Cell Death Differ* 2022;29:351–365.
- Yue R, Zhou BO, Shimada IS, Zhao Z, Morrison SJ. Leptin receptor promotes adipogenesis and reduces osteogenesis by regulating mesenchymal stromal cells in adult bone marrow. *Cell Stem Cell* 2016;18:782–796.
- Wang ZX, Luo ZW, Li FX, et al. Aged bone matrix-derived extracellular vesicles as a messenger for calcification paradox. *Nat Commun* 2022;13:1453.
- Lu L, Tang M, Li J, et al. Gut microbiota and serum metabolic signatures of high-fat-induced bone loss in mice. *Front Cell Infect Microbiol* 2021;11:788576.
- Yu LB, Xie MX, Zhang FJ, Wan C, Yao X. TM9SF4 is a novel regulator in lineage commitment of bone marrow mesenchymal stem cells to either osteoblasts or adipocytes. *Stem Cell Res Ther* 2021;12:573.
- Karadeniz F, Oh JH, Jo HJ, Seo Y, Kong CS. Myricetin 3-O- $\beta$ -D-galactopyranoside exhibits potential anti-osteoporotic properties in human bone marrow-derived mesenchymal stromal cells via stimulation of osteoblastogenesis and suppression of adipogenesis. *Cells* 2021;10:2690.
- Zhang YL, Liu L, Su YW, Xian CJ. miR-542-3p attenuates bone loss and marrow adiposity following methotrexate treatment by targeting sFRP-1 and Smurf2. *Int J Mol Sci* 2021;22:10988.
- Kim SP, Da H, Wang L, Taketo MM, Wan M, Riddle RC. Bone-derived sclerostin and Wnt/ $\beta$ -catenin signaling regulate PDGFR $\alpha$ + adipogenic cell differentiation. *FASEB J* 2021;35:e21957.
- Tang CY, Chen W, Luo Y, et al. Runx1 up-regulates chondrocyte to osteoblast lineage commitment and promotes bone formation by enhancing both chondrogenesis and osteogenesis. *Biochem J* 2020;477:2421–2438.
- Law SM, Zheng JJ. Premise and peril of Wnt signaling activation through GSK-3 $\beta$  inhibition. *iScience* 2022;25:104159.

35. Zhu Y, Wang YM, Jia YC, Xu J, Chai Y. Catalpol promotes the osteogenic differentiation of bone marrow mesenchymal stem cells via the Wnt/ $\beta$ -catenin pathway. *Stem Cell Res Ther* 2019;10:37.
36. Wang R, Gao D, Zhou Y, et al. High glucose impaired estrogen receptor alpha signaling via  $\beta$ -catenin in osteoblastic MC3T3-E1. *J Steroid Biochem Mol Biol* 2017;174:276–283.
37. Rakedzon S, Neuberger A, Domb AJ, Petersiel N, Schwartz E. From hydroxychloroquine to ivermectin: What are the antiviral properties of anti-parasitic drugs to combat SARS-CoV-2? *J Travel Med* 2021;28:taab005.
38. Custodio H. Protozoan parasites. *Pediatr Rev* 2016;37:59–71.
39. Shakya A, Bhat HR, Ghosh SK. Update on nitazoxanide: A multifunctional chemotherapeutic agent. *Curr Drug Discov Technol* 2018;15:201–213.
40. Walsh KF, McAulay K, Lee MH, et al. Early bactericidal activity trial of nitazoxanide for pulmonary tuberculosis. *Antimicrob Agents Chemother* 2020;64:e01956-19.
41. Kiehl IGA, Ricetto E, Salustiano ACC, et al. Boosting bladder cancer treatment by intravesical nitazoxanide and bacillus calmette-guérin association. *World J Urol* 2021;39:1187–1194.
42. Senkowski W, Zhang X, Olofsson MH, et al. Three-dimensional cell culture-based screening identifies the anthelmintic drug nitazoxanide as a candidate for treatment of colorectal cancer. *Mol Cancer Ther* 2015;14:1504–1516.
43. Jin H, Ji Y, Cui Y, Xu L, Liu H, Wang J. Simvastatin-incorporated drug delivery systems for bone regeneration. *ACS Biomater Sci Eng* 2021;7:2177–2191.
44. Yu Y, Oh SY, Kim HY, Choi JY, Jo SA, Jo I. Valproic acid-induced CCN1 promotes osteogenic differentiation by increasing CCN1 protein stability through HDAC1 inhibition in tonsil-derived mesenchymal stem cells. *Cells* 2022;11:534.
45. Dong K, Zhou WJ, Liu ZH. Metformin enhances the osteogenic activity of rat bone marrow mesenchymal stem cells by inhibiting oxidative stress induced by diabetes mellitus: An in vitro and in vivo study. *J Periodontal Implant Sci* 2023;53:54–68.
46. Lü Z, Li X, Li K, et al. Structure-activity study of nitazoxanide derivatives as novel STAT3 pathway inhibitors. *ACS Med Chem Lett* 2021;12:696–703.
47. Ye C, Wei M, Huang H, et al. Nitazoxanide inhibits osteosarcoma cells growth and metastasis by suppressing AKT/mTOR and Wnt/ $\beta$ -catenin signaling pathways. *Biol Chem* 2022;403:929–943.
48. Khan SA, Lee TKW. Investigations of nitazoxanide molecular targets and pathways for the treatment of hepatocellular carcinoma using network pharmacology and molecular docking. *Front Pharmacol* 2022;13:968148.

# METHODS, TOOLS, AND TIPS



William E. Mason

## The Dentist's Guide to Atraumatic Extractions

144 pages, 467 illus.

ISBN 978-1-64724-139-1

€88

Traditional methods of tooth extraction involve raising flaps and luxating the tooth to force it out of the bone. This often results in significant trauma and ridge resorption, which can compromise future implant placement. In this book, the author details his atraumatic extraction technique, which relies on systematic removal of root structure to protect the socket from deformation and thereby maintain the patient's original jaw anatomy and facial structure. With the root space creation extraction technique (RSCET), root structure is removed to allow space for the remaining tooth structure to be maneuvered and manipulated instead of pushed into the adjacent bony walls, thereby protecting the bone from trauma and resorption. Every tooth in the mouth can be removed atraumatically, and this book shows every step of the process and the tools required, including tips on atraumatic anesthesia.



[www.quint.link/extractions](http://www.quint.link/extractions)



[books@quintessenz.de](mailto:books@quintessenz.de)



+49 (0)30 761 80 667

 **QUINTESSENZ PUBLISHING**



# Complications and Peri-operative Characteristics of Flaps for Reconstruction of Defects after Ablation of Squamous Cell Carcinoma of the Floor of the Mouth

Qu DENG<sup>1,2</sup>, Qiu Sheng XU<sup>1,2</sup>, Xu Hui ZHANG<sup>2</sup>, Jing Chan XIE<sup>2</sup>, Yi Fang ZHAO<sup>1,3</sup>, Yan Ping HU<sup>2</sup>, Jun JIA<sup>1,3</sup>

**Objective:** To determine the appropriate method to use to repair defects after ablation of squamous cell carcinoma (SCC) of the floor of the mouth (FOM).

**Methods:** A retrospective review of 119 patients who underwent surgical resections of SCC of the FOM and flap reconstructions was conducted. A Student t test was used to examine the statistical differences in operative time, length of hospital stay and complications among groups with different reconstructions.

**Results:** Advanced-stage patients were repaired with more free flaps than local pedicled flaps that provided more reconstructions for small-to-medium defects. The most common recipient complication was wound dehiscence, and patients in the anterolateral thigh flap group developed a greater number of overall recipient site complications compared with those in other groups. Patients undergoing local flap reconstructions had shorter operative times compared with those with free flap reconstructions.

**Conclusion:** In contrast to a radial forearm free flap as a more appropriate reconstruction for defects involving the tongue, an anterolateral thigh flap was better suited for defects with dead spaces. A fibular flap was appropriate for massive complex defects involving the mandible, FOM and tongue. A pectoralis major musculocutaneous flap provided the last line of reconstruction for patients with relapsed SCC or high-risk factors for microsurgical reconstructions.

**Key words:** complication, flap, floor of the mouth, squamous cell carcinoma

*Chin J Dent Res* 2023;26(2):77–82; doi: 10.3290/j.cjdr.b4128013

Although considerable progress has been made with chemotherapy, radiotherapy and immunotherapy in recent decades, surgery remains the mainstay of multimodal treatment for oral squamous cell carcinoma (SCC)<sup>1-3</sup>; however, complete excision of tumours inevitably impairs not only patients' physiological function,

but also their psychosocial state<sup>4</sup>. To reduce postoperative impairment as much as possible, various flaps have been employed to repair defects after oral cancer ablation.

The floor of the mouth (FOM) is one of the subsites most frequently exposed to harmful toxicants, such as tobacco and alcohol, in the oral cavity. Thus, the FOM is a relatively common subsite for oral cancer, with approximately 10% of all oral cancers developing there<sup>5</sup>. Defects affecting the FOM need flaps that are able to preserve the local anatomy, repair physiological function and separate the oral cavity from the neck. The present study reports our experience with the use of flaps and sums up the relative characteristics in the reconstruction of defects in the FOM.

1 The State Key Laboratory Breeding Base of Basic Science of Stomatology (Hubei-MOST) and Key Laboratory for Oral Biomedicine Ministry of Education, Wuhan University; and Department of Oral Maxillofacial and Head Neck Oncology, School and Hospital of Stomatology, Wuhan University, Wuhan, P.R. China.

2 Department of Oral Surgery, Stomatological Hospital of Xiamen Medical College, Xiamen, P.R. China.

3 Department of Oral Maxillofacial-Head Neck Oncology, School and Hospital of Stomatology, Wuhan University, Wuhan, P.R. China.

**Corresponding author:** Dr Jun JIA, Department of Oral Maxillofacial-Head Neck Oncology, School and Hospital of Stomatology, Wuhan University, 237 Luoyu Road, Wuhan 430079, P.R. China. Tel: 86-27-87866129; Fax: 86-27-87873260. Email: junjia@whu.edu.cn

**Table 1** Comparison of patients with different types of flaps.

| Characteristics |                               | RFFF | ALTF | FF | PMMF | LF |
|-----------------|-------------------------------|------|------|----|------|----|
| Median age, y   |                               | 55   | 57   | 55 | 59   | 54 |
| Sex             | Total                         | 43   | 30   | 13 | 9    | 27 |
|                 | Male                          | 41   | 29   | 13 | 9    | 27 |
|                 | Female                        | 2    | 1    | 0  | 0    | 0  |
| Tumour stage    | T1 and T2                     | 37   | 20   | 5  | 1    | 26 |
|                 | T3 and T4                     | 6    | 10   | 8  | 8    | 1  |
| Prior treatment | Radiation therapy             | 0    | 0    | 0  | 1    | 0  |
|                 | Chemotherapy                  | 5    | 3    | 1  | 1    | 0  |
|                 | Surgery                       | 0    | 1    | 0  | 0    | 1  |
|                 | Radiation therapy and surgery | 0    | 0    | 0  | 5    | 0  |

ALTF, anterolateral thigh flap; FF, fibular flap; LF, local flap; PMMF, pectoralis major musculocutaneous flap; RFFF, radial forearm free flap.

## Materials and methods

### Data collection and analysis

The study was approved by the review board of the Ethics Committee of the School and Hospital of Stomatology of Wuhan University (No. 2019-B05). We conducted the study by selecting medical information of patients with SCC of the FOM who underwent surgery at the Department of Oral and Maxillofacial Surgery, Wuhan University, China, from January 2008 to December 2017. Patients with lesions that were closed directly were excluded. A total of 119 cases were identified. Information on patient characteristics, clinical and histopathological tumour characteristics, treatment modalities and complications was retrieved from the medical records (Table 1).

### Surgical intervention

For each patient, the choice of flap type was based on surgeon experience, defect size and patient characteristics, including body habitus, donor site suitability, comorbidity and preoperative treatment. The patients who agreed to reconstruction with free flaps were treated using a two-team approach and those who received reconstruction with local flaps were treated by a single attending surgeon.

### Data analysis

Operative time, length of hospital stay and complications were calculated between each group, and a Student *t* test was used to assess statistical differences.  $P < 0.05$  was considered significant. Statistical analysis was performed using SPSS version 16 (SPSS, Chicago, IL, USA).

## Results

### Patient demographics and tumour characteristics

A total of 119 patients received 122 flaps, with one patient receiving both a radial forearm free flap (RFFF) and fibular flap (FF) due to the absence of a cutaneous perforator of the FF. Two patients who had undergone their first reconstruction in our department and subsequently developed recurrent disease after a disease-free interval received a pectoralis major musculocutaneous flap (PMMF) as the secondary reconstruction: one had undergone an anterolateral thigh flap (ALTF) and the other a FF. The key points for the different reconstructive methods were the size, site of defects and surgeon experience after ablation of SCC of the FOM. Of the 122 reconstructions, local flaps (LF, 96%, 26/27) were mainly used for defects after ablation of T1 and T2 tumours, whereas large defects caused by T3 and T4 tumours (97%, 32/33) were reconstructed with free flaps. The choice of a free flap with T3 and T4 tumours depended on the defects in the FOM muscle group, with the first choice of flap with through-and-through defects being ALTF. Sixteen patients had received prior surgical and/or radiation therapy before reconstruction: seven (7/16, 44%) in the PMMF group, five (5/16, 31%) in the RFFF group and four (4/16, 25%) in the ALTF group. All five patients who had previously undergone radiotherapy were in the PMMF group.

### Perioperative and postoperative characteristics

Operative time and length of hospital stay are shown in Fig 1. The mean operative time for tumour resection, neck dissection and flap reconstruction was 7 hours and 50 minutes in the RFFF group, 8 hours and 25 minutes in the ALTF group, 9 hours and 53 minutes in the FF group, 9 hours and 3 minutes in the PMMF group, and 6

**Fig 1** Operative time and hospital stay days with various types of flaps. **(a)** There was a significant difference between the operative time of different flaps ( $P < 0.001$ ). **(b)** The length of hospital stay was shorter for the LF group than for the other groups, but the difference was not statistically significant.

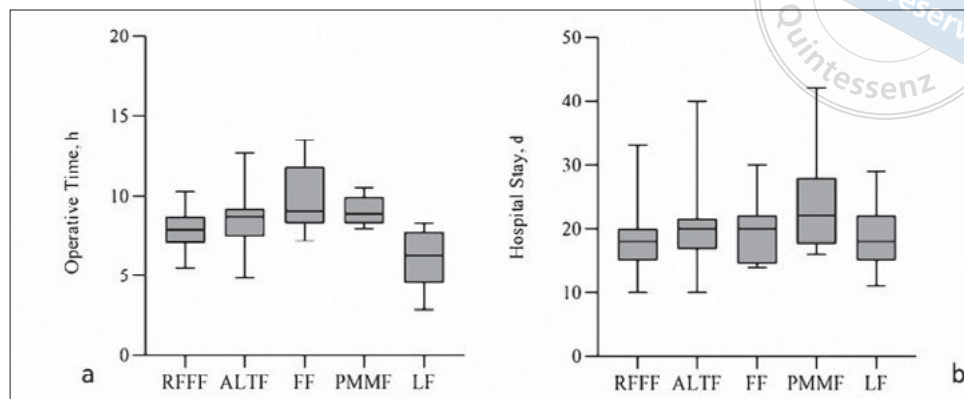


**Table 2** Complications in patients with various types of flaps.

| Complication                   | RFFF                       | ALTF | FF | PMMF | LF |   |
|--------------------------------|----------------------------|------|----|------|----|---|
| Flap-related complication      | Overall                    | 3    | 4  | 0    | 5  | 6 |
|                                | Partial necrosis           | 2    | 4  | 0    | 5  | 6 |
|                                | Venous thrombosis          | 1    | 0  | 0    | 0  | 0 |
| Recipient-related complication | Overall                    | 8    | 12 | 3    | 7  | 5 |
|                                | Orocutaneous fistula       | 0    | 1  | 0    | 1  | 1 |
|                                | Wound dehiscence           | 2    | 7  | 1    | 3  | 0 |
|                                | Hematoma                   | 1    | 1  | 1    | 1  | 1 |
|                                | Neck infection             | 5    | 2  | 1    | 1  | 3 |
|                                | Chylous fistula            | 0    | 1  | 0    | 1  | 0 |
| Donor site complication        | Overall                    | 7    | 0  | 2    | 0  | 0 |
|                                | Partial loss of skin graft | 2    | 0  | 0    | 0  | 0 |
|                                | Wound dehiscence           | 0    | 0  | 2    | 0  | 0 |
|                                | Delayed wound healing      | 2    | 0  | 0    | 0  | 0 |
| Medical-related complication   | Overall                    | 0    | 0  | 1    | 0  | 1 |
|                                | Pneumonia                  | 0    | 0  | 0    | 0  | 1 |
|                                | Pneumothorax               | 0    | 0  | 1    | 0  | 0 |

hours and 1 minute in the LF group. Compared with the patients in the free flap reconstruction group, patients undergoing LF reconstruction had significantly shorter operative times ( $P < 0.001$ ) (Fig 1a).

The average length of hospital stay was 18.6 days in the RFFF group, 20.7 days in the ALTF group, 19.6 days in the FF group, 24.2 days in the PMMF group and 18.1 days in the LF group. Although the mean length of hospital stay in the LF group was shorter than 19.95 days in the free flap group, the difference was not statistically significant ( $P = 0.108$ ) (Fig 1b). Nine patients with an RFFF flap spent over 21 days in hospital (21%), compared with 13 ALTF patients (43%), 6 FF patients (46%), 6 PMMF patients (67%) and 8 LF patients (30%). Neck infection and partial flap necrosis were the two most common causes of extended hospitalisation.

### Complications

Complications including flap-related, recipient site, donor site and medical-related complications are displayed in Table 2. The most common flap-related complication was partial flap necrosis, six cases of which were identified in the LF group, followed by five in the PMMF group, four in the ALTF group and two in the RFFF group. No cases of total flap necrosis were presented in this study. Only one RFFF patient underwent operative revision due to venous thrombosis.

The most common of the recipient site complications was wound dehiscence, 54% (7/13) cases of which were presented in the ALTF group. Recipient site complications were most prevalent with ALTF reconstruction: seven patients had wound dehiscence, two had a

neck infection, one had an orocutaneous fistula, one had a hematoma and one had a chylous fistula. Eight patients in the RFFF group experienced recipient site complications, followed by seven in the PMMF group, five in the LF group and three in the FF group. Thus, the highest incidence of recipient site complications was found in the PMMF group (7/9, 78%), followed by the ALTf (12/30, 40%), FF (3/13, 23%), RFFF (8/43, 19%) and LF groups (5/27, 19%).

Owing to the skin graft in the donor site, the overall donor site complications were higher in the RFFF group than the other groups. The patients with RFFF reconstructions had two episodes of delayed wound healing and two cases of partial loss of skin grafts. In the FF group, two cases of wound dehiscence were identified, whereas there were no donor site complications in the ALTf and PMMF groups. In the LF group, the donor site was physically close to the recipient site; thus, in our study, all the donor site complications in the LF group were incorporated into the recipient-related complications. Of the medical-related complications, one case developed pneumonia in the LF group and the other case of pneumothorax was presented in the FF group.

## Discussion

In the FOM, the choice of reconstruction depends on the size and location of the defect. The main goals are to separate the oral cavity and neck and to maintain chewing, swallowing and pronunciation. Primary closure may be sufficient for small defects that would not result in a fistula between the oral cavity and neck or limit tongue movement. For large defects, various types of flaps have been used to provide soft tissue bulk between the ventral tongue and mandible and maintain mandibular continuity.

Currently, RFFF and ALTf are among the most popular types of free flap used for reconstruction of oral soft tissue defects. It has been widely accepted that RFFFs are thinner and more pliable than ALTfs, which provides the tongue with the possibility of flexible movement. Due to the many cases of wound dehiscence in the ALTf group, our results showed a higher incidence of recipient-related complications in this group (12/30, 40%) than in the RFFF group (8/43, 19%). The possible explanation for this is that an ALTf is not pliable enough for defects involving the anterior part of the tongue because of the tongue's frequently flexible movement. ALTfs were used mainly to repair larger or through-and-through defects, leading to a relatively higher incidence of postoperative complications. Thus, careful suturing decompression incision,

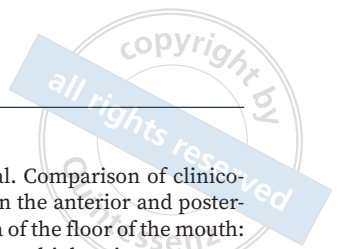
flap suture anchoring with the alveolar process and flap suture slinging to the left teeth would decrease the rate of wound dehiscence. The past decades have seen the introduction of perforator-based chimeric ALTfs. With the chimeric-designed ALTfs, the anterolateral thigh muscle is filled at the muscle defects of the FOM to prevent an orocutaneous fistula and the skin is used to repair the defect affecting the tongue and oral mucosa. Furthermore, an ALTf can be trimmed individually into fasciocutaneous, adipofascial, de-epithelialised and folded flaps to meet the demands of FOM reconstruction; however, for female and obese male patients, caution should be exercised when choosing ALTfs because the flap harvesting process is tedious and time-consuming and has many technical surgical requirements. Previous studies compared differences between an ALTf and RFFF in terms of flap survival, complications, satisfaction with appearance, swallowing capacity and intelligibility of speech when they were used for reconstruction in the oral cavity and showed that both flaps were reliable with favourable results, but ALTfs are better for large soft tissue defects and those with a lower rate of donor site morbidity<sup>6,7</sup>. In addition, other studies found that wound infections and fistulas were more common with RFFFs due to their insufficient subcutaneous tissue for packing of compound defects after ablative surgery of FOM SCC<sup>8,9</sup>, which is in line with our results. One of the advantages of an ALTf flap is that the size of the muscular bulk can be isolated as required. In our experience, the appropriate size of muscular bulk is harvested to fill the dead spaces in the submandibular region. Thus, more ALTf flaps were used for the T4 cases with a through-and-through defect than RFFF flaps in our study. Although many attempts have been made to improve reconstruction of FOM defects, the incidence of postoperative complications with free flaps was 46.5% in our patients, which was higher than other defect reconstructions for head and neck cancer<sup>10</sup>; however, very few published studies focus on the postoperative complications of FOM reconstruction. A previous study reported more flap necrosis during reconstruction of the tongue, FOM or oropharynx than in the buccal mucosa, oral and facial skin and the gingiva<sup>11</sup>, which may explain the high incidence of postoperative complications in our study. When the tumour invades the FOM and mandible deeply, reconstruction can be achieved with a free compound flap, such as fibular or scapula flaps. Since its introduction in 1989, the free fibular flap has been the mainstay of repair of various mandibular defect types<sup>12</sup>. Although a large skin paddle based on distal septocutaneous perforators<sup>13</sup> and the flexor hallucis longus and soleus

muscles<sup>14</sup> can provide the soft tissue needed for reconstruction, an approach involving a combination of two free flaps is sometimes mandatory for a massive complex defect involving the mandible, FOM and tongue<sup>15</sup>. In our study, a combination of RFFF and FF was used to repair an extensive defect after tumour resection due to the absence of perforating branches of skin in the fibular flap. In some elderly patients with a poor prognosis, mandibular defects may be restored with a titanium reconstruction plate and soft tissue defects may be reconstructed with ALTF or PMMF wrapping around the plate to avoid extrusion. In the present study, some patients underwent marginal mandibulectomy because of the inadequate soft tissue margins. In this situation, only a soft tissue flap was required to cover the rest of the mandible.

The PMMF has been used frequently for head and neck reconstruction owing to its versatile design, easy dissection and reliable blood supply; however, its use has decreased dramatically since the application of the ALT flap. In our experience, PMMFs were mainly used for patients with high risk factors for microsurgical reconstructions including preoperative radiotherapy, prior surgical therapy or a high American Society of Anesthesiologists (ASA) grade. Zou et al<sup>11</sup> reported 24 PMMFs in patients with recurrent oral SCC, with six of them being SCC in FOM. More flap necrosis occurred during reconstruction of the tongue, FOM and oropharynx than the buccal mucosa, oral and facial skin, and gingiva. In our study, the incidence of recipient site complications and flap-related complications was 77.78% (7/9) and 55.56% (5/9), respectively. A possible explanation for this is that the mandible compresses the pedicle of the PMMF due to its bulk and postoperative oedema. The hypothesis is supported by Marques et al<sup>16</sup>, who found no PMMF necrosis in patients with FOM SCC who underwent glossectomy and segmental mandibulectomy. Additionally, in our study, seven of nine patients with PMMF had undergone prior surgical and/or radiation therapy, which could impact the local blood supply or anatomy, thus increasing the rate of wound dehiscence, orocutaneous fistula and neck infection. For patients who had previously undergone treatment, the design of the PMMF flap that was larger than the defects, a more reliable blood supply and longer pedicle would reduce complications. Preservation of the lateral thoracic artery in addition to the thoracoacromial artery can improve unstable blood circulation in the PMMF<sup>17</sup>. Chen et al<sup>18</sup> reported that an extensive segmental PMMF via the anterior axillary line could effectively prolong the pedicle of conventional PMMF and enable better shoulder abduction.

Although free flaps are the gold standard for oral cavity reconstruction, local pedicled flaps may be helpful for some patients who are elderly and have complex chronic comorbidities or who cannot afford expensive health care costs. In our study, platysma myocutaneous flaps were used in 12 cases, submental island flaps in nine cases, buccinator myomucosal flaps in four cases and sternocleidomastoid myocutaneous flaps in two cases. One of the greatest advantages of cervical pedicled flaps is that they avoid the need for a separate donor site. Another advantage is that LF reconstruction is a quick procedure, as in our cases where the mean surgical time was 6 hours and 1 minute, which was significantly shorter than for the free flap reconstruction groups; however, there are several concerns regarding the use of cervical pedicled flaps in oral reconstruction. First, controversy exists regarding the potential risk of transferring occult metastasis to the recipient site. To reduce the risk, some authors have proposed a submental artery island perforator flap and sternocleidomastoid perforator flap<sup>19,20</sup>. Second, debate remains as to whether a cervical pedicled flap is appropriate after the identification of nodal metastasis. Third, neck dissection and prior radiotherapy may affect the blood supply of cervical pedicled flaps. Finally, a cervical pedicled flap can only provide enough volume of tissue for small-to-medium defects. In the LF group in our study, 26 of 27 cases were at early tumour stage. No extracapsular metastases were identified in patients with LF reconstructions on preoperative imaging, which was confirmed by pathological examination; however, postoperative pathological examination detected positive lymph nodes in 14 patients. In the LF group, one patient had previously received chemotherapy and none had previously undergone neck dissection or radiotherapy. No complications were identified in the patient who had undergone chemotherapy. We propose that prior radiotherapy and extracapsular extension of the cervical nodes are contraindications for LF reconstruction.

To the best of our knowledge, this study represents one of the largest reported series of reconstructions of FOM defects following cancer surgery; however, the study inevitably has some limitations due to its retrospective nature. Long-term complications like localised numbness of donor site were not evaluated because some patients died or were lost to follow-up. Swallowing and speech functions were not compared between different types of flaps because impairment of swallowing and speech increased with defect size, and the choice of the flaps varied significantly with the defect size and clinical stage. There was a greater number of T3 and T4 tumours in the FF group than those



in the LF group. Moreover, postoperative radiation therapy or chemoradiotherapy can adversely affect speech and swallowing.

## Conclusion

Patients in the ALTF group developed a greater number of overall recipient site complications compared with those in the other groups, while the overall donor site complications were significantly higher in the RFFF group. LFs are an appropriate choice for reconstructing small-to-medium FOM defects without extracapsular cervical metastasis and prior radiotherapy. Compared with RFFF, ALTF is better for large through-and-through defects, but it is less suitable for defects involving the anterior part of the tongue. For complex defects involving the mandible, FF is an optimal choice. PMMP provides a good choice for recurrent FOM SCC or patients with high risk factors for microsurgical reconstructions, which makes it the last-line reconstruction for FOM defects.

## Conflicts of interest

The authors declare no conflicts of interest related to this study.

## Author contribution

Dr Qu DENG carried out the experiments and drafted the manuscript; Drs Qiu Sheng XU conducted the statistical analysis; Drs Xu Hui ZHANG and Jing Chan XIE reviewed the literature; Prof Yi Fang ZHAO and Yan Ping HU revised the manuscript comprehensively; Prof Jun JIA designed and supervised the study.

(Received Jun 17, 2022; accepted Jan 31, 2023)

## References

- Chatterjee A, Laskar SG, Chaukar D. Management of early oral cavity squamous cancers. *Oral Oncol* 2020;104:104627.
- Sinha N, Rigby MH, McNeil ML, et al. The histologic risk model is a useful and inexpensive tool to assess risk of recurrence and death in stage I or II squamous cell carcinoma of tongue and floor of mouth. *Mod Pathol* 2018;31:772–779.
- Mao L. Oral squamous cell carcinoma - Progresses from risk assessment to treatment. *Chin J Dent Res* 2012;15:83–88
- Almeida Parra F, Bueno De Vicente Á, Ranz Colio Á, et al. Transmandibular approach in head and neck oncological surgery. *Chin J Dent Res* 2020;23:257–264.
- Oikawa Y, Tanaka K, Ohsako T, et al. Comparison of clinicopathological characteristics between the anterior and posterior type of squamous cell carcinoma of the floor of the mouth: The anterior type is a risk factor for multiple primary cancer. *Front Oncol* 2021;11:682428.
- Chen H, Zhou N, Huang X, Song S. Comparison of morbidity after reconstruction of tongue defects with an anterolateral thigh cutaneous flap compared with a radial forearm free-flap: A meta-analysis. *Br J Oral Maxillofac Surg* 2016;54:1095–1101.
- Loreti A, Di Lella G, Vetrano S, Tedaldi M, Dell'Osso A, Poladas G. Thinned anterolateral thigh cutaneous flap and radial fasciocutaneous forearm flap for reconstruction of oral defects: Comparison of donor site morbidity. *J Oral Maxillofac Surg* 2008;66:1093–1098.
- Stark B, Nathanson A, Hedén P, Jernbeck J. Results after resection of intraoral cancer and reconstruction with the free radial forearm flap. *ORL J Otorhinolaryngol Relat Spec* 1998;60:212–217.
- Chen CH, Lin GT, Fu YC, et al. Comparison of deltopectoralis flap and free radial forearm flap in reconstruction after oral cancer ablation. *Oral Oncol* 2005;41:602–606.
- Lo SL, Yen YH, Lee PJ, Liu CC, Pu CM. Factors influencing postoperative complications in reconstructive microsurgery for head and neck cancer. *J Oral Maxillofac Surg* 2017;75:867–873.
- Zou H, Zhang WF, Han QB, Zhao YF. Salvage reconstruction of extensive recurrent oral cancer defects with the pectoralis major myocutaneous flap. *J Oral Maxillofac Surg* 2007;65:1935–1939.
- Hidalgo DA. Fibula free flap: A new method of mandible reconstruction. *Plast Reconstr Surg* 1989;84:71–79.
- Ozalp T, Masquelet AC, Begue TC. Septocutaneous perforators of the peroneal artery relative to the fibula: Anatomical basis of the use of pedicled fasciocutaneous flap. *Surg Radiol Anat* 2006;28:54–58.
- Kuo YR, Shih HS, Chen CC, et al. Free fibula osteocutaneous flap with soleus muscle as a chimeric flap for reconstructing mandibular segmental defect after oral cancer ablation. *Ann Plast Surg* 2010;64:738–742.
- Gong ZJ, Zhang S, Zhang S, Liu J, Xu YM, Wu HJ. Reconstruction of through-and-through oromandibular defects with combined fibula flap and anterolateral thigh flap. *J Oral Maxillofac Surg* 2017;75:1283–1292.
- Marques A, Abrahao M, Castro M, et al. Complications of the pectoralis major osteomyocutaneous flap used for head and neck reconstruction. *Eur J Plasti Surg* 1996;19:229–233.
- Kumegawa S, Miyazaki H, Sakata Y, et al. Lateral thoracic artery can stabilize circulation in the pectoralis major myocutaneous pedicle flap: Single-center, prospective, uncontrolled case series. *Plast Reconstr Surg Glob Open* 2021;9:e3860.
- Chen WL, Zhang DM, Huang ZQ, Wang Y, Zhou B, Wang YY. Comparison of outcomes with extensive segmental pectoralis major myocutaneous flap via the anterior axillary line and the conventional technique in oral and oropharyngeal cancer. *Head Neck* 2018;40:349–354.
- Avery CM. The sternocleidomastoid perforator flap. *Br J Oral Maxillofac Surg* 2011;49:573–575.
- Mutlu ÖÖ, Yasak T, Egemen O, Kayadibi T, Tasasiz K. The use of submental artery perforator island flap without including digastric muscle in the reconstruction of lower face and intraoral defects. *J Craniofac Surg* 2016;27:e406–e409.

# Quantitative Assessment of Dimensional Evaluation and Artefacts from Filling Materials with CBCT Using Standard Phantom Roots

Xiao Bo CHEN<sup>1,2</sup>, Zhe Jun WANG<sup>2</sup>, Ya SHEN<sup>2</sup>, Andrea ESTEVES<sup>2</sup>, He LIU<sup>2,3</sup>, Gui Bin HUANG<sup>4</sup>, Xiao Yan WANG<sup>4</sup>, Lin YUE<sup>4</sup>, Markus HAAPASALO<sup>2</sup>

**Objective:** To investigate the accuracy of dimensional evaluation and representation of artefacts generated by different gutta-percha (GP) cones with or without sealer with CBCT using a reproducible, standardised phantom root methodology.

**Methods:** The reproducible artificial phantom roots with six root canal sizes from #25 to #50 and 0.04 taper were aligned according to the jaw curvature in a stone model for dimensional measurements. Each root was scanned while empty and filled with four types of filling materials. The specimens were scanned using the CS 9300 3D (Carestream Dental, Rochester, NY, USA) (at two different resolutions), 3D Accuitomo (J Morita, Kyoto, Japan) and NewTom VG1 (Verona, Italy) CBCT systems. The hyperdense and hypodense axial slice artefacts from root canal sizes #40, #45 and #50 were recorded.

**Results:** Dimensions were significantly smaller and more accurate with CS 9300/0.09 mm voxel size than with other protocols. The hypodense band was found mostly in the CS 9300 3D system with 0.18 mm voxel size, especially in the buccal-lingual (95%) and coronal (64%) sections. The 3D Accuitomo CBCT system showed the lowest presence of the hypodense band. Areas of both light and dark artefacts were significantly larger in the coronal third than in the apical and middle thirds.

**Conclusion:** Artefacts in the coronal locations and in buccal-lingual sections were more evident in the CS 9300 3D system with a 0.18-mm voxel size.

**Key words:** artefact, CBCT, gutta-percha, measurement, zirconium  
*Chin J Dent Res* 2023;26(2):83–92; doi: 10.3290/j.cjdr.b4128007

1 Department of Stomatology, Hospital of Tsinghua University, Beijing, P.R. China.

2 Division of Endodontics, Department of Oral Biological & Medical Sciences, Faculty of Dentistry, University of British Columbia, Vancouver, BC, Canada.

3 Department of Stomatology, Affiliated Hospital of Jining Medical University, Jining, Shandong Province, P.R. China.

4 Department of Cariology and Endodontology, Peking University School and Hospital of Stomatology, Beijing, P.R. China.

**Corresponding authors:** Prof Markus HAAPASALO, Chair, Division of Endodontics, UBC Faculty of Dentistry, 2199 Wesbrook Mall, Vancouver, BC, Canada V6T 1Z3. Tel: 1-604-822-5996; Fax: 1-604-822-3562. Email: markush@dentistry.ubc.ca

Prof Lin YUE, Department of Cariology and Endodontology, Peking University School and Hospital of Stomatology, #22 Zhongguancun South Avenue, Haidian District, Beijing 100081, P.R. China. Tel: 86-10-82195526; Fax: 86-10-62173402. Email: kqlinyue@bjmu.edu.cn

This study was supported by the National Natural Science Foundation of China (U20A20169).

CBCT has been accepted as an essential tool for diagnosis and treatment planning in dentistry, as it permits the construction of 3D images of the targeted teeth and areas<sup>1</sup>. Despite the advances in endodontics produced by CBCT, artefacts have been reported with this tool that can degrade the image quality and mask abnormalities in the presence of high-density obturation materials in the root canals. Worse still, these artefacts cannot be easily avoided<sup>2-4</sup>. Among the possible causes of artefacts, beam hardening is described as the most common. One of the leading causes is the presence of high-density materials within the field of view (FOV); those encountered by endodontists are metal implants, intracanal posts, metallic crowns and amalgam restoration, especially root-filling materials<sup>5</sup>. A reconstructed 3D volume like CBCT represents a reasonable estimation of density within the object at that particular location represented in the particular voxel. Artefacts in the vicinity of highly

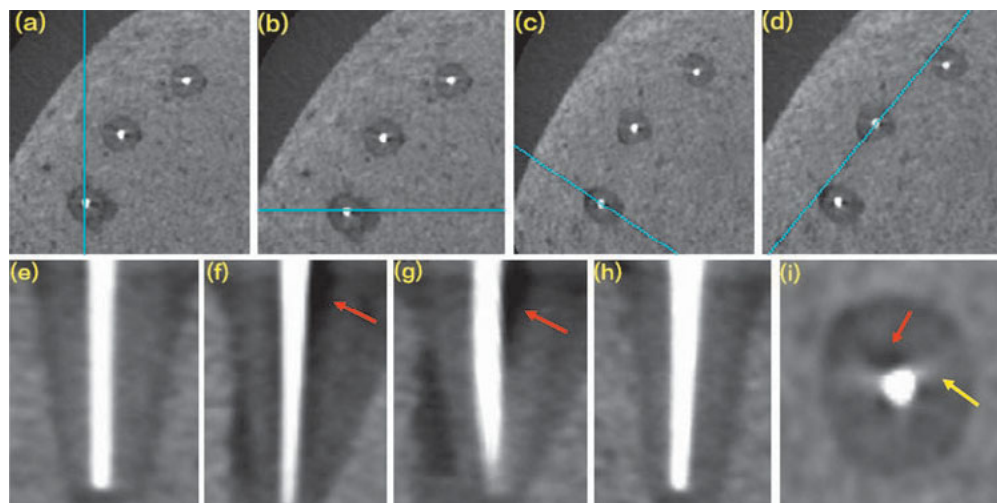


**Fig 1** Artifacts in axial and longitudinal sections of EndoSequence GP, #50 in CS 0.18 mm protocol. (a-d) Section line for sagittal, coronal, buccal-lingual, and mesiodistal sections in axial views. (e-h) Images in sagittal, coronal and buccal-lingual views. (i) Axial view. Red arrow, hypodense area; yellow arrow, hyperdense streaks.

dense materials are either caused by beam hardening or by the complete extinction of the beam. Since these materials have extremely high atomic numbers and are highly dense. In this case, zero energy is recorded on the detector “behind” such material.

Artefacts resulting from root-filling material along the long axis of the alveolar bones may result in difficulties with diagnosis<sup>6</sup>. Some previous studies used extracted teeth as the study models to assess the artefacts produced by vertical root fracture<sup>7,8</sup>. Others showed that artefacts might obscure or resemble pathology, and therefore impede accurate diagnosis and subsequent treatment planning<sup>9-14</sup>.

Phantom teeth<sup>15</sup> and phantom blocks with pins<sup>5,16</sup> were used in previous studies for artefact assessment. The development of a phantom tooth model with standardised and reproducible root canal morphology can offer a platform to evaluate the accuracy (e.g., area, maximum and minimum diameters) of different obturation materials in the root canal system. So far, few studies have been able to quantify high-density artefacts in CBCT images, especially in standardised phantom roots.

Zinc oxide and barium sulphate in gutta-percha (GP) contribute to the radiopacity of the material. Zirconium is a weak attenuator used in endodontic bioceramic sealers, which may influence the artefacts and the grey values in CBCT images<sup>15</sup>. The grey value has been recognised as the index to assess the density or quality of the material<sup>17</sup>. Despite the good physical, chemical and biological properties of the bioceramic sealer materials<sup>18</sup>, properly depicting obturation material in 3D images is challenging. So far, little is known about the impact of obturation materials and bioceramic sealers on CBCT artefacts and accuracy.

The present study aims to develop a reproducible novel artificial phantom root to investigate the artefacts and accuracy of the dimensional evaluation of different root canal filling materials using four CBCT protocols.

## Materials and methods

### Phantom setup

A reproducible phantom, including a stone model<sup>19</sup> with a standardised straight phantom single root and root canal, was fabricated to measure accuracy and artefacts. To determine the accuracy of dimensional evaluation, the dental stone phantom was fabricated by mixing equal volumes of type III stone plaster (Whip Mix, Louisville, KY, USA) and sawdust, with the shape like the alveolar process of the maxilla. Six sockets were created by arranging MicroAmp tubes (Thermo Fisher Scientific, Waltham, MA, USA), coated with a thin layer of Vaseline, according to the jaw curvature in the phantom model with 6 mm distance between the cervical plane of each root. Equal volumes of epoxy resin (ArtResin, Carrollton, TX, USA) and calcium carbonate (C5929-100G, MilliporeSigma, Burlington, MA, USA) were mixed thoroughly in the tubes, then the filled tubes were vibrated in a VWR Mini Vortexer (Henry Troemner, Thorofare, NJ, USA) for 90 seconds each to eliminate any visible bubbles. Before the resin was set, a 0.04-taper vaseline-coated paper point (Brasseler, Savannah, GA, USA) for one of six different sizes (#25, #30, #35, #40, #45 and #50), was inserted gently in the centre of each resin-filled tube. The top of each tube was covered with a



thin layer of wax to centre the paper points precisely. The paper points were pulled out after the resin was cured, leaving a standard size canal space. Five groups of artificial root fillings, each in six sizes (taper 0.04, size #25 to #50), were prepared: group 1, with no filling; group 2 (GPE), filled with EndoSequence BC GP cones (Brasseler); group 3 (GPV), filled with Vortex GP cones (Dentsply Sirona Endodontics, Tulsa, OK, USA); group 4 (GPEB), filled with EndoSequence BC GP with iRoot SP, root canal sealer (Innovative BioCeramix, Burnaby, BC, Canada); and group 5 (GPVA), filled with Vortex GP with AH Plus sealer (Dentsply DeTrey, Konstanz, Germany). For groups 4 and 5, CBCT scanning was performed after allowing the sealer to set for 72 hours in a water bath at 37°C.

For the artefact measurements, using the same phantom model, the artificial root canals of three sizes (#40, #45, and #50, taper 0.04) were aligned according to the jaw curvature in sequence (#50 in the posterior region of the dental arch, #45 in the premolar region and #40 in the anterior region) as shown in Fig 1. The artificial root and the real root showed similar radiographic contrast and grey value, as shown by a similar threshold of grey values in Fig 2. Each sample was scanned as unrestored and then restored with four types of root filling materials: EndoSequence BC GP cones only; Vortex GP cones only; EndoSequence BC GP with iRoot SP, injectable root canal sealer; and Vortex GP with AH Plus sealer. The artificial roots for accuracy of dimensional evaluation and artefact measurements were coated with a thin layer of wax (white utility wax strips; Coltene Whaledent, Alstätten, Switzerland) and then placed in the corresponding sockets in the phantom stone model, aligned to the same position for the CBCT scan (Fig 3).

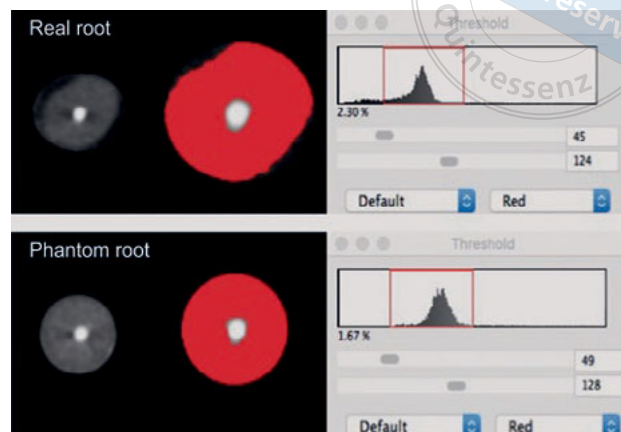


**Fig 2** CBCT images of the real root and phantom root scanned by CS 9300 under a voxel size of 0.09 mm. The histograms show nearly identical grey values for both objects.

### CBCT image acquisition and processing

The phantom model was positioned on a reproducible platform kept in the same location. The phantom jaw was placed in a round plastic box full of water on the CBCT jig, which was equivalent to a soft tissue surrounding the skull<sup>19</sup>. Images were taken using the following endodontic scanning protocols:

1. CS 9300 3D system (Carestream Dental) with two exposure protocols: 84 kV 5 mA and 90 kV 5 mA. Voxel size and FOV were fixed at 0.09 mm, 5 cm × 5 cm and 0.18 mm, 8 cm × 8 cm (CS0.09, CS0.18);
2. 3D Accuitomo (J. Morita, Kyoto, Japan) with 80 kV 3 mA 0.125 mm, 6 cm × 6 cm (Morita);
3. NewTom VGi (QR SRL, Verona, Italy) with 110 kV 5.2 mA 0.10 mm, 5 cm × 5 cm.



**Fig 3** Scanning condition of the phantom. (a) CS 9300; (b) 3D Accuitomo; (c) Newtom VGi).



**Table 1** Exposure protocols for each CBCT device.

| Parameter                      | CS9300 | CS9300 | 3D Accuitomo | Newton VGi |
|--------------------------------|--------|--------|--------------|------------|
| Tube voltage (kV)              | 90     | 84     | 80           | 110        |
| Tube current (mA)              | 5      | 5      | 3            | 5.2        |
| Field of view (FOV, mm)        | 8 × 8  | 5 × 5  | 6 × 6        | 5 × 5      |
| Voxel size (mm)                | 0.18   | 0.09   | 0.125        | 0.10       |
| Slice thickness (mm)           | 0.20   | 0.09   | 0.125        | 0.10       |
| Exposure time (s)              | 19     | 28     | 30.8         | 36         |
| Resolution (1/2*pixels per mm) | 2.78   | 5.56   | 4            | 5          |

Exposure parameters were optimised for the phantom roots. The exposure protocols for each device are listed in Table 1. For the qualitative analysis of the CBCT image, all data were exported as DICOM files and imported into Image J software (version 1.52a, National Institutes of Health, Bethesda, MD, USA) for measurement.

*Imaging processing*

**Dimensional evaluation**

A total of 120 volumes were acquired (five groups of six sizes of four exposure protocols). Axial images of roots were selected from three regions: apical (2 mm above the apical end of the root filling/canal), middle (5 mm above the apical end of the root filling/canal) and coronal (8 mm above the apical end of the root filling/canal). Each root adjusted the position according to the axis line from the apex to the central point of the crown plane to make sure the cross-section was perpendicular to the long axis of the root while measuring. For each region, five images at the slice thickness intervals were selected (segment slice and two adjacent slices in both apical and coronal directions). The diameters of phantom root fillings at the three measurement locations (2 mm, 5 mm, 8 mm above the apical end of the root filling) were measured using a digital Vernier caliper before being placed in each phantom root canal, which was used as a “ground truth”. A total of 450 images were selected for each exposure protocol (15 slices with five groups, six sizes), with no filling group as the baseline for control. The resulting images were set to 8-bit colour depth, saved with a black background in TIFF format and imported into ImageJ software.

All the axial images with fillings were measured with ImageJ, using a wand (tracing tool) to segment the target automatically with the same fixed tolerance and threshold regions. Area and the maximum and minimum diameter of axial canal images were all calculated by the ImageJ software algorithm. The threshold tool and fixed region of interest (ROI) tool were both used to represent the area.

**Artefact measurement**

The artefact pixel intensity value ranges were established for the hyperdense zone (light) and hypodense (dark) artefacts for each protocol, respectively. Threshold tools and fixed ROI tools were used manually, along with standardised segmentation of the area for light and dark artefacts for each axial section. Within the ROIs, areas of light and dark artefacts were measured according to the grey value threshold using the software. Both light and dark artefacts were seldom observed in the apical part of sizes #25, #30 and #35. Thus, axial slice artefacts from root canal sizes #40, #45 and #50 were recorded. A total of 225 axial images in TIFF format were selected for each exposure protocol (15 slices with five groups, three sizes). Longitudinal images were acquired from four directions (Figs 1a to d), all passing through the centre of the tooth. As such, a set of four longitudinal images for each group were obtained as follows: one in sagittal view and one in coronal views (Figs 1e and f), one in buccal-lingual (B-L) view, and one in mesio-distal (M-D) view (Figs 1g and h). The hypodense band in a total of 60 longitudinal images in TIFF format was selected for each exposure protocol (slices of four directions with five groups, three sizes). The score for the hypodense band was recorded in all acquired longitudinal images with scores given according to the absence (0) or presence (1) of the dark band. Continuous and linear change of grey value was analysed in longitudinal sections using plot profile tools and surface profile tools in ImageJ. A total of 900 (225\*4) axial images and 240 (60\*4) longitudinal images were analysed twice over a 2-week period under the same display condition.

All CBCT scanning, evaluation and measurement were performed by the same three experienced radiologists and endodontists trained in CBCT diagnostic applications.

*Statistical analysis*

SPSS (version 25; IBM, Armonk, NY, USA) was used for statistical tests. The level of statistical significance was set at  $P < 0.05$ . The data were analysed statistically using a

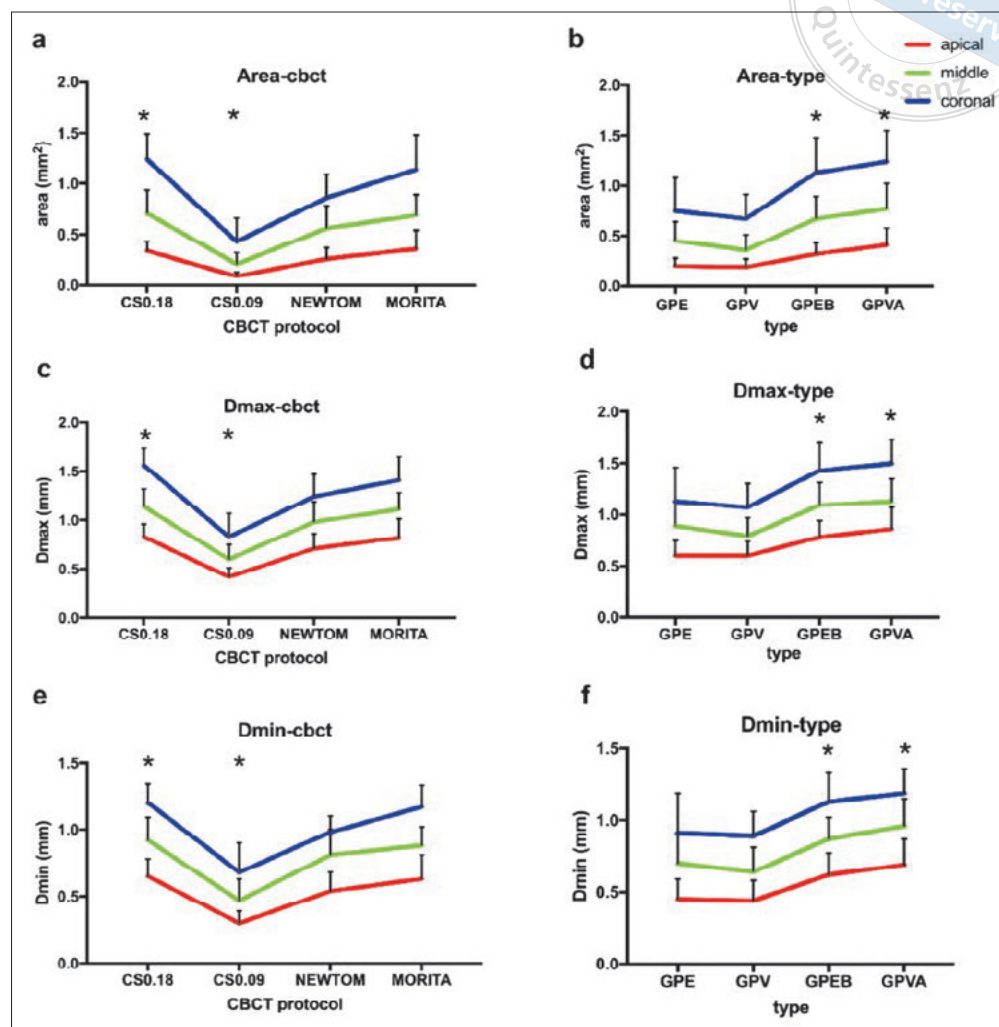


**Fig 4** Comparison of areas (**a and b**), maximum diameters (**c and d**) and minimum diameters (**e and f**) among CBCT protocols and filling types in size #30. \*Statistically significant difference compared with the other groups of the same line,  $P < 0.05$ .

one-way analysis of variance followed by a Tukey test and multiple linear regression. A Kappa test was used to assess interobserver and intraobserver agreement for the three observers. A chi-squared test was applied to compare the average presence of artefacts evaluated by the three observers (two experienced endodontists and one experienced oral radiologist) for different slice orientations.

## Results

The interobserver and intraobserver agreement ranged from 0.706 to 0.838 (substantial) for reading of the longitudinal sections.

### Dimensional evaluation

Both the areas and diameters of root fillings with CS 9300/0.09 mm voxel size were significantly smaller than

for the other three CBCT protocols as shown in Fig 4 ( $P < 0.001$ ) in all root filling sizes. The maximum/minimum diameters of root filling of #30 canal fillings in CS 9300, for example, were  $0.42 + 0.09$  mm/ $0.30 + 0.08$  mm (2 mm above the apical end of the root filling);  $0.60 + 0.15$  mm/ $0.47 + 0.15$  mm in the middle part (5 mm above the apical end of the root filling); and  $0.83 + 0.22$  mm/ $0.68 + 0.20$  mm in the coronal part (8 mm above the apical end of the root filling), depending on the CBCT protocol (Table 2). CS 9300/0.18 mm voxel size produced the largest filling area and diameters, especially when compared to CS 9300 using a voxel size of 0.09 mm ( $P < 0.05$ ).

Taking root canal filling size #30 as an example, images of groups of EndoSequence BC GP with BC iRoot SP sealer (GPEB) and Vortex GP with AH Plus sealer (GPVA) both showed significantly larger areas (Fig 4;  $P < 0.001$ ), and bigger maximum (Fig 4;  $P < 0.001$ ) and minimum diameters (Fig 4;  $P < 0.001$ ) than those of the



**Table 2** Maximum and minimum diameters of root filling.

| w        | Location | #25<br>Dmax/Dmin<br>(mm)    | #30<br>Dmax/Dmin<br>(mm)    | #35<br>Dmax/Dmin<br>(mm)    | #40<br>Dmax/Dmin<br>(mm)    | #45<br>Dmax/Dmin<br>(mm)    | #50<br>Dmax/Dmin<br>(mm)    |
|----------|----------|-----------------------------|-----------------------------|-----------------------------|-----------------------------|-----------------------------|-----------------------------|
| CS 0.18  | Apical   | 0.79 + 0.11/<br>0.56 + 0.11 | 0.83 + 0.13/<br>0.65 + 0.13 | 0.97 + 0.16/<br>0.71 + 0.15 | 1.06 + 0.18/<br>0.79 + 0.15 | 1.18 + 0.15/<br>0.85 + 0.11 | 1.24 + 0.13/<br>0.87 + 0.10 |
|          | Middle   | 1.07 + 0.12/<br>0.79 + 0.11 | 1.14 + 0.18/<br>0.92 + 0.17 | 1.23 + 0.19/<br>1.01 + 0.10 | 1.31 + 0.10/<br>1.10 + 0.14 | 1.41 + 0.12/<br>1.13 + 0.13 | 1.54 + 0.15/<br>1.19 + 0.14 |
|          | Coronal  | 1.40 + 0.16/<br>1.09 + 0.15 | 1.56 + 0.16/<br>1.20 + 0.14 | 1.59 + 0.16/<br>1.25 + 0.14 | 1.63 + 0.18/<br>1.32 + 0.12 | 1.71 + 0.19/<br>1.32 + 0.18 | 1.77 + 0.19/<br>1.36 + 0.19 |
| *CS 0.09 | Apical   | 0.38 + 0.10/<br>0.27 + 0.09 | 0.42 + 0.09/<br>0.30 + 0.08 | 0.45 + 0.12/<br>0.33 + 0.10 | 0.56 + 0.12/<br>0.45 + 0.11 | 0.65 + 0.11/<br>0.56 + 0.14 | 0.79 + 0.13/<br>0.67 + 0.12 |
|          | Middle   | 0.57 + 0.17/<br>0.42 + 0.12 | 0.60 + 0.15/<br>0.47 + 0.15 | 0.63 + 0.15/<br>0.53 + 0.13 | 0.79 + 0.11/<br>0.65 + 0.10 | 0.85 + 0.10/<br>0.72 + 0.11 | 0.90 + 0.11/<br>0.76 + 0.12 |
|          | Coronal  | 0.78 + 0.17/<br>0.60 + 0.16 | 0.83 + 0.22/<br>0.68 + 0.20 | 0.89 + 0.21/<br>0.71 + 0.81 | 1.03 + 0.13/<br>0.87 + 0.10 | 1.11 + 0.16/<br>0.96 + 0.11 | 1.15 + 0.17/<br>0.99 + 0.15 |
| NewTom   | Apical   | 0.71 + 0.14/<br>0.54 + 0.17 | 0.76 + 0.15/<br>0.57 + 0.14 | 0.81 + 0.18/<br>0.62 + 0.16 | 0.91 + 0.25/<br>0.72 + 0.20 | 0.95 + 0.26/<br>0.80 + 0.20 | 1.05 + 0.22/<br>0.79 + 0.13 |
|          | Middle   | 1.02 + 0.21/<br>0.75 + 0.12 | 0.98 + 0.21/<br>0.81 + 0.14 | 1.02 + 0.12/<br>0.86 + 0.17 | 1.14 + 0.22/<br>0.90 + 0.19 | 1.17 + 0.21/<br>0.99 + 0.12 | 1.25 + 0.24/<br>1.02 + 0.15 |
|          | Coronal  | 1.26 + 0.24/<br>0.97 + 0.15 | 1.24 + 0.23/<br>0.98 + 0.12 | 1.39 + 0.27/<br>1.06 + 0.21 | 1.40 + 0.30/<br>1.12 + 0.21 | 1.49 + 0.18/<br>1.18 + 0.22 | 1.52 + 0.17/<br>1.22 + 0.12 |
| Morita   | Apical   | 0.82 + 0.13/<br>0.63 + 0.16 | 0.86 + 0.19/<br>0.65 + 0.18 | 0.86 + 0.19/<br>0.67 + 0.23 | 0.86 + 0.19/<br>0.67 + 0.18 | 0.86 + 0.19/<br>0.71 + 0.14 | 0.86 + 0.19/<br>0.75 + 0.13 |
|          | Middle   | 1.07 + 0.20/<br>0.79 + 0.18 | 1.11 + 0.17/<br>0.88 + 0.14 | 1.11 + 0.17/<br>0.89 + 0.16 | 1.11 + 0.17/<br>0.87 + 0.17 | 1.11 + 0.17/<br>0.94 + 0.15 | 1.11 + 0.17/<br>0.97 + 0.16 |
|          | Coronal  | 1.35 + 0.19/<br>1.08 + 0.15 | 1.41 + 0.24/<br>1.17 + 0.16 | 1.41 + 0.24/<br>1.15 + 0.21 | 1.41 + 0.24/<br>1.14 + 0.15 | 1.41 + 0.24/<br>1.19 + 0.17 | 1.41 + 0.24/<br>1.21 + 0.13 |

\*Statistically significant difference compared with the other groups in the same location,  $P < 0.05$ .

**Table 3** Presence of hypodense halo in longitude sections.

| CBCT protocol | Sagittal | Coronal            | Buccal-lingual     | Mesiodistal         |
|---------------|----------|--------------------|--------------------|---------------------|
| CS 0.18       | 0.25     | 0.64 <sup>ab</sup> | 0.95 <sup>ab</sup> | 0.31 <sup>abc</sup> |
| CS 0.09       | 0.19     | 0.50 <sup>c</sup>  | 0.61               | 0.06 <sup>a</sup>   |
| NewTom        | 0.08     | 0.08 <sup>a</sup>  | 0.36 <sup>a</sup>  | 0.00 <sup>b</sup>   |
| Morita        | 0.00     | 0.00 <sup>bc</sup> | 0.36 <sup>b</sup>  | 0.00 <sup>c</sup>   |

<sup>a,b,c</sup>Different superscript letters in each line indicate a significant difference ( $P < 0.05$ ).

GPE and GPV groups in the apical, middle and coronal parts of the roots. The smallest area and maximum diameter were found in the GPV group ( $P < 0.001$ ). When comparing the GPV group to the GPE group, there was no significant difference in the minimum diameter. The GPVA group showed the largest areas in all filling groups ( $P < 0.001$ ).

*Artefact measurement*

Artefacts appeared like streaks and hypodense areas (Fig 1). In a total of 192 CBCT images, hypodense areas were found mostly in the CS 9300 3D system with a voxel size of 0.18 mm in all four longitudinal sections: 64% in

coronal, 25% in sagittal, 95% in buccal-lingual and 31% in mesiodistal sections (Table 3), followed by the CS 9300 system with a voxel size of 0.09 mm. The 3D Accutomo CBCT system showed a low presence of artefacts, and only in buccal-lingual sections of size #40 (anterior zone). Hypodense artefacts were observed significantly more often in coronal and buccal-lingual sections, but less in sagittal and mesiodistal sections in all four protocols.

The roots filled with Vortex GP (GPV group) exhibited the smallest light areas (hyperdense artefacts) in all four CBCT protocols and in all three locations ( $P < 0.001$ ). EndoSequence GP with BC sealer (GPEB group) and Vortex GP with AH Plus sealer (GPVA group) showed the largest light areas. With the CS 9300 3D

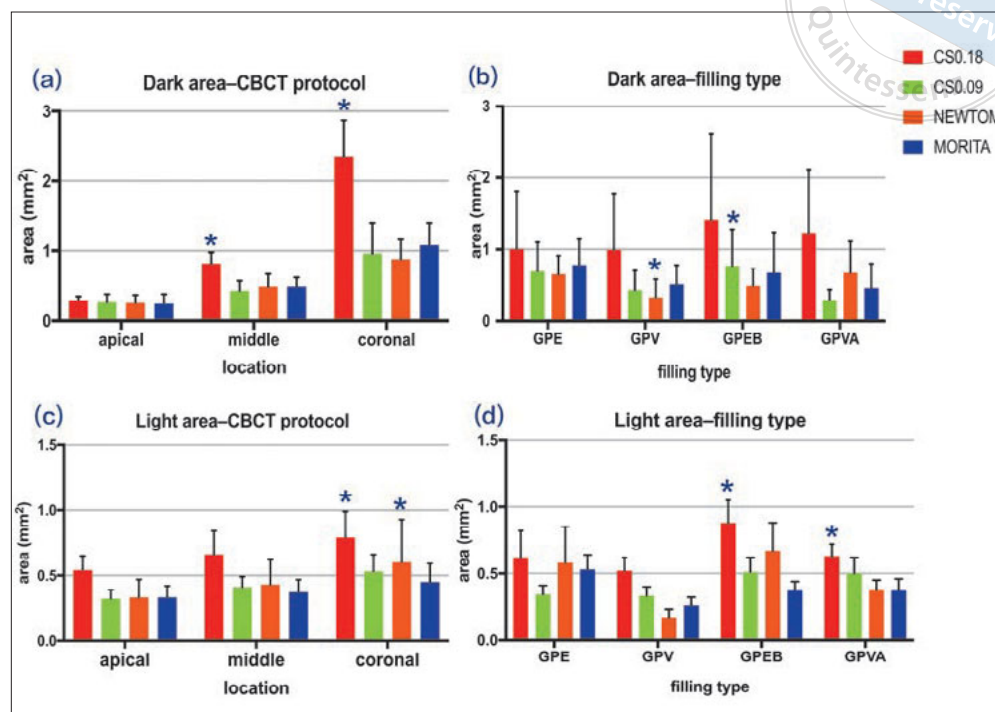


**Fig 5** Comparison of areas ( $\text{mm}^2$ ) of light and dark artefacts among different CBCT (a and c) and root filling protocols (b and d) in the #50 group. \*Statistically significant difference compared with the other groups of the same colour bar,  $P < 0.05$ .

system with a voxel size of 0.18 mm, the light areas in the GPEB group were significantly larger than for the GPVA group ( $P = 0.009$ ). Measurements of the dark areas (hypodense artefacts) were performed only in the size #50 group. The GPV group showed the smallest dark areas with NewTom protocols, and the GPEB group had the largest dark areas with the CS 0.09 protocol. When using CS 9300/0.18mm and Morita protocols, dark areas of the four root-filling groups showed no significant differences. With the CS 9300 3D system with a voxel size of 0.18 mm, light and dark area artefacts were both significantly larger than for the other three CBCT protocols in apical, middle and coronal locations ( $P < 0.001$ ). Both light and dark areas were significantly larger in the coronal part than in the apical and middle part ( $P < 0.001$ ) in all four CBCT protocols and all four types of filling materials. Figure 5 shows the performance of the size #50 group. The dark areas of the middle location were significantly larger than those of the apical location for the CS 0.18 mm, NewTom, and Morita CBCT protocols ( $P < 0.001$ ,  $P < 0.001$ ,  $P = 0.003$ , respectively).

In the longitudinal sections exhibiting hypodense haloes, the plot profile analysis demonstrated an obvious decline in grey value adjacent to the GP in the coronal section, approaching zero in the nearest portion, when compared to the control group with no filling material (Fig 6); however, in the sagittal section, a slight

increase in grey value was detected for the GP close to the root wall.

## Discussion

This study used an artificial phantom root to quantitatively evaluate the dimensional evaluation and metal (high-density) artefacts generated by different filling materials. The advantage of artificial roots created in this study is that they are reproducible and with the same size (length and width) similar to real teeth. The model is easy to build and enables reliable comparison of parameters from CBCT images taken using different protocols. Furthermore, the material selected for the artificial roots has a similar radiopacity to real roots (Fig 2).

Besides the widely used AH Plus sealer and traditional GP cones, where barium and zinc are the main contributors to radiopacity, the newly introduced bioceramic sealer and GP were also investigated. New root canal obturation materials (e.g., Endosequence GP cones and sealer) with lower radiopacity profiles<sup>20</sup> and improved CBCT software algorithms are expected to minimise imaging artefacts. EndoSequence BC Sealer was investigated<sup>14</sup> and no significant difference was detected in fracture diagnostics between the zirconium-based filling material and traditional ones. In the present study, although the areas of artefacts in

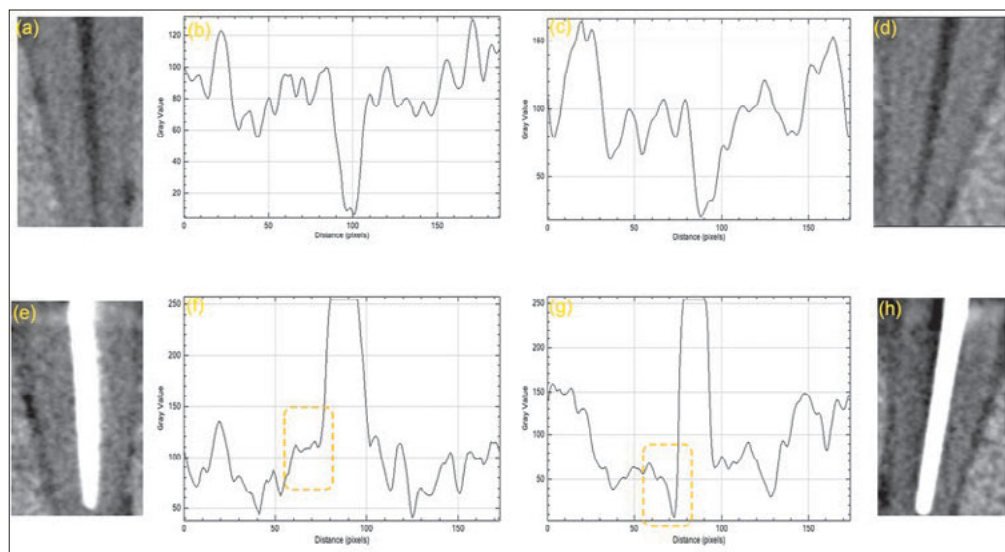


**Fig 6** Views and plot profile analysis of size #50 with no filling (a-d) and filled with EndoSequence GP (e-h) in the CS 0.09 mm protocol in sagittal (a, b, e, f) and coronal (c, d, g, h) views, demonstrating an evident decline in grey value adjacent to the GP in the coronal section, but no reduction in the sagittal section.

roots filled with zirconium-based fillings appeared to be smaller than those in roots filled with GP Vortex and AH Plus sealer, no significant difference was detected.

The thresholding method<sup>15,21</sup> was applied and a fixed ROI was used in the present study. The present study developed a reproducible methodology for characterising artefacts generated from GP with or without sealers and to quantitatively assess artefacts based on phantom roots.

It has been reported that identical tissues may appear to present different greyscale intensity values depending upon their position relative to other tissues in the irradiated field<sup>17</sup>. To minimise this, each root was kept in the same position in the same model during each scan. A previous study claimed that if the grey value is too high, artefacts may occur and compromise measurement accuracy, especially in the border area of the images<sup>17</sup>. In fact, it is not the grey value that causes these effects; it is the density and atomic number of the real object that causes beam hardening or even beam extinction. It is important to remember that radiography always measures absorption, which translates into the physical parameter “density”. In other words, reconstructed CBCT images represent a reasonable estimation of density within the object at that location represented in the particular voxel. Artefacts in the vicinity of highly dense (extremely high atomic numbers) materials are mostly caused by beam hardening. In this context, this might also explain why more artefacts were observed in the buccolingual dimension and in parts of thicker root-filling material, as shown in Table 3. Following the explanation above, this is simply due to more (non-linear) absorption in these regions/

directions and thus more incorrect redistribution of the recorded values, i.e., more prominent artefacts.

The CBCT protocol was shown to be the most reliable predictor of both hyperdense and hypodense artefacts by multiple regression. The hypodense (dark) area was most obvious in the CS9300 3D system, especially with a voxel size of 0.18 mm. In B-L sections, it even reached an incidence of 0.95 in the dark band, while dark areas larger than 2 mm<sup>2</sup> were seen in the coronal location. Artificial lines in the oblique directions resulting from root-filling material may resemble root fractures. These hypodense artefacts were not observed with Accutomo previously<sup>2,22</sup>, which is consistent with the findings of the present study. The 3D Accutomo CBCT system only showed a 36% incidence of artefacts in B-L sections (#40 size: anterior region), whereas the incidence for the other three sections was all zero.

Both light and dark areas were largest in the coronal parts of the canals, especially for the dark area in the coronal location with CS 0.18, which is consistent with previous studies<sup>2,15</sup>. The greater light artefact area in the coronal third was associated with the larger volume of root fillings in this third. For the middle and apical thirds of the canal, fewer light artefacts were observed because of the smaller volume of root fillings. This may explain the difficulty in reading and segmentation in sizes #40 and #45 of the root canal fillings for the dark artefacts. This finding is also in line with the notion of strengthening minimal instrumentation in modern endodontics to save dentine by reducing instrumentation sizes<sup>23</sup>, leading to lighter artefacts.

Artefacts may have a significant impact on diagnosis, planning and follow-up<sup>24</sup>. An image-reading approach<sup>25</sup>

suggests that a map-reading strategy of viewing sequential axial slices resolved the problem<sup>26</sup>. Longitudinal images were obtained and analysed according to this protocol in the present study. The surface plot of grey value in Fig 6 demonstrated an evident decline adjacent to GP in this apparently hypodense band. B-L and coronal sections showed the highest incidence of the hypodense band even with the 3D Accuitomo, indicating that careful interpretation is essential to avoid an incorrect diagnosis of fracture lines or under-obturation<sup>2</sup>. In the back-projection process, which is no more than a highly simplified inversion of the true physical projection process, the recorded energy is “smeared back” from the detector pixels along the ray paths towards the source, and in such cases incorrect (relatively too high) energies are distributed in the reconstruction volume. This causes dark (hyperdense) bands that are always along the back-projection lines. Extinction would cause hyperdense (light) stripes along those lines; however, a posteriori “correction” of the reconstructed volume as implemented by manufacturers may often alter the colour of the stripes. This makes it difficult to correct, as the information on the true density cannot be derived from the projections as they are the only source used for CBCT scans. Thus, the present study described the performance of artefacts induced by root canal fillings rather than revealing the internal cause of artefacts. Such information could be derived from evaluating thousands of existing computed tomography or CBCT scans and using this information in learning systems, such as artificial intelligence.

## Conclusion

CBCT showed acceptable accuracy of measurement of filling material dimensions. More artefacts were detected in the CS 9300 3D system with a voxel size of 0.18 mm in the coronal location and in the B-L section.

## Conflicts of interest

The authors declare no conflicts of interest related to this study.

## Author contribution

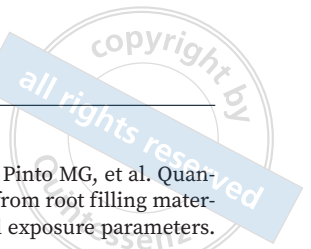
Dr Xiao Bo CHEN contributed to the conceptualisation of the study and drafted the manuscript; Drs Zhe Jun WANG, Ya SHEN, Andrea ESTEVES and He LIU contributed to the analysis and interpretation of data; Gui Bin HUANG contributed to drafting the manuscript and finalising the article; Dr Xiao Yan WANG contributed

to drafting the manuscript; Drs Lin YUE and Markus HAAPASALO contributed to the conception and design of the study and the supervision of the project.

(Received Sep 21, 2022; accepted Jan 31, 2023)

## References

- Liang YH, Jiang L, Gao XJ, Shemesh H, Wesselink PR, Wu MK. Detection and measurement of artificial periapical lesions by cone-beam computed tomography. *Int Endod J* 2014;47: 332–338.
- Vasconcelos KF, Nicolielo LF, Nascimento MC, et al. Artefact expression associated with several cone-beam computed tomographic machines when imaging root filled teeth. *Int Endod J* 2015;48:994–1000.
- Panjnoush M, Kheirandish Y, Kashani PM, Fakhar HB, Younesi F, Mallahi M. Effect of exposure parameters on metal artefacts in cone beam computed tomography. *J Dent (Tehran)* 2016;13:143–150.
- Pinto MGO, Rabelo KA, Sousa Melo SL, et al. Influence of exposure parameters on the detection of simulated root fractures in the presence of various intracanal materials. *Int Endod J* 2017;50:586–594.
- Codari M, de Faria Vasconcelos K, Ferreira Pinheiro Nicolielo L, Haiter Neto F, Jacobs R. Quantitative evaluation of metal artefacts using different CBCT devices, high-density materials and field of views. *Clin Oral Implants Res* 2017; 28:1509–1514.
- Iikubo M, Nishioka T, Okura S, et al. Influence of voxel size and scan field of view on fracture-like artefacts from gutta-percha obturated endodontically treated teeth on cone-beam computed tomography images. *Oral Surg Oral Med Oral Pathol Oral Radiol* 2016;122:631–637.
- da Silveira PF, Vizzotto MB, Liedke GS, da Silveira HLD, Montagner F, da Silveira HED. Detection of vertical root fractures by conventional radiographic examination and cone beam computed tomography: An in vitro analysis. *Dent Traumatol* 2013; 29:41–46.
- Brady E, Mannocci F, Brown J, Wilson R, Patel S. A comparison of cone beam computed tomography and periapical radiography for the detection of vertical root fractures in nonendodontically treated teeth. *Int Endod J* 2014;47:735–746.
- Patel S, Brady E, Wilson R, Brown J, Mannocci F. The detection of vertical root fractures in root filled teeth with periapical radiographs and CBCT scans. *Int Endod J* 2013;46:1140–1152.
- Moudi E, Haghanifar S, Madani Z, Alhavaz A, Bijani A, Bagheri M. Assessment of vertical root fracture using cone-beam computed tomography. *Imaging Sci Dent* 2014;44:37–41.
- Jones D, Mannocci F, Andiappan M, Brown J, Patel S. The effect of alteration of the exposure parameters of a cone-beam computed tomographic scan on the diagnosis of simulated horizontal root fractures. *J Endod* 2015;41:520–525.
- Katkar R, Steffy DD, Noujeim M, Deahl ST 2nd, Geha H. The effect of milliamperage, number of basis images, and export slice thickness on contrast-to-noise ratio and detection of mandibular canal on cone beam computed tomography scans: An in vitro study. *Oral Surg Oral Med Oral Pathol Oral Radiol* 2016;122:646–653.
- Menezes RF, Araújo NC, Santa Rosa JMC, et al. Detection of vertical root fractures in endodontically treated teeth in the absence and in the presence of metal post by cone-beam computed tomography. *BMC Oral Health* 2016;16:48.



14. Fox A, Basrani B, Lam EWN. The performance of a zirconium-based root filling material with artifact reduction properties in the detection of artificially induced root fractures using cone-beam computed tomographic imaging. *J Endod* 2018;44:828–833.
15. Fox A, Basrani B, Kishen A, Lam EWN. A novel method for characterizing beam hardening artefacts in cone-beam computed tomographic images. *J Endod* 2018;44:869–874.
16. Martins LAC, Queiroz PM, Nejaim Y, de Faria Vasconcelos K, Groppo FC, Haiter-Neto F. Evaluation of metal artefacts for two CBCT devices with a new dental arch phantom. *Dentomaxillofac Radiol* 2020;49:20190385.
17. Katsumata A, Hirukawa A, Okumura S, et al. Effects of image artefacts on gray-value density in limited-volume cone-beam computerized tomography. *Oral Surg Oral Med Oral Pathol Oral Radiol Endod* 2007;104:829–836.
18. Wang ZJ. Bioceramic materials in endodontics. *Endodontic Topics* 2015;32:3–30.
19. Brito-Júnior M, Santos LA, Faria-e-Silva AL, Pereira RD, Sousa-Neto MD. Ex vivo evaluation of artefacts mimicking fracture lines on cone-beam computed tomography produced by different root canal sealers. *Int Endod J* 2014;47:26–31.
20. Pawar AM, Pawar S, Kfir A, Pawar M, Kokate S. Push-out bond strength of root fillings made with C-Point and BC sealer versus gutta-percha and AH Plus after the instrumentation of oval canals with the Self-Adjusting File versus WaveOne *Int Endod J* 2016;49:374–381.
21. Rabelo KA, Cavalcanti YW, de Oliveira Pinto MG, et al. Quantitative assessment of image artefacts from root filling materials on CBCT scans made using several exposure parameters. *Imaging Sci Dent* 2017;47:189–197.
22. Makeeva IM, Byakova SF, Novozhilova NE, et al. Detection of artificially induced vertical root fractures of different widths by cone beam computed tomography in vitro and in vivo. *Int Endod J* 2016;49:980–989.
23. Wolters WJ, Duncan HF, Tomson PL, et al. Minimally invasive endodontics: a new diagnostic system for assessing pulpitis and subsequent treatment needs. *Int Endod J* 2017;50:825–829.
24. Kim JH, Arita ES, Pinheiro LR, Yoshimoto M, Watanabe PCA, Cortes ARG. Computed tomographic artefacts in maxillofacial surgery. *J Craniofac Surg* 2018;29:e78–e80.
25. Bueno MR, Estrela C, De Figueiredo JA, Azevedo BC. Mapping strategy to diagnose root perforations near metallic intracanal posts by using cone beam computed tomography. *J Endod* 2011;37:85–90.
26. Hekmatian E, Karbasi Kheir M, Fathollahzade H, Sheikhi M. Detection of vertical root fractures using cone-beam computed tomography in the presence and absence of gutta-percha. *Scientific World Journal* 2018;2018:1920946.



# Evolutionary and Pan-genome Analysis of Three Important Black-pigmented Periodontal Pathogens

Pei Qi MENG<sup>1</sup>, Qian ZHANG<sup>2</sup>, Yun DING<sup>1</sup>, Jiu Xiang LIN<sup>3</sup>, Feng CHEN<sup>2</sup>

**Objective:** To analyse the pan-genome of three black-pigmented periodontal pathogens: *Porphyromonas gingivalis*, *Prevotella intermedia* and *Prevotella nigrescens*.

**Methods:** Pan-genome analyses of 66, 33 and 5 publicly available whole-genome sequences of *P. gingivalis*, *P. intermedia* and *P. nigrescens*, respectively, were performed using Pan-genome Analysis Pipeline software (version 1.2.1; Beijing Institute of Genomics, Chinese Academy of Sciences, Beijing, PR China). Phylogenetic trees were constructed based on the entire pan-genome and single nucleotide polymorphisms within the core genome. The distribution and abundance of virulence genes in the core and dispensable genomes were also compared in the three species.

**Results:** All three species possess an open pan-genome. The core genome of *P. gingivalis*, *P. intermedia* and *P. nigrescens* included 1001, 1514 and 1745 orthologous groups, respectively, which were mainly related to basic cellular functions such as metabolism. The dispensable genome of *P. gingivalis*, *P. intermedia* and *P. nigrescens* was composed of 2814, 2689 and 906 orthologous groups, respectively, and it was enriched in genes involved in pathogenicity or with unknown functions. Phylogenetic trees presented a clear separation of *P. gingivalis*, *P. intermedia* and *P. nigrescens*, verifying the reclassification of the black-pigmented species. Furthermore, the three species shared almost the same virulence factors involved in adhesion, proteolysis and evasion of host defences. Some of these virulence genes were conserved across species whereas others belonged to the dispensable genome, which might be acquired through horizontal gene transfer.

**Conclusion:** This study highlighted the usefulness of pan-genome analysis to infer evolutionary cues for black-pigmented species, indicating their homology and phylogenomic diversity.

**Key words:** core genome, pan-genome, *Porphyromonas gingivalis*, *Prevotella intermedia*, *Prevotella nigrescens*

*Chin J Dent Res* 2023;26(2):93–104; doi: 10.3290/j.cjdr.b4128023

1 Third Clinical Division, Peking University School and Hospital of Stomatology & National Clinical Research Center for Oral Diseases & National Engineering Laboratory for Digital and Material Technology of Stomatology & Beijing Key Laboratory of Digital Stomatology, Beijing, P.R. China.

2 Central Laboratory, Peking University School and Hospital of Stomatology & National Clinical Research Center for Oral Diseases & National Engineering Laboratory for Digital and Material Technology of Stomatology & Beijing Key Laboratory of Digital Stomatology, Beijing, P.R. China.

3 Department of Orthodontics, Peking University School and Hospital of Stomatology & National Clinical Research Center for Oral Diseases & National Engineering Laboratory for Digital and Material Technology of Stomatology & Beijing Key Laboratory of Digital Stomatology, Beijing, P.R. China.

**Corresponding author:** Dr Feng CHEN, Central Laboratory, Peking University School and Hospital of Stomatology, 22 Zhongguancun South Avenue, Haidian District, Beijing 100081, P.R. China. Tel: 86-10-82195773; Fax: 86-10-82195773. Email: chenfeng2011@hsc.pku.edu.cn

Black-pigmented, gram-negative anaerobes have been found to be associated with periodontal disease since they were first isolated in 1928<sup>1</sup>. Given that these anaerobes share similar biochemical features and form black colonies on blood agar, they were named as *Bacteroides melanogenica* prior to the 1990s. With advances in DNA sequencing, the underlying diversity within some of these black-pigmented anaerobes previously characterised as a single bacterial species became apparent. Through a systematic analysis using biochemical, physiological and immunological approaches, in addition to molecular DNA technologies, what was previously

This work was supported by the National Natural Science Foundation of China (Grant No. 81991501), the KCL and PKUHSC Joint Institute for Medical Research Fund (Grant No. BMU2020KCL003) and the Post-doctor Seed Funding from Peking University School and Hospital of Stomatology.

a single entity is now appreciated to contain two different genera, *porphyromonas* and *prevotella*<sup>2</sup>. Of the many species of *porphyromonas* and *prevotella*, *Porphyromonas gingivalis* (*P. gingivalis*) and *Prevotella intermedia* (*P. intermedia*) are considered major pathogens in periodontal infections in humans. Meanwhile, the heterogeneity within *P. intermedia* species has led to further biochemical and chemical studies, which have revealed two serotypes within the *P. intermedia* species. The newly discovered *P. intermedia*, which had another species identified within this assumed homogenous species, is what we now know as *Prevotella nigrescens* (*P. nigrescens*)<sup>3</sup>. *P. nigrescens*, which is also considered a periodontal pathogen, causes periodontitis by colonising on the tooth surface and triggering an overly aggressive immune response, resulting in inflammation of oral tissue.

In the last few decades, the development of high-throughput sequencing technology and bioinformatics has increased the availability of sequenced bacterial genomes. The first published whole-genome sequence of *P. gingivalis* and *P. intermedia* was *P. gingivalis* W83<sup>4</sup> and *P. intermedia* 17<sup>5</sup>, respectively. Since then, several whole-genome sequences covering various species of *porphyromonas* and *prevotella* genera have become available in the public domain. Analyses of the available genome data have the potential to provide insights into the evolution and phylogeny of these closely correlated black-pigmented strains.

The accumulation of genome sequences introduced the concept of a “pan-genome”<sup>6</sup>. The pan-genome is defined as the set of all the genes presented in an analysed dataset and comprises both core and dispensable genomes<sup>7</sup>. The core genome refers to the set of genes shared by almost all the genomes of the analysed dataset, whereas the dispensable genome describes the genes shared within only one or some genomes. Since the original proposal of the pan-genome, this concept has been widely used to account for the genomic diversity present within a given phylogenetic clade, including the heterogeneous genus *lactobacillus*<sup>8,9</sup>, *clostridium*<sup>10</sup>, and the species *escherichia coli*<sup>11</sup>, *pseudomonas aeruginosa*<sup>12</sup> and *streptococcus agalactiae*<sup>6</sup>.

However, despite the availability of several whole-genome sequences of black-pigmented species in public databases, no studies on the pan-genomics of these species are available. Although a few recent studies investigated the genomics of *P. gingivalis* and *P. intermedia*<sup>13-16</sup>, none performed comprehensive pan-genome analyses on these species. Thus, in the present study, the authors performed a large-scale, comparative genome and pan-genome analysis of black-pigmented species (*P. gingivalis*, *P. intermedia* and *P. nigrescens*)

using the publicly available whole-genome sequences of these species. Such genome-based analysis provides a detailed overview of the gene content of the core genome and pan-genome, and offers insight into phylogenomic relationships of these closely related clinically important species.

## Materials and methods

### Genome sequences

All the publicly available genome sequences of *P. gingivalis*, *P. intermedia* and *P. nigrescens* were obtained from the genome database of National Center for Biotechnology Information (NCBI). A total of 104 genome (draft and complete) sequences, including 66 *P. gingivalis*, 33 *P. intermedia* and 5 *P. nigrescens* genome sequences, which were submitted to the database prior to 12 October 2020, were used in this study. In addition, 19 genome sequences from bacteria in the bacteroides genus that were isolated from the human oral cavity were also downloaded and used as an outgroup for comparison in our analyses. All the sequences were from humans originating from diverse countries (USA, UK, South Korea, China, Japan, Sudan, Germany, Norway, Chile, Canada, Romania, Russia, Denmark and Hungary).

### Clustering and functional annotation of the core and dispensable genomes

The annotated protein sequences of 104 genomes were grouped into homogenous clusters using OrthoMCL (University of Pennsylvania, Philadelphia, PA, USA)<sup>17</sup> based on sequence similarity. The BLAST reciprocal best hit algorithm<sup>18</sup> was applied with the criterion of e-value < 1e<sup>-5</sup>, identity > 40% and length coverage of a gene > 50%, and Markov cluster algorithms<sup>19</sup> were employed with an inflation index of 1.5 to complete cluster analyses.

The functional category of each homogenous cluster was determined by performing BLASTp<sup>20</sup> against the Cluster of Orthologous Groups (COG) database (<http://www.ncbi.nih.gov/COG/>) with a criterion of e-value < 1e<sup>-5</sup> and identity > 40%. To elucidate whether the core genome was enriched in a particular function, the proportions of the COG categories in the core and dispensable genomes were compared. An enrichment analysis was performed with a chi-square test using SPSS version 20 (IBM, Armonk, NY, USA) to give statistical significance to the difference. *P* < 0.05 was considered significant.

### Statistical estimation of core genome and pan-genome size

Analyses of the pan-genome and core genome were undertaken using PGAP (version 1.2.1) software platform<sup>21</sup> for *P. gingivalis*, *P. intermedia* and *P. nigrescens*. The pan-genome and core genome were calculated as described previously<sup>22</sup> in an additive and reductive manner. Considering that core genes may be missed during genome sequencing and assembly, a correction step was introduced for the calculation of core genome size, in which any one gene that was absent in only one of the draft genomes was still regarded as a core gene<sup>23</sup>. The number of total genes/core genes provided by each added new genome depends on the selection of previously added genomes. For a given number of given strains (N), the number of all possible combinations is C(N<sub>total</sub>, N). N<sub>total</sub> represents the total number of genomes for a species. In this study, N<sub>total</sub> is 66, 33, and 5 for *P. gingivalis*, *P. intermedia* and *P. nigrescens*, respectively. If the value of C(N<sub>total</sub>, N) was greater than 8000, only 8000 random combinations were used. If fewer, all possible combinations were used. The final size of the pan- or core genomes was the mean value of all used combinations.

To perform statistical extrapolation to estimate the theoretical pan-genome and core genome size, a non-linear least-squares curve was used to fit the observed core genome and pan-genome sizes as a function of the number of analysed genomes. For the core genome extrapolation, an exponential decay function was used<sup>6</sup> where n is the genome number, κ and τ are fitting parameters and Ω is the extrapolated size of the core genome when n → ∞.

$$f(n) = \kappa \exp(-n/\tau) + \Omega$$

For the pan-genome, a Heaps' power law function was used, where n is the number of genomes used, a and b are fitting parameters and c is the growth exponent that indicates the speed at which the pan-genome is growing<sup>24</sup>.

$$f(n) = a + bn^c$$

Results were compared among *P. gingivalis*, *P. intermedia* and *P. nigrescens*. For visual comparison, genome development trend maps were generated using OriginLab software (<https://www.originlab.com/>) (Northampton, MA, USA).

### Phylogenetic analysis

For phylogenetic analyses, the PGAP pipeline used both the pan-genome profile and single nucleotide polymorphisms (SNPs) information in the core genome. Every set of orthologous genes found in all of the genomes were aligned separately using the multiple alignment tool MUSCLE (University of California, Berkeley, CA, USA)<sup>25</sup>. SNPs were extracted from these alignments and concatenated to form a multiple sequence alignment. Based on the whole pan-genome and SNPs within the core genome, phylogenetic trees were constructed using various methods, including an unweighted pair-group method with arithmetic means (UPGMA), neighbour-joining (NJ) and maximum likelihood (ML).

Additionally, a phylogenetic tree was constructed based on the 16S ribosome RNA (16S rRNA) gene, which is the most widely used gene marker in bacterial phylogenetic analysis for its functionally conserved feature. The 16S rRNA sequences with a length between 1,400 and 1,700 nt and an RNAmmer score above 1,700 were identified using RNAmmer (University of Oslo, Oslo, Norway)<sup>26</sup>. MEGA-7.0 software (King Abdulaziz University, Jeddah, Saudi Arabia)<sup>27</sup> was used to align the 16S rRNA sequences and construct an NJ tree with the Kimura 2-parameter model. Bootstrap values of each branch were calculated 500 times. All the trees were visualised using Evolview<sup>28</sup> (Beijing Institute of Genomics, Chinese Academy of Sciences, Beijing, PR China) (<http://www.evolgenius.info/evolview.html>).

To further reaffirm that the genomes of each strain did indeed belong to the assigned species, average nucleotide identity (ANI) values were calculated for all strains using the popular JSpecies package (Institut Mediterrani d'Estudis Avançats, Esporles, Spain)<sup>29</sup>. The ANI-based all-vs-all matrix was presented in a heatmap using HemI software (Huazhong University of Science and Technology, Wuhan, PR China)<sup>30</sup> (<http://hemi.bio-cuckoo.org/down.php>).

### Analysis of virulence factors

To explore the distribution of virulence factors in the black-pigmented bacterial species, we reviewed the available literature and summarised the virulence factors of *P. gingivalis*, *P. intermedia* and *P. nigrescens* from previous publications<sup>15,31-36</sup>. The genome annotation reports for each strain were downloaded from the NCBI database (<ftp://ftp.ncbi.nih.gov/genomes/all/>), and the authors searched for the relevant genes associated with these virulence factors. The distribution and abundance of virulence genes in 66 *P. gingivalis*, 33 *P. intermedia* and

5 *P. nigrescens* genomes were displayed as a heatmap using HemI software. The abundance of virulence genes in the core and dispensable genomes was also compared in *P. gingivalis*, *P. intermedia* and *P. nigrescens*.

## Results and discussion

### Distribution of homogenous clusters

Detailed information regarding the 66 *P. gingivalis*, 33 *P. intermedia* and 5 *P. nigrescens* strains is shown in Supplementary Table S1 (provided on request). The genome size of *P. nigrescens* (mean 2.85 Mb and median 2.84 Mb) and *P. intermedia* (mean 2.79 Mb and median 2.78 Mb) is larger than that of *P. gingivalis* (mean 2.32 Mb and median 2.33 Mb). The genomes also vary substantially with regard to their number of genes. The number of genes was lowest for *P. gingivalis* with a mean of 2073, followed by 2324 for *P. intermedia* and 2407 for *P. nigrescens*; however, all three species have a relatively consistent genomic guanine and cytosine (GC) content, with *P. gingivalis* having the highest (range 48.1% to 49.1%), followed by *P. intermedia* (range 43.2% to 43.9%) and *P. nigrescens* (range 42.5% to 42.8%). By comparing the proteins annotated in the genomes of three species, 3815, 4203 and 2651 homologous clusters were identified in *P. gingivalis*, *P. intermedia* and *P. nigrescens*, respectively. Among these, 1001, 1514 and 1745 clusters comprised the core genome, while the remaining 2814, 2689 and 906 clusters comprised the dispensable genome (Table 1).

To identify functional differences between genes in the core and dispensable genomes, genes were classified according to their predicted function based on COG categories. The abundance of each COG category was plotted and compared in Figs 1a, 1c and 1e. In all three species, the highest numbers of genes in the core genome were related to translation, ribosomal structure and biogenesis (J). This was consistent with some species, such as *streptococcus pneumoniae*<sup>37</sup> and the genus *clostridium*<sup>10</sup>, while other species, such as *staphylococcus aureus*, *salmonella enterica*, *escherichia coli*, *pseudomonas aeruginosa* and *acinetobacter baumannii*, showed amino acid transport and metabolism (E) as the most abundant category in their core genome<sup>37</sup>.

With the exception of the categories P (inorganic ion transport and metabolism) and Q (secondary metabolites biosynthesis, transport and catabolism) in *P. nigrescens*, the enriched genes in the core genome were involved in almost all the COG categories of metabolism, including energy production and conversion (C), carbohydrate transport and metabolism (G), amino acid

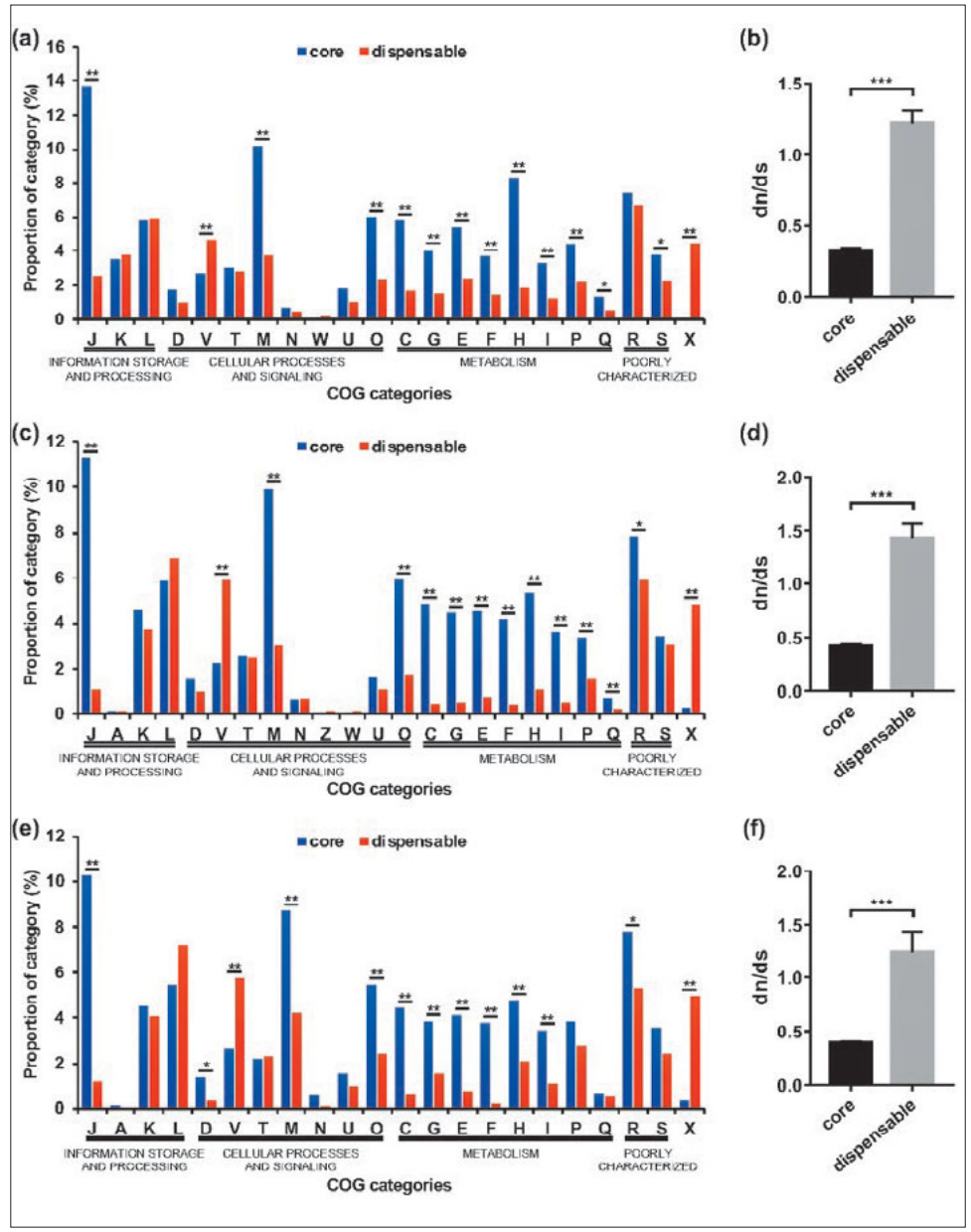
transport and metabolism (E), nucleotide transport and metabolism (F), coenzyme transport and metabolism (H), and lipid transport and metabolism (I); however, the enriched genes in the dispensable genome were included in poorly characterised categories, such as genes with unknown functions (S) in *P. gingivalis*, and only general function prediction (R) in *P. intermedia* and *P. nigrescens*. Similar enrichment in genes with no assigned function was reported previously in the dispensable genome of other organisms<sup>6,38,39</sup>, and these genes may represent new virulent factors or interaction features of the oral microbiome. For all three species, statistically significant differences between the core and dispensable genome were also found in COG categories J (translation, ribosomal structure and biogenesis), M (cell wall/membrane/envelope biogenesis), O (posttranslational modification, protein turnover, chaperones), V (defence mechanisms) and X (mobilome: prophages, transposons). The core genome was enriched in the former three categories, whereas the dispensable genome was enriched in the latter two. In addition, we only observed in *P. nigrescens* that genes involved in cell cycle control, cell division and chromosome partitioning (D) comprised a significantly higher proportion of the core genome compared to the dispensable genome. Thus, genes involved in basic functions in life maintenance of the organism were likely to be more abundant in the core genome, whereas those related to pathogenicity or unknown functions were more likely to be enriched in the dispensable genome.

To compare the evolutionary pressure of genes in the core genome and dispensable genome, we calculated the ratio of non-synonymous to synonymous substitutions (dn/ds) for *P. gingivalis*, *P. intermedia* and *P. nigrescens*. The dn/ds ratio is commonly regarded as one of the most popular and reliable measures of the strength and mode of natural selection acting on protein coding sequences, with dn/ds > 1 indicating positive (adaptive or diversifying) selection, dn/ds = 1 indicating neutral evolution and dn/ds < 1 indicating negative (purifying) selection<sup>40</sup>. In the present study, the mean value of dn/ds was 1.22, 1.43 and 1.24 for the dispensable genome of *P. gingivalis*, *P. intermedia* and *P. nigrescens*, respectively, which was significantly higher than that of the core genome ( $P < 0.001$ ), whose dn/ds value was below 1 in all three species (Figs 1b, 1d and 1f). It can be inferred that core genes are more conserved since they are involved in basic functions of life maintenance, whereas in the dispensable genome, the non-synonymous rate is significantly higher than that of the synonymous rate, leading to adaptive protein evolution to survive sudden environmental changes.

**Table 1** Summary of the pan-genome of *P. gingivalis*, *P. intermedia* and *P. nigrescens*.

| Number of clusters of orthologous genes | <i>P. gingivalis</i> | <i>P. intermedia</i> | <i>P. nigrescens</i> |
|---|----------------------|----------------------|----------------------|
| Mean number of genes                    | 3,815                | 4,203                | 2,651                |
| Core                                    | 1,001 (26%)          | 1,514 (36%)          | 1,745 (66%)          |
| Dispensable                             | 2,814 (74%)          | 2,689 (64%)          | 906 (34%)            |
| Strain-specific                         | 759 (20%)            | 815 (19%)            | 488 (18%)            |

**Fig 1** Functional analysis. Comparison of the abundance for each COG category and dn/ds values of homogenous clusters in the core and dispensable genome in *P. gingivalis* (a and b), *P. intermedia* (c and d) and *P. nigrescens* (e and f). The asterisks indicate those that are significantly different (\* $P < 0.05$ , \*\* $P < 0.01$ , \*\*\* $P < 0.001$ ). For all three species, the enriched genes in the core genome were involved in almost all the COG categories of metabolism. The dispensable genome was enriched in the genes related to defence (category V) and mobilome (category X) (a, c and e). The mean value of dn/ds for the core genome was below 1 in all three species, which was significantly lower than that of the dispensable genome (b, d and f). See Supplementary Table S3 (provided on request) for COG codes.



*Pan-genome and core genome analysis*

The pan-genome and core genome development plots of *P. gingivalis*, *P. intermedia* and *P. nigrescens* are shown in Fig 2. All three species were found to possess an open

pan-genome that continues to increase in the number of genes as new genomes are added (Figs 2a, 2c and 2e). On average, with each new genome sequenced, there were additions of 31, 68 and 145 genes to the pan-genome of *P. gingivalis*, *P. intermedia* and *P. nigrescens*, respectively.

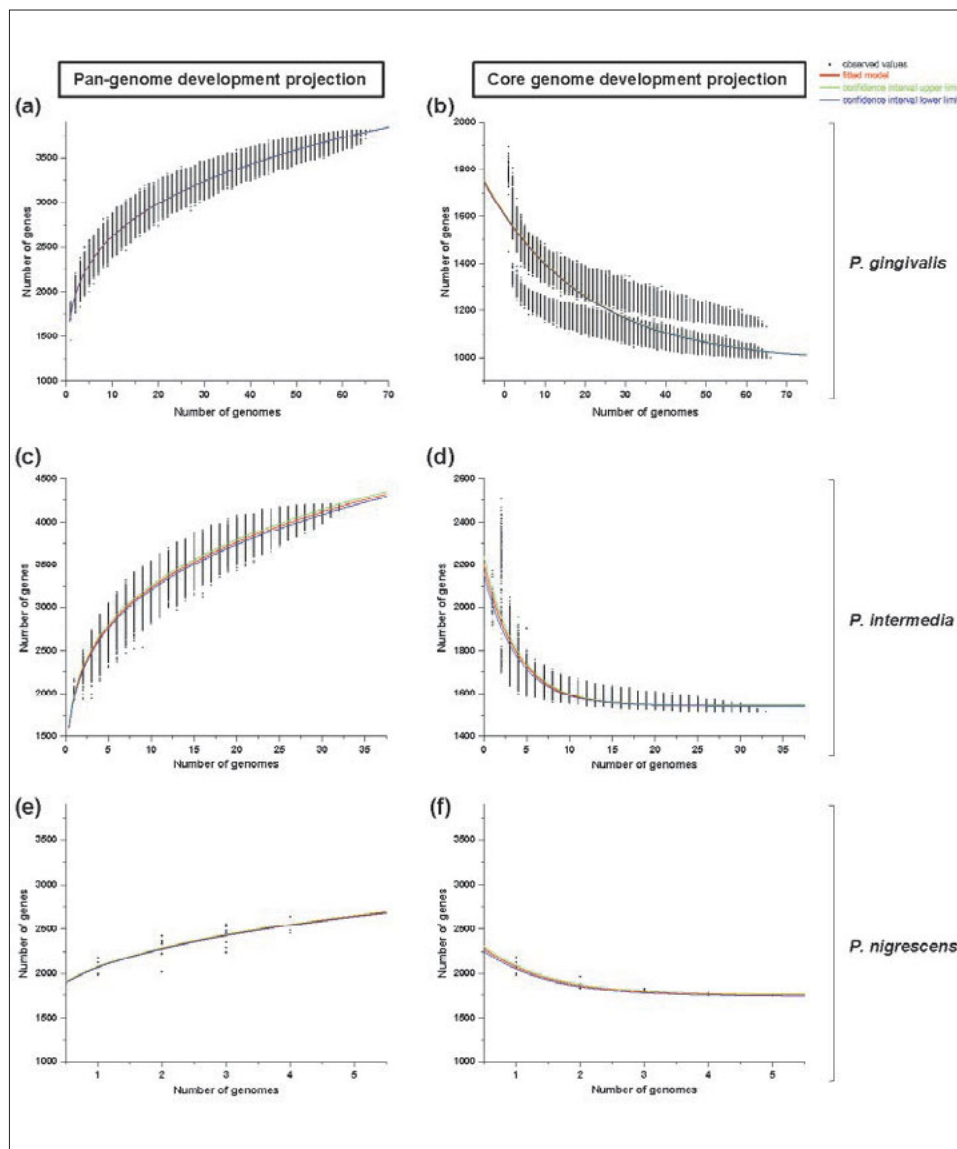


**Fig 2** Pan-genome and core genome development plot projections for *P. gingivalis* (a and b), *P. intermedia* (c and d) and *P. nigrescens* (e and f). In the six panels, each black point represents the size of the pan-genome or core genome calculated from random combinations and iterations of strains as genomes are included in the analysis. For pan-genome development plot extrapolation: the red curve shows the fitted exponential Heaps' law function, and the green and blue curves indicate the upper and lower boundary of the 95% confidence interval. For all three species, the extrapolated curves continue to increase, indicating that they all have an open pan-genome. For core genome development plot extrapolation: the red curve shows the fitted exponential decay function, and the green and blue curves indicate the upper and lower boundary of the 95% confidence interval. The size of the core genome decreases at a slower rate with the addition of each strain genome, and remains relatively constant even as more genomes are added.

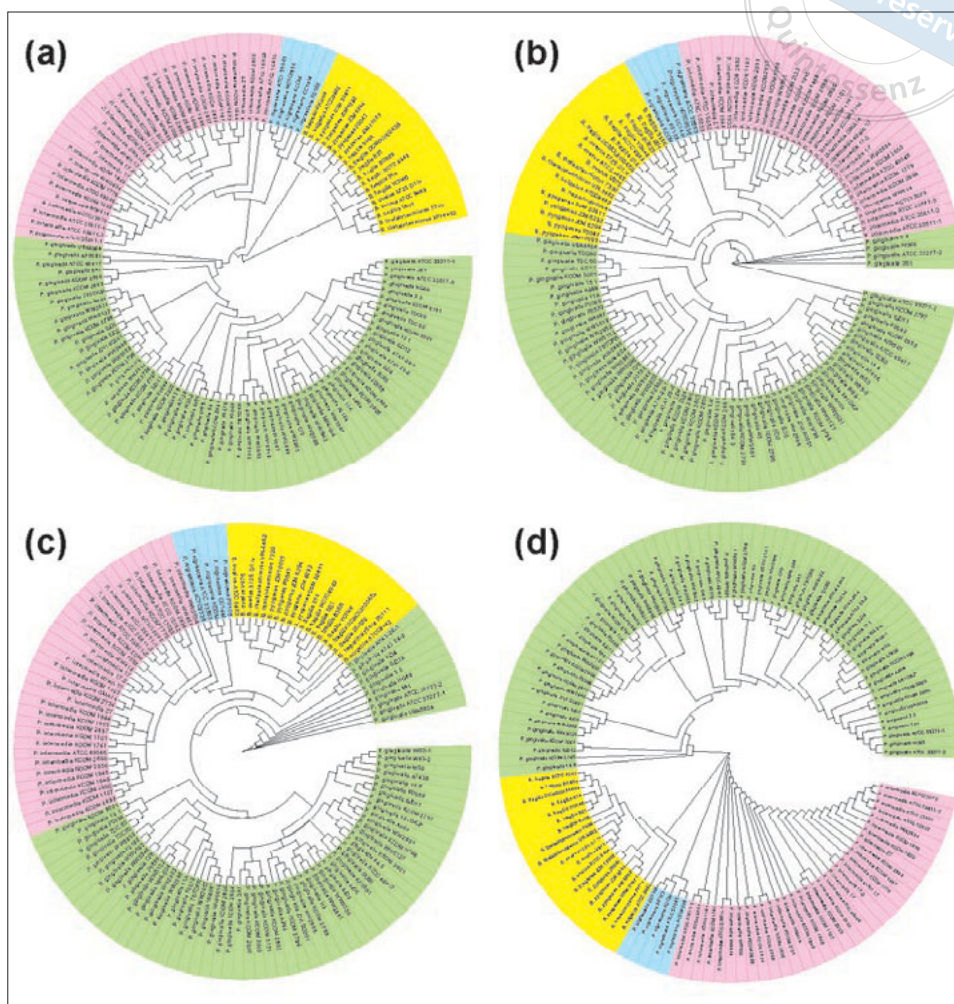
The significant difference should be due to the variation in the number of sequenced genomes. Since the number of *P. nigrescens* genomes is much smaller, it is anticipated that with the addition of further genomes, more new genes are likely to be added to the pool.

Aside from these black-pigmented species, an open pan-genome is also found in *streptococcus agalactiae*<sup>6</sup>, *escherichia coli*<sup>11</sup>, *streptococcus pneumoniae*<sup>37</sup> and *streptococcus mutans*<sup>22</sup>. These bacterial species exhibit high genome expansion plasticity through the lateral exchange of genetic material to adapt to variable environments. On the contrary, some bacteria display a closed pan-genome, such as *staphylococcus aureus*<sup>41</sup>, *staphylococcus lugdunensis*<sup>42</sup>, *salmonella enterica*<sup>43</sup> and *yersinia pestis*<sup>44</sup>. For these species, any acquisition of

foreign genes seems to be largely restricted to bacteriophages and plasmids.

The core genome of the three species also displayed a similar evolution. The core genome size decreased at a slower rate with the addition of each new sequence, and then remained relatively constant even as more genomes were added (Figs 2b, 2d and 2f). The extrapolated core genome sizes were 980 (95% confidence interval 979–980 genes), 1543 (95% confidence interval 1542–1543 genes) and 1746 (95% confidence interval 1736–1756 genes) genes for *P. gingivalis*, *P. intermedia* and *P. nigrescens*, respectively (Supplementary data 1, Table S1, provided on request). This suggested that all three species are defined by a limited number of core genes and display a degree of variability in dispensable genes.

**Fig 3** Circular phylogenetic trees illustrating the genetic relationships between strains of black-pigmented species. **(a)** The tree was built based on the pan-genome using the UPGMA method. **(b)** The tree was built based on the pan-genome using the neighbour-joining method. **(c)** The tree was built based on SNPs within the core genome using the maximum likelihood method. **(d)** The tree was built based on the 16S rRNA gene using the maximum likelihood method. For each tree, the leaf colour of light green, pink, light blue and yellow represents *P. gingivalis*, *P. intermedia*, *P. nigrescens* and species of *Bacteroides*, respectively. All the trees show that *P. gingivalis*, *P. intermedia*, *P. nigrescens* and species of *Bacteroides* form four clearly separated clusters within the phylogenetic trees, and there is a closer relationship between *P. intermedia* and *P. nigrescens*.



### Phylogenetic analysis

The phylogenetic tree is a common methodology to infer the evolutionary relationship between different species. To confirm the close phylogenesis of *P. gingivalis*, *P. intermedia* and *P. nigrescens*, we constructed phylogenetic trees for the three species together based on the pan-genome profile (Figs 3a and b), SNP information for the core genome (Fig 3c) and 16S rRNA gene (Fig 3d). We compared these trees and found that although they were not completely identical, they exhibited considerably similar topology. All the trees showed a clear separation in *P. gingivalis*, *P. intermedia*, *P. nigrescens* and species of *Bacteroides*. They all formed monophyletic branches, and strains of the same species were closest to each other. It is worth noting that there is a close evolutionary relationship between *P. intermedia* and *P. nigrescens* as they originate from the same branch in all the phylogenetic trees. Among the four trees based on different genome information with diverse algorithms, the pan-

genome tree using the unweighted pair group method with arithmetic mean (UPGMA) exhibited a higher resolution at the species level, with some already known closely related isolates located in the adjacent branches, such as *P. intermedia* ATCC 25611-1, *P. intermedia* ATCC 25611-2 and *P. intermedia* ATCC 25611-3. This verified not only the superiority of the UPGMA algorithm in constructing phylogenetic trees for closely related species, but also the advantage of the pan-genome in phylogenetic analysis, especially for species with incomplete or unavailable 16S rRNA gene sequences.

To reveal the influences of geographic locations on the evolution of *P. gingivalis*, *P. intermedia* and *P. nigrescens*, we referred to the NCBI websites and previously published studies for the geographic locations of each taxon and combined the geographic locations with the phylogenetic tree. The geographic locations of the analysed taxa included the USA, UK, South Korea, China, Japan, Sudan, Germany, Norway, Chile, Canada, Romania, Russia, Denmark and Hungary, although this

information was missing for a few taxa. The strains with different geographic locations are scattered throughout different branches on the phylogenetic trees, which suggested that adapting to different countries did not play an essential role in the evolutionary history of the black-pigmented bacteria.

Furthermore, the average nucleotide identity (ANI) value, which is a widely accepted genome-based method for species delineation, was calculated for all the strains and represented as a heatmap (Supplementary Figure, provided on request). The heatmap shows the degree of similarity between strains based on the ANI values of the whole-genome sequences. In agreement with phylogenetic analysis, the resulting ANI values of *P. gingivalis*, *P. intermedia* and *P. nigrescens* were distributed between 97.49% and 99.99%, 95.16% and 99.99%, 96.93% and 99.91% (Supplementary data 2, Excel S1, provide on request), respectively, meeting the cut-off criteria of 95% identity as suggested previously<sup>29</sup>. The ANI values between the three species and *Bacteroides* were distributed between 63.76% and 71.78% (Supplementary data 2, Excel S1), which is much lower than the cut-off of 95% similarity, further confirming the previously modified nomenclature for these closely related black-pigmented bacteria. It is worth noting that the ANI values of *P. intermedia* and *P. nigrescens* were distributed between 84.12% and 85.92% (Supplementary data 2, Excel S1), which was much higher than that of other different species, further validating their close evolutionary relationship.

### Distribution of virulence factors

We reviewed the literature and found that *P. gingivalis*, *P. intermedia* and *P. nigrescens* possess a range of virulence factors involved in adhesion, proteolysis and evasion of host defences<sup>2,32-34</sup>. The three species share almost the same virulence factors, including capsule, lipopolysaccharide (LPS) and hemagglutinin<sup>32-34</sup>. Some virulence factors are conserved in all three species, such as rubrerythrin (Fig 4a), which is a non-heme iron protein that protects many air-sensitive bacteria against oxidative stress<sup>45</sup>. Genes coding for serine phosphatase (SerB), which has been shown to inhibit the biosynthesis of cytokines in gingival epithelial cells<sup>33</sup>, were also conserved in *P. gingivalis*, *P. intermedia* and *P. nigrescens* (Fig 4a). For most virulence factors, the level of conservation varies with the aspect of pathogenicity. The involved genes have a relatively conserved part and a strain-specific part (Fig 4a).

To invade periodontal tissues, the periodontal pathogens need to adhere to the surface of the tooth or

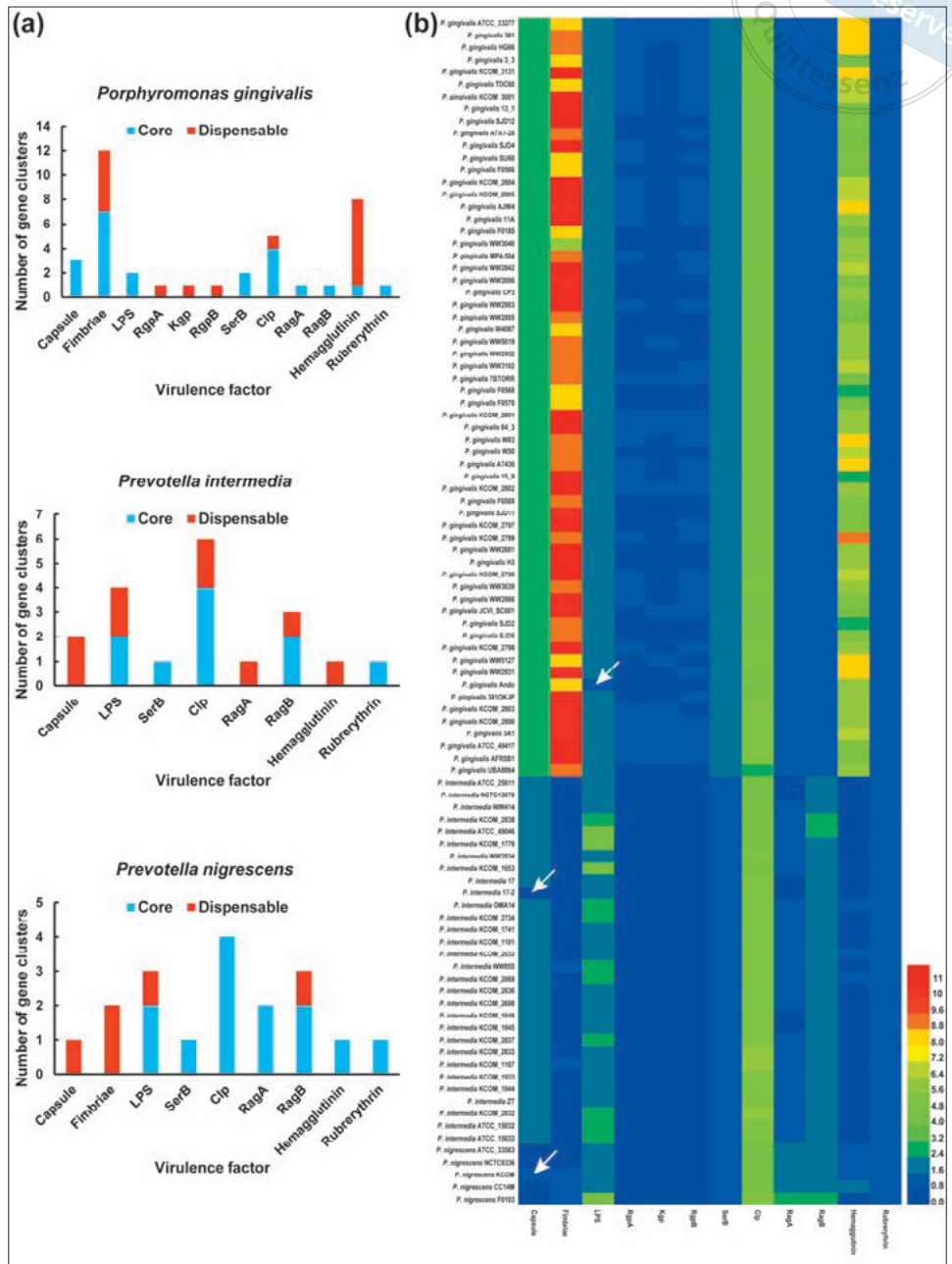
mucosa, which is facilitated by a repertoire of adhesins, including fimbriae and hemagglutinin<sup>46</sup>. Fimbriae are thin, filamentous, cell-surface protrusions that facilitate adherence of the periodontal pathogens to salivary proteins, extracellular matrix and bacteria of either the same or other species. Through the fimbriae, they can attach to the early colonising bacteria and participate in the developing biofilm structure. Hemagglutinin is a type of non-fimbrial adhesin that agglutinates erythrocytes and promotes adherence to host tissue, including endothelial cells. In *P. gingivalis* strains, some fimbriae and hemagglutinin genes are conserved, whereas others only exist in certain strains. In *P. nigrescens*, genes coding for fimbriae and hemagglutinin belong to the dispensable genome and the core genome, respectively (Fig 4a).

Apart from adhesins, LPS is also a key virulence factor in the development of periodontitis. LPS is a major component of the outer cell membrane of gram-negative bacteria, including periodontal pathogens *P. gingivalis*, *P. intermedia* and *P. nigrescens*. It is recognised by the host and potently activates host inflammatory and innate defence responses<sup>34</sup>. LPS has been demonstrated to be a stimulator of proinflammatory responses and bone resorption in animal models of periodontitis<sup>47,48</sup>. In *P. gingivalis*, both gene copies coding for LPS belong to the core genome. Notably, one of them has the conservation value of 65 and is only absent in *P. gingivalis* Ando strain (Fig 4b). Since the genome of *P. gingivalis* Ando is not completely assembled (scaffold level), some genes might have been missed during sequencing and assembly of the draft genome. Thus, this gene is still regarded as conserved. In *P. intermedia* and *P. nigrescens*, there are also two gene copies coding for LPS shared by all the strains, while other genes are only found in one or several strains (Supplementary data 3, Excel S2, provided on request).

Like LPS, the capsule is an outer envelope structure that lies outside bacterial cells. Many bacterial strains have been found to possess capsules, such as *Streptococcus pneumoniae*, whose capsule was verified as an important virulence factor in the early 20th century<sup>49</sup>. Similar to its functions in other bacteria, the capsule of *P. gingivalis* protects the bacteria from host immune clearance. It has been reported that encapsulated strains of *P. gingivalis* are more resistant to phagocytosis by polymorphonuclear leukocytes than non-encapsulated strains<sup>50</sup>. In this study, all three genes coding for capsule biosynthesis proteins are conserved in *P. gingivalis*, whereas in *P. intermedia* and *P. nigrescens*, genes coding for the capsule belong to the dispensable genome. Interestingly, higher conservation



**Fig 4** Distribution of virulence factors. **(a)** The overall number of putative virulence genes and their core and dispensable fractions are indicated for each virulence gene. Both SerB and rubrerythrin are conserved in all three species, whereas for most virulence factors, there is a conserved part and a dispensable part. **(b)** Heatmap illustrating the distribution and abundance of putative virulence genes across important black-pigmented strains. The gene copy number of each virulence gene is indicated by the colour key ranging from blue (absent) to red. Strains are graphed top to bottom in the same order as they appear in the phylogeny based on the pan-genome using UPGMA (Fig 3a). The white arrows highlight the representative strains. In *P. intermedia*, genes coding for the capsule show a high conservation level. Both of the two gene copies are only absent in *P. intermedia* 17-2, whereas in *P. nigrescens*, the single gene coding for the capsule is specific to *P. nigrescens* KCOM. In *P. gingivalis*, one of the genes coding for LPS is only absent in *P. gingivalis* Ando, whose genome is not completely assembled (scaffold level). Thus, we still regard this gene as conserved.



levels of the capsule were found in *P. intermedia*. Both gene copies coding for the capsule are only absent in *P. intermedia* 17-2 strain (Fig 4b), which is a complete genome, whereas in *P. nigrescens*, the single gene coding for the capsule is specific to *P. nigrescens* KCOM (Fig 4b). It seems that both genes coding for LPS and capsule were conserved in *P. gingivalis* but showed lower conservation levels in *P. intermedia* and *P. nigrescens*, which is consistent with previous studies reporting that LPS and capsule are only found in certain strains of *P. intermedia* and *P. nigrescens*, especially those isolated from periodontitis patients<sup>15</sup>.

Another major virulence factor in black-pigmented periodontal pathogens are proteases. The most important proteases in *P. gingivalis* are gingipains, which account for 85% of the extracellular proteolytic activities of *P. gingivalis*<sup>51</sup>. Aside from their role in degrading host tissue, gingipains are also involved in enhancing the interactions of *P. gingivalis* with other periodontal pathogens to facilitate bacterial survival and biofilm formation<sup>52</sup>. Based on their specificity, gingipains can be divided into two groups: arginine-specific (Rgp) and lysine-specific (Kgp). Rgp is further subdivided into RgpA and RgpB based on structure. All the genes coding

for RgpA, RgpB and Kgp are single-copy and belong to the dispensable genome (Figs 4a and b). Interestingly, genes coding for RgpA and Kgp are attributed to the same homogenous cluster in this study (Supplementary data 3, Excel S2, provided on request), indicating their sequence similarity. This is consistent with a previous report that found RgpA and Kgp have a similar structure and close molecular weights<sup>35</sup>, whereas RgpB has a smaller molecular weight and lacks the C-terminal hemagglutinin domain compared with RgpA and Kgp<sup>53</sup>.

Although gingipains are specific to *P. gingivalis*, another proteolytic enzyme belonging to the caseinolytic protease (Clp) family is ubiquitous among various organisms<sup>54</sup>. The Clp family has several members, including ClpB, ClpC, ClpP and ClpX, all of which play an important role in colonisation and survival in the oral cavity. It has been reported that ClpC, ClpP and ClpX are necessary for *P. gingivalis* to enter host epithelial cells, and the absence of these proteases can result in diminished tolerance to high temperature in *P. gingivalis*. ClpB does not play a role in entry, but is required for intracellular replication and survival in *P. gingivalis*<sup>55</sup>. In this study, all three species had an intact repertoire of the four gene copies coding for ClpB, ClpC, ClpP and ClpX in the core genome (Fig 4a and Supplementary data 3, Excel S2), which is consistent with a previous study that reported that Clp proteases were highly conserved<sup>54</sup>, indicating the importance of the Clp family in *P. gingivalis*, *P. intermedia* and *P. nigrescens*.

## Conclusion

Pan-genome analysis at the intraspecies level of three clinically important, black-pigmented periodontal pathogens was performed. We identified an open pan-genome structure for all three species. Phylogenetic analysis presented a clear separation of *P. gingivalis*, *P. intermedia*, *P. nigrescens* and species of *Bacteroides*, verifying the reclassification of these black-pigmented species. All three species were found to share almost the same virulence factors involved in adhesion, proteolysis and evasion of host defences. Genes coding for these virulence factors are flexible, displaying both strain specificity and universality. Various conservation levels of virulence genes indicated that the different strains of *P. gingivalis*, *P. intermedia* and *P. nigrescens* inherited a basic package of genes that enables them to adapt to the complicated oral environment and cause disease; however, this basic gene package diverged under different conditions and the genes of different functions evolved at different rates. The dataset setup in this study can

act as a powerful framework for the addition of further sequenced strains, enabling the refinement of the pan-genome. The tools and approaches used could also be applied as a pan-genomics framework to other species in future studies.

## Conflicts of interest

The authors declare no conflicts of interest related to this study.

## Author contribution

All authors contributed to the study conception and design. Dr Pei Qi MENG contributed to the functional annotation and phylogenetic analysis and drafted the manuscript; Dr Qian ZHANG contributed to the data collection and analysis. All authors approved the final version of the manuscript.

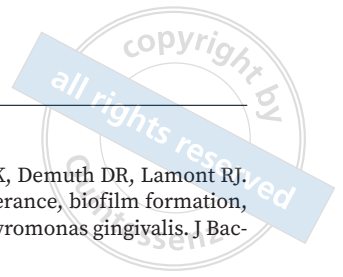
(Received Jun 28, 2022; accepted Mar 2, 2023)

## References

- Dahlén GG. Black-pigmented gram-negative anaerobes in periodontitis. *FEMS Immunol Med Microbiol* 1993;6:181–192.
- Lang NP, Lindhe J. *Clinical Periodontology and Implant Dentistry, Two-Volume Set*. Chichester: John Wiley & Sons, 2015.
- Shah HN, Gharbia SE. Biochemical and chemical studies on strains designated *Prevotella intermedia* and proposal of a new pigmented species, *Prevotella nigrescens* sp. nov. *Int J Syst Bacteriol* 1992;42:542–546.
- Nelson KE, Fleischmann RD, DeBoy RT, et al. Complete genome sequence of the oral pathogenic bacterium *Porphyromonas gingivalis* strain W83. *J Bacteriol* 2003;185:5591–5601.
- Nambu T, Yamane K, Maruyama H, Mashimo C, Yamanaka T. Complete genome sequence of *Prevotella intermedia* strain 17-2. *Genome Announc* 2015;3:e00951-15.
- Tettelin H, Massignani V, Cieslewicz MJ, et al. Genome analysis of multiple pathogenic isolates of *Streptococcus agalactiae*: Implications for the microbial “pan-genome”. *Proc Natl Acad Sci U S A* 2005;102:13950–13955.
- Medini D, Donati C, Tettelin H, Massignani V, Rappuoli R. The microbial pan-genome. *Curr Opin Genet Dev* 2005;15:589–594.
- Sun Z, Harris HM, McCann A, et al. Expanding the biotechnology potential of lactobacilli through comparative genomics of 213 strains and associated genera. *Nat Commun* 2015;6:8322.
- Inglis RC, Meile L, Stevens MJA. Clustering of pan- and core-genome of *Lactobacillus* provides novel evolutionary insights for differentiation. *BMC Genomics* 2018;19:284.
- Udaondo Z, Duque E, Ramos JL. The pangenome of the genus *Clostridium*. *Environ Microbiol* 2017;19:2588–2603.
- Rasko DA, Rosovitz MJ, Myers GS, et al. The pangenome structure of *Escherichia coli*: Comparative genomic analysis of *E. coli* commensal and pathogenic isolates. *J Bacteriol* 2008;190:6881–6893.

12. Mosquera-Rendón J, Rada-Bravo AM, Cárdenas-Brito S, Corredor M, Restrepo-Pineda E, Benítez-Páez A. Pangenome-wide and molecular evolution analyses of the *Pseudomonas aeruginosa* species. *BMC Genomics* 2016;17:45.
13. Chen T, Siddiqui H, Olsen I. In silico comparison of 19 *Porphyromonas gingivalis* strains in genomics, phylogenetics, phylogenomics and functional genomics. *Front Cell Infect Microbiol* 2017;7:28.
14. Chen T, Siddiqui H, Olsen I. Comparative genomics and proteomics of 13 *Porphyromonas gingivalis* strains. *J Oral Microbiol* 2015;7:29008.
15. Zhang Y, Zhen M, Zhan Y, Song Y, Zhang Q, Wang J. Population-genomic insights into variation in *Prevotella intermedia* and *Prevotella nigrescens* isolates and its association with periodontal disease. *Front Cell Infect Microbiol* 2017;7:409.
16. Ruan Y, Shen L, Zou Y, et al. Comparative genome analysis of *Prevotella intermedia* strain isolated from infected root canal reveals features related to pathogenicity and adaptation. *BMC Genomics* 2015;16:122.
17. Fischer S, Brunk BP, Chen F, et al. Using OrthoMCL to assign proteins to OrthoMCL-DB groups or to cluster proteomes into new ortholog groups. *Curr Protoc Bioinformatics* 2011;35:6.12.1-6.12.19.
18. Moreno-Hagelsieb G, Latimer K. Choosing BLAST options for better detection of orthologs as reciprocal best hits. *Bioinformatics* 2008;24:319–324.
19. Enright AJ, Van Dongen S, Ouzounis CA. An efficient algorithm for large-scale detection of protein families. *Nucleic Acids Res* 2002;30:1575–1584.
20. Altschul SF, Gish W, Miller W, Myers EW, Lipman DJ. Basic local alignment search tool. *J Mol Biol* 1990;215:403–410.
21. Zhao Y, Wu J, Yang J, Sun S, Xiao J, Yu J. PGAP: Pan-genomes analysis pipeline. *Bioinformatics* 2012;28:416–418.
22. Meng P, Lu C, Zhang Q, Lin J, Chen F. Exploring the genomic diversity and cariogenic differences of *Streptococcus mutans* strains through pan-genome and comparative genome analysis. *Curr Microbiol* 2017;74:1200–1209.
23. Song L, Wang W, Conrads G, et al. Genetic variability of *mutans streptococci* revealed by wide whole-genome sequencing. *BMC Genomics* 2013;14:430.
24. Heaps HS. *Information Retrieval: Computational and Theoretical Aspects*. New York: Academic Press, 1978.
25. Edgar RC. MUSCLE: Multiple sequence alignment with high accuracy and high throughput. *Nucleic Acids Res* 2004;32:1792–1797.
26. Lagesen K, Hallin P, Rødland EA, Staerfeldt HH, Rognes T, Ussery DW. RNAmmer: Consistent and rapid annotation of ribosomal RNA genes. *Nucleic Acids Res* 2007;35:3100–3108.
27. Kumar S, Stecher G, Tamura K. MEGA7: Molecular Evolutionary Genetics Analysis Version 7.0 for bigger datasets. *Mol Biol Evol* 2016;33:1870–1874.
28. Zhang H, Gao S, Lercher MJ, Hu S, Chen WH. EvolView, an online tool for visualizing, annotating and managing phylogenetic trees. *Nucleic Acids Res* 2012;40:W569–W572.
29. Richter M, Rosselló-Móra R. Shifting the genomic gold standard for the prokaryotic species definition. *Proc Natl Acad Sci U S A* 2009;106:19126–19131.
30. Deng W, Wang Y, Liu Z, Cheng H, Xue Y. HemI: A toolkit for illustrating heatmaps. *PLoS One* 2014;9:e111988.
31. Okamoto M, Maeda N, Kondo K, Leung KP. Hemolytic and hemagglutinating activities of *Prevotella intermedia* and *Prevotella nigrescens*. *FEMS Microbiol Lett* 1999;178:299–304.
32. Zenobia C, Hajishengallis G. *Porphyromonas gingivalis* virulence factors involved in subversion of leukocytes and microbial dysbiosis. *Virulence* 2015;6:236–243.
33. Sochalska M, Potempa J. Manipulation of neutrophils by *Porphyromonas gingivalis* in the development of periodontitis. *Front Cell Infect Microbiol* 2017;7:197.
34. Mysak J, Podzimek S, Sommerova P, et al. *Porphyromonas gingivalis*: Major periodontopathic pathogen overview. *J Immunol Res* 2014;2014:476068.
35. Jia L, Han N, Du J, Guo L, Luo Z, Liu Y. Pathogenesis of important virulence factors of *Porphyromonas gingivalis* via toll-like receptors. *Front Cell Infect Microbiol* 2019;9:262.
36. Xu W, Zhou W, Wang H, Liang S. Roles of *Porphyromonas gingivalis* and its virulence factors in periodontitis. *Adv Protein Chem Struct Biol* 2020;120:45–84.
37. Park SC, Lee K, Kim YO, Won S, Chun J. Large-scale genomics reveals the genetic characteristics of seven species and importance of phylogenetic distance for estimating pan-genome size. *Front Microbiol* 2019;10:834.
38. Galardini M, Mengoni A, Brilli M, et al. Exploring the symbiotic pangenome of the nitrogen-fixing bacterium *Sinorhizobium meliloti*. *BMC Genomics* 2011;12:235.
39. Bottacini F, Medini D, Pavesi A, et al. Comparative genomics of the genus *Bifidobacterium*. *Microbiology (Reading)* 2010;156:3243–3254.
40. Kryazhimskiy S, Plotkin JB. The population genetics of dN/dS. *PLoS Genet* 2008;4:e1000304.
41. Harris SR, Feil EJ, Holden MT, et al. Evolution of MRSA during hospital transmission and intercontinental spread. *Science* 2010;327:469–474.
42. Argemi X, Matelska D, Ginalska K, et al. Comparative genomic analysis of *Staphylococcus lugdunensis* shows a closed pangenome and multiple barriers to horizontal gene transfer. *BMC Genomics* 2018;19:621.
43. Holt KE, Parkhill J, Mazzoni CJ, et al. High-throughput sequencing provides insights into genome variation and evolution in *Salmonella* Typhi. *Nat Genet* 2008;40:987–993.
44. Cui Y, Yu C, Yan Y, et al. Historical variations in mutation rate in an epidemic pathogen, *Yersinia pestis*. *Proc Natl Acad Sci U S A* 2013;110:577–582.
45. Sztukowska M, Bugno M, Potempa J, Travis J, Kurtz DM Jr. Role of rubrerythrin in the oxidative stress response of *Porphyromonas gingivalis*. *Mol Microbiol* 2002;44:479–488.
46. Lamont RJ, Jenkinson HF. Subgingival colonization by *Porphyromonas gingivalis*. *Oral Microbiol Immunol* 2000;15:341–349.
47. Chiang CY, Kyritsis G, Graves DT, Amar S. Interleukin-1 and tumor necrosis factor activities partially account for alveolar bone resorption induced by local injection of lipopolysaccharide. *Infect Immun* 1999;67:4231–4236.
48. Nishida E, Hara Y, Kaneko T, Ikeda Y, Ukai T, Kato I. Bone resorption and local interleukin-1 $\alpha$  and interleukin-1 $\beta$  synthesis induced by *Actinobacillus actinomycetemcomitans* and *Porphyromonas gingivalis* lipopolysaccharide. *J Periodontol Res* 2001;36:1–8.
49. Griffith F. The significance of pneumococcal types. *J Hyg (Lond)* 1928;27:113–159.
50. Sundqvist G, Figdor D, Hänström L, Sörlin S, Sandström G. Phagocytosis and virulence of different strains of *Porphyromonas gingivalis*. *Scand J Dent Res* 1991;99:117–129.
51. de Diego I, Veillard F, Sztukowska MN, et al. Structure and mechanism of cysteine peptidase gingipain K (Kgp), a major virulence factor of *Porphyromonas gingivalis* in periodontitis. *J Biol Chem* 2014;289:32291–32302.
52. Bao K, Belibasakis GN, Thurnheer T, Aduse-Opoku J, Curtis MA, Bostanci N. Role of *Porphyromonas gingivalis* gingipains in multi-species biofilm formation. *BMC Microbiol* 2014;14:258.

53. Guo Y, Nguyen KA, Potempa J. Dichotomy of gingipains action as virulence factors: From cleaving substrates with the precision of a surgeon's knife to a meat chopper-like brutal degradation of proteins. *Periodontol* 2000 2010;54:15–44.
54. Kress W, Maglica Z, Weber-Ban E. Clp chaperone-proteases: Structure and function. *Res Microbiol* 2009;160:618–628.
55. Capestany CA, Tribble GD, Maeda K, Demuth DR, Lamont RJ. Role of the Clp system in stress tolerance, biofilm formation, and intracellular invasion in *Porphyromonas gingivalis*. *J Bacteriol* 2008;190:1436–1446.



# Application Value of 64-slice Multidetector Spiral CT Contrast-enhanced Scan in Maxillofacial Soft Tissue Hypervascular Tumours

Wen Xin ZHANG<sup>1</sup>, Seyiti PAKEZHATI<sup>1</sup>, Shu LIU<sup>1</sup>, Xiao Feng HUANG<sup>2</sup>, Guo Wen SUN<sup>3</sup>, Tie Mei WANG<sup>1</sup>

**Objective:** To evaluate the diagnostic ability and clinical imaging features in maxillofacial soft tissue hypervascular tumours by 64-slice multidetector spiral computed tomography (64-MDCT) contrast-enhanced scanning.

**Methods:** In a retrospective study of 21 cases of hypervascular tumours, the degree of blood supply and indexes were assessed, and the pathological results were used as the diagnostic gold standard to evaluate the sensitivity and specificity of 64-MDCT plain scan and enhanced CT in the diagnosis of oral and maxillofacial soft tissue hypervascular tumours, using the receiver operating characteristic curve to analyse and evaluate the efficacy.

**Results:** Among 21 patients, the diagnostic accuracy of 64-MDCT contrast-enhanced scan was 90.48%, the area under the curve of venous phase CT value was 0.80, the sensitivity was 83.30% and the specificity was 72.73%.

**Conclusion:** 64-MDCT contrast-enhanced scan can be used to evaluate the blood supply of maxillofacial soft tissue hypervascular tumours before an operation. The CT value in the venous phase of tumours has the highest diagnostic effectiveness, which can reduce the risk of blood loss during surgery for maxillofacial hypervascular tumours. In addition, it has certain guiding significance for the formulation of clinical treatment plans.

**Key words:** contrast-enhanced computed tomography, hypervascular tumours, oral and maxillofacial, radiology, squamous cell carcinoma

*Chin J Dent Res* 2023;26(2):105–111; doi: 10.3290/j.cjdr.b4128033

More than 650,000 cases of maxillofacial and neck tumours are diagnosed worldwide every year, with a higher rate in Asia<sup>1</sup>. Maxillofacial soft tissue hypervascular tumours are tumors with special physiological characteristics affecting the head and neck, which increases the risk and difficulty of operation due to the complex anatomical structure and abundant blood supply, and they also involve multiple anatomical areas

including the oral cavity, pharynx, larynx, paranasal sinuses, nasal cavity and salivary glands.

Previous studies have focused mainly on benign hypervascular tumours such as hemangioma and vascular malformation<sup>2,3</sup>, but few have studied other soft tissue hypervascular tumours in the maxillofacial region. The physiological characteristics of malignant tumours such as oral squamous cell carcinoma (OSCC) and other benign tumours can match those of hypervascular tumours<sup>4</sup>.

It is particularly important to evaluate the blood supply of a tumour accurately before an operation, choose the appropriate surgical path and reduce the chances of injury in patients. In addition, implementation of multidimensional visualisation of tumours can objectively and truly show the relationship between tumours, blood vessels, jaws, the degree of blood supply of the tumour and the normal anatomy and pathological changes of blood supplying arteries and surrounding blood vessels, providing more accurate auxiliary diag-

1 Department of Dentomaxillofacial Radiology, Nanjing Stomatological Hospital, Medical School of Nanjing University, Nanjing, P.R. China.

2 Department of Oral Pathology, Nanjing Stomatological Hospital, Medical School of Nanjing University, Nanjing, P.R. China.

3 Department of Oral and Maxillofacial Surgery, Nanjing Stomatological Hospital, Medical School of Nanjing University, Nanjing, P.R. China.

**Corresponding author:** Dr Tie Mei WANG, Department of Dentomaxillofacial Radiology, Nanjing Stomatological Hospital, Medical School of Nanjing University, Zhong Yang Road 30, Nanjing 210008, P.R. China. Tel: 86-25-83620351; Fax: 86-25-83620200. Email: tiemeiwang106@163.com

nosis and treatment plans for stomatologists, which is also a pressing clinical issue to solve and address.

Studies have shown that computed tomography (CT) image features correlate with the histopathological grade, molecular biomarkers and prognosis for various tumours, such as oropharyngeal, oesophageal and breast cancer<sup>5</sup>. Using contrast-enhanced imaging, Yu et al<sup>6</sup> distinguished between human papillomavirus positive and negative oropharyngeal cancers.

In the present study, we analysed CT-based radiological features of maxillofacial soft tissue hypervascular tumours based on the ability of these features to predict important clinical and histological factors across different tumour types.

## Materials and methods

### Case selection

This retrospective study was conducted in accordance with the Declaration of Helsinki (as revised in 2013) and approved by the institutional review board of Nanjing University Medical College Affiliated Stomatology Hospital (NJSH-2022NL-011). The case records were identified in our institution from June 2017 to October 2021. A total of 21 patients with a diagnosis of maxillofacial soft tissue hypervascular tumours (15 men and 6 women; mean age  $47.57 \pm 16.45$  years) were enrolled in this study. The inclusion criteria were as follows:

- patients with plain CT scan and multidetector spiral CT (64-MDCT) enhanced examination prior to surgery;
- arterial phase net enhancement value exceeding flat scan CT value  $\geq 40$  Hu after enhancement of the CT scan, which could be diagnosed using imaging.

The exclusion criteria were as follows:

- patients with hyperthyroidism, asthma, liver, kidney or severe cardiopulmonary insufficiency, or who are not well and may be in danger during the image-taking process;
- patients with iodine contrast agent allergy, history of drug allergy and allergic constitution;
- female patients who were planning pregnancy within 6 months or who were pregnant or lactating;
- patients who were unable to cooperate;
- images including metal ornaments and foreign objects, as well as obvious motion artefacts.

### Criteria for judging enhancement

If the lesion had vascular imaging or the difference between CT images before and after enhancement exceeded 40 Hu, it was defined as “enhanced”; if it did not have a vascular shadow or the difference between CT images before and after enhancement was between 20~40 Hu, it was defined as “possible enhancement”; and if no vascular shadow was seen or the difference between CT images before and after enhancement was less than 20 Hu, it was considered “no enhancement”<sup>7</sup>.

### CT image acquisition

CT examinations were performed on a 64-slice CT scanner (SOMATOM Perspective Sensation 64, Siemens Healthineers, Erlangen, Germany). A CT scan of the head and neck was performed, followed by contrast-enhanced 64-MDCT examination. The scanning range was from the aortic arches to the cranial top. Scan parameters were set at 110 kV, and the pipe current was automatically adjusted by the CT machine based on the CARE Dose4D (Siemens) intelligent algorithm,  $64 \times 0.625$  mm detector collimation, gantry rotation time of 0.48 seconds and slice thickness of 1 mm. CT scans of the head and neck were performed using intravenous nonionic iodinated contrast (350 mg/ml, Iohexol). The dosage of contrast agent was calculated according to patients' weight as 1.5 to 2.0 ml/kg to inject at 3.5 ml/second. The follow-up scan was delayed by 10 seconds after the start of contrast injection. The tracking scan interval was 1 seconds. When the CT value of the aortic arch area reached 95 Hu, the arterial period scan was begun.

### Image analysis

#### CT feature evaluation

Two radiologists with 8 and 12 years of experience and who were blinded to the pathological diagnosis performed CT analysis independently. The following CT features were evaluated qualitatively:

- lesion size (expressed as the largest dimension);
- tumour margin (clear or unclear);
- area of the tumour;
- necrosis (absent or present);
- texture (uniform or non-uniform);
- CT value and CT enhancement value of each phase (the diameter of the region of interest [ROI] set at 1 cm.

**Table 1** Clinical data and CT signs of benign and malignant tumors with a rich blood supply in the oral and maxillofacial region.

| Clinical factors and image feature |                                      | Malignant [cases (%)]  | Benign [cases (%)]    | P value |
|------------------------------------|--------------------------------------|------------------------|-----------------------|---------|
| Sex (M/F)                          |                                      | 10/2                   | 5/4                   | 0.16    |
| Age (y)                            |                                      | 50.67 ± 13.11 (33 ~67) | 43.44 ± 20.17 (17~68) | 0.03    |
| Location                           | Oropharynx                           | 4 (33.3)               | 2 (22.2)              | 0.46    |
|                                    | Tongue                               | 2 (16.7)               | NA (NA)               |         |
|                                    | Neck                                 | 1 (8.3)                | NA (NA)               |         |
|                                    | Parotid                              | 2 (16.7)               | 3 (33.3)              |         |
|                                    | Buccal                               | 3 (25.0)               | 4 (44.4)              |         |
| Margin (clear or unclear)          |                                      | 8/4                    | 8/1                   | 0.16    |
| Necrosis (absent or present)       |                                      | 4/8                    | 2/7                   | 0.58    |
| Texture (uniform or non-uniform)   |                                      | 4/8                    | 3/6                   | 1.00    |
| CT value (Hu)                      | Plain CT                             | 49.08 ± 8.77           | 46.85 ± 7.10          | 0.84    |
|                                    | Arterial phases                      | 104.71 ± 27.37         | 152.09 ± 63.63        | 0.01    |
|                                    | Venous phases                        | 103.92 ± 16.09         | 143.32 ± 67.04        | 0.03    |
|                                    | Arterial phase net enhancement value | 55.63 ± 28.24          | 105.00 ± 65.03        | 0.01    |
|                                    | Venous phase net enhancement value   | 54.84 ± 16.52          | 96.37 ± 66.62         | 0.01    |

F, female; M, male; NA, not applicable.

**Table 2** Comparison of plain scan and contrast-enhanced 64-MDCT in the area of maxillofacial soft tissue hypervascular tumours.

| Group                     | Area (mm <sup>2</sup> ) | P value |
|---------------------------|-------------------------|---------|
| Plain CT scan             | 10.84 ± 7.13            | 0.00    |
| Contrast-enhanced 64-MDCT | 12.13 ± 7.03            |         |

The most obvious tumour enhancement area was selected to avoid the volume effect and artefact area, and the mean value was measured.

### Enhanced performance

Based on the combination of contrast enhancement observed at each stage of the study, a global dynamic pattern of enhancement was defined. Stable contrast enhancement referred to stable and persistent enhancement in which all or part of the lesions in the arterial phase are higher than the surrounding soft tissue, and progressive contrast enhancement was where the lesion increases progressively over time, reaching maximal intensity in venous phases; these classifications were adopted from Iavarone et al<sup>8</sup>.

### Statistical analysis

Statistical analysis was performed using SPSS (IBM, Armonk, NY, USA). Chi-square or Fisher exact tests and independent sample *t* tests were used for qualitative and quantitative data, respectively. Associated receiver operating characteristic (ROC) curves were plotted using SPSS. Intragroup correlation coefficient (ICC) was used to evaluate the consistency of CT values measured

by two doctors. *P* < 0.05 was considered statistically significant.

### Results

The CT data measured by two radiologists were demonstrated to have a good agreement, with ICCs of 0.92. The characteristics of the patients are described in Table 1. There were significant differences in patient age between the two groups (*P* < 0.05). Patients with malignant hypervascular tumours were older than their counterparts with benign tumours. The lesion area showed significant differences between the group with plain CT scans and contrast-enhanced CT scans (*P* < 0.00), showing that the tumour boundary after enhancement is larger than that for the plain CT scan image. Comparisons of the two groups are presented in Table 2.

Contrast-enhanced CT provided the best accuracy in detecting benign and malignant maxillofacial soft tissue hypervascular tumours (90.48%), and it was superior to plain scans (14.29%). The exact values are shown in Table 3.

With a threshold of 0.73, the sensitivity of the venous phase CT value and the venous phase net enhancement value was 83.30% and 100.00%, respectively, and the specificity was 72.73%. The area under the curve (AUC)

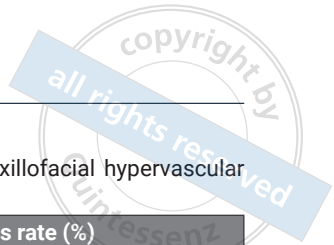


**Table 3** Comparison of the diagnostic accuracy of plain scan and contrast-enhanced 64-MDCT in maxillofacial hypervascular tumours.

| Group                     | Diagnosis result |    | Diagnosis rate (%) |
|---------------------------|------------------|----|--------------------|
|                           | +                | -  |                    |
| Plain CT scan             | 3                | 18 | 14.29              |
| Contrast-enhanced 64-MDCT | 19               | 2  | 90.48              |
| $\chi^2$                  | 24.44            |    |                    |
| P value                   | 0.00             |    |                    |

**Table 4** ROC curve results of different CT value indexes to evaluate the degree of blood supply of maxillofacial soft tissue hypervascular tumours.

| Variable                             | AUC  | P value | SE   | 95% CI    | Sensitivity (%) | Specificity (%) | Youden index |
|--------------------------------------|------|---------|------|-----------|-----------------|-----------------|--------------|
| Arterial phase                       | 0.74 | 0.06    | 0.12 | 0.51–0.90 | 95.20           | 54.55           | 0.55         |
| Arterial phase net enhancement value | 0.73 | 0.07    | 0.12 | 0.50–0.89 | 100.00          | 54.55           | 0.55         |
| Venous phase                         | 0.80 | 0.01    | 0.12 | 0.59–0.94 | 83.30           | 72.73           | 0.73         |
| Venous phase net enhancement value   | 0.76 | 0.05    | 0.13 | 0.54–0.91 | 100.00          | 72.73           | 0.73         |

CI, confidence interval; SE, standard error.

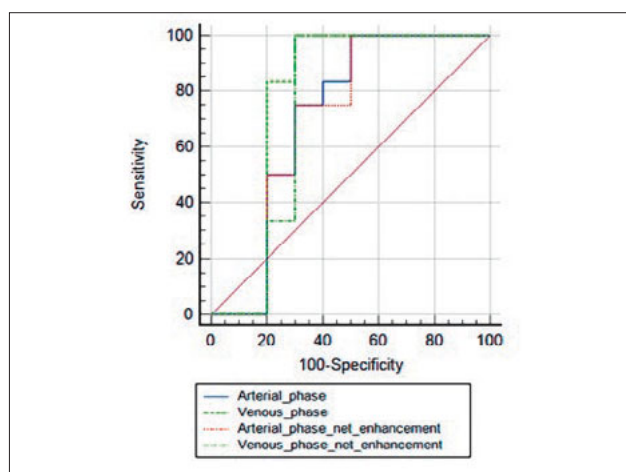


**Fig 1** The ROC curve of contrast-enhanced 64-MDCT to evaluate the blood supply to a maxillofacial soft tissue hypervascular tumour.

for ROC analysis was 0.80 and 0.76. Sensitivity and specificity are presented in Table 4 and Fig 1.

**Discussion**

*Hypervascular tumours*

A soft tissue hypervascular tumour is a type of tumour or tumour-like lesion with a net enhancement degree of arterial and venous phase equal to or greater than that of a plain CT scan, as well as increased intensity after enhanced CT<sup>9</sup>. Blood-rich tumours of the head and neck include hemangioendothelioma, neurogenic tumours

(e.g., schwannoma), paragangliomas (e.g., carotid body tumours), nasopharyngeal angiofibromas, hemangiomas and other malignant tumours<sup>10</sup>. The present study involved nine cases of soft tissue benign tumours, including spindle cell tumor (one case), basal cell adenoma (one case), adenolymphoma (one case) and inflammatory mass (one case). There were five cases of vasogenic tumours, including vascular malformation (four cases) and carotid body tumour (one case). Twelve cases of malignant blood-rich tumours included squamous cell carcinoma (nine cases), mucoepidermoid carcinoma (one case), acinar cell carcinoma (one case) and malignant lymphadenoma (one case). In the diagnosis of hypervascular diseases such as affecting the liver and kidney, enhanced 64-MDCT plays an important role in the preoperative examination, showing uniform or inhomogeneous and marginal enhancement in each stage of enhancement and showing “cow’s eye” and “pupil” sign (the centre of the lesion is low density, the edge is high density due to enhancement, and the density of the outermost layer of the lesion is lower than that of normal tissue) when the lesion is necrotic<sup>11</sup>.

With regard to tumours with a rich blood supply in the maxillofacial soft tissue, on the plain CT scan, most soft tissue masses had a uniform density and unclear boundary and showed round, quasi-round or irregular soft tissue mass after enhancement. In this study, most of the benign tumours were vascular lesions (5 seconds, 9%). The boundary was clear after enhancement and the lesions were significantly enhanced in uniform mass and patch shape. The interior and edges were characterised by clusters of enhanced blood ves-



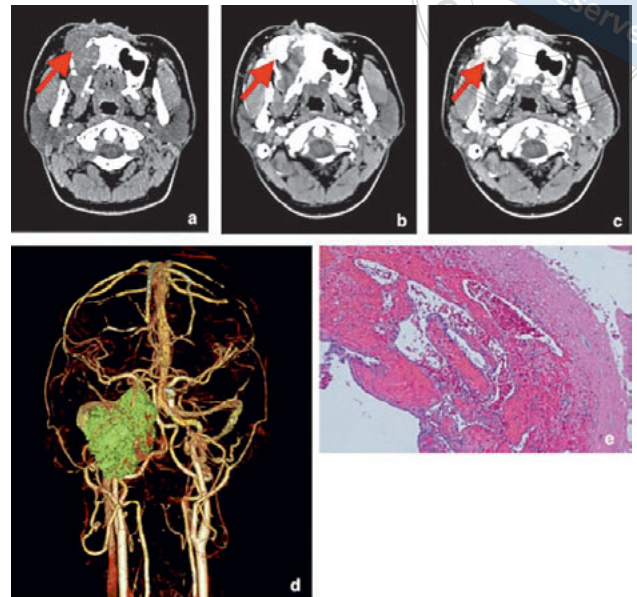


**Fig 2** A 24-year-old man with vascular malformation of the right maxilla. (a) The plain scan image shows the soft tissue mass in the right maxilla, the CT value is around 56 Hu, and the boundary is not clear. (b) The CT value of the arterial phase is 178 Hu. (c) The CT value of the venous phase is 236 Hu, showing rosette-shaped and patch-like enhancement. (d) Volume rendering technique reconstruction images show that the boundary of the mass is adjacent to the internal carotid artery and there are branches of the external carotid artery passing through it. (e) Inflammatory fibrous connective tissue and bone tissue, with vascular hyperplasia and a large number of cellulose hemorrhagic exudation. (hematoxylin-eosin, original magnification  $\times 100$ ).

sels and vascular penetration of varying thickness. On the other hand, benign tumours of the parotid gland, such as basal cell adenoma, show severe enhancement in the venous phase, which is generally weakened further in the delayed phase, and cystic changes are easy to observe. This may be related to the vascular structure of the tumour; the cystic area contains many endothelial-lined vascular channels, as well as capillaries and venules<sup>12</sup>. The enhancement of inflammatory components in this group of tumours shows solid tissue with an irregular shape. Pathology suggests that chronic inflammation with necrosis may be caused by infection, and a large amount of neovascularisation is formed during the repair process of inflammation and necrosis<sup>13</sup>. The majority of malignant or metastatic tumours showed inhomogeneous rosette-like and patchy severe enhancement, which was further enhanced in the venous phase; additionally, these tumours were different to malignant hypervascular tumours of the liver, which often show “fast-in and fast-exit” patterns. The solid components of malignant hypervascular tumours in the maxillofacial region were significantly enhanced and mixed with uneven enhancement areas, which represented the vascular nutrient area, tumour cell aggregation area and necrotic area within the tumour. In addition, delayed enhancement is related to the content and composition of collagen fibres in the tumour<sup>14</sup>.

According to the results of the ROC curve analysis, enhanced 64-MDCT is a more effective and sensitive method for screening and predicting hypervascular tumours in the maxillofacial region because it gives the

largest AUC of venous phase CT scans, which is useful in determining the degree and characteristics of the tumour’s blood supply. The present results indicate that when the enhanced CT value of the tumour is  $\geq 80$  Hu, it can be considered to have a rich blood supply. The results also suggest that when the tumour displays progressive enhancement and the venous phase CT value reaches 112~131 Hu, it can be regarded as a malignant hypervascular tumour.

In this study, the diagnostic accuracy of enhanced 64-MDCT is much higher than that of a plain scan with enhanced CT, indicating that contrast-enhanced CT can dynamically distinguish between blood vessels and lymph nodes, clearly display the location, size, boundary, blood supply and surrounding tissue infiltration of the mass, and provide more vascular anatomical information and a stereoscopic view combined with image post-processing<sup>15</sup>.

The present authors found that the size of the lesion measured by the plain scan of a maxillofacial soft tissue tumour with a rich blood supply was smaller than its numerical boundary measured after enhancement and that this was likely due to marginal infiltration of the tumour, which included increased neovascularisation and blood flow at the margins. The surface permeability is high, which increases expression in the marginal tissue of the tumour<sup>16</sup>. The case is shown in Figs 2 and 3.

### Treatment

Surgery and/or intervention forms the basis for the treatment of soft tissue hypervascular tumours<sup>17</sup>, and

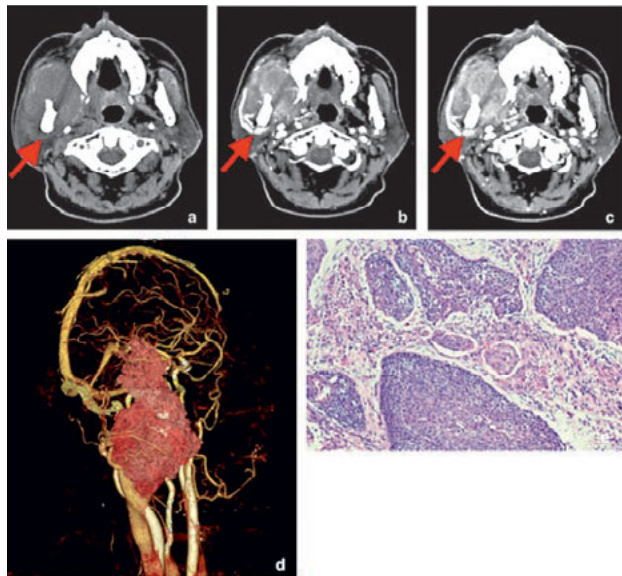


**Fig 3** A 67-year-old man with squamous cell carcinoma of the maxillary right posterior area. **(a)** The plain scan image shows the soft tissue mass in the maxillary right posterior area. The CT value is around 42 Hu. **(b)** The CT value of the arterial phase is 97 Hu. **(c)** The CT value of the venous phase is 114 Hu and the boundary is clear, showing target-like enhancement. **(d)** Volume rendering technique reconstruction images show that the mass is adjacent to the external carotid artery. **(e)** There was obvious epithelial nest mass infiltration with necrosis in the maxillary right posterior area (hematoxylin-eosin, original magnification  $\times 100$ ).

requires accurate information about the location, size and extent of the lesions, as well as blood supply and drainage vessels. Thus, the analysis and prediction of preoperative noninvasive imaging examination are very important for treatment planning. Enhanced 64-MDCT can predict the degree of the tumour blood supply in relation to the rich blood supply to the soft tissue, as well as the relationship between the tumour, blood vessel and maxillofacial bone<sup>18</sup>, which is used by clinicians to design operating plans and assess operational risks. The radiation dose and iodine contrast agent used in enhanced 64-MDCT are lower than in catheter angiography. Additionally, it has the advantages of no anaesthesia intubation, no obvious trauma<sup>19</sup> and higher sensitivity and visibility than ultrasound and other noninvasive imaging<sup>20</sup>.

#### *Application value*

64-MDCT contrast-enhanced technology also has high application value for tumours adjacent to or invading the internal carotid artery. Contrast-enhanced CT can show the relationship between tumours and carotid artery through 64-MDCT contrast-enhanced technology, clarify the situation of wrapping, passing, erosion and the intracranial circle of Willis, and provide a basis for surgical plan design. If the internal carotid artery is only moved but not eroded, the internal carotid artery can be preserved. If the internal carotid artery is extensively eroded, the preoperative plan should be designed carefully to make preparations and plans in advance for the sacrifice of the internal carotid artery, which can avoid the serious con-

sequences of intracranial ischemia caused by temporary ligation or sacrifice of the internal carotid artery during the operation. Some cervical hemangiomas located in the skull base, penetrating through the skull or rich in blood supply, including carotid body tumours, nasopharyngeal hemangioma and mild hemangiopericytoma, are difficult to operate, which can be done with 64-MDCT contrast-enhanced scans aided by preoperative embolisation therapy to reduce intraoperative bleeding and increase the success rate of surgery for patients. For large-scale aneurysmal bone cysts, cementum-ossifying fibroma, malignant tumours of the inferior temporal fossa and metastatic tumours, preoperative 64-MDCT contrast-enhanced scan evaluation can also be performed. If the risk of intraoperative bleeding is high and the lesion cannot be completely resected, preoperative embolisation can be performed.

#### **Conclusion**

In this study, 64-slice spiral CT plain scan and contrast-enhanced CT were used to evaluate the blood supply of oral and maxillofacial soft tissue tumours. The results showed high sensitivity and good repeatability of the noninvasive imaging evaluation. The present study provides the theoretical basis and a certain clinical significance and reference value for preventing tumour recurrences. In addition, we also used 3D reconstruction technology to more intuitively and clearly show the relationship between tumour and surrounding blood vessels, bone and other anatomical structures to provide guidance for clinical analysis.

## Conflicts of interest

The authors declare no conflicts of interest related to this study.

## Author contribution

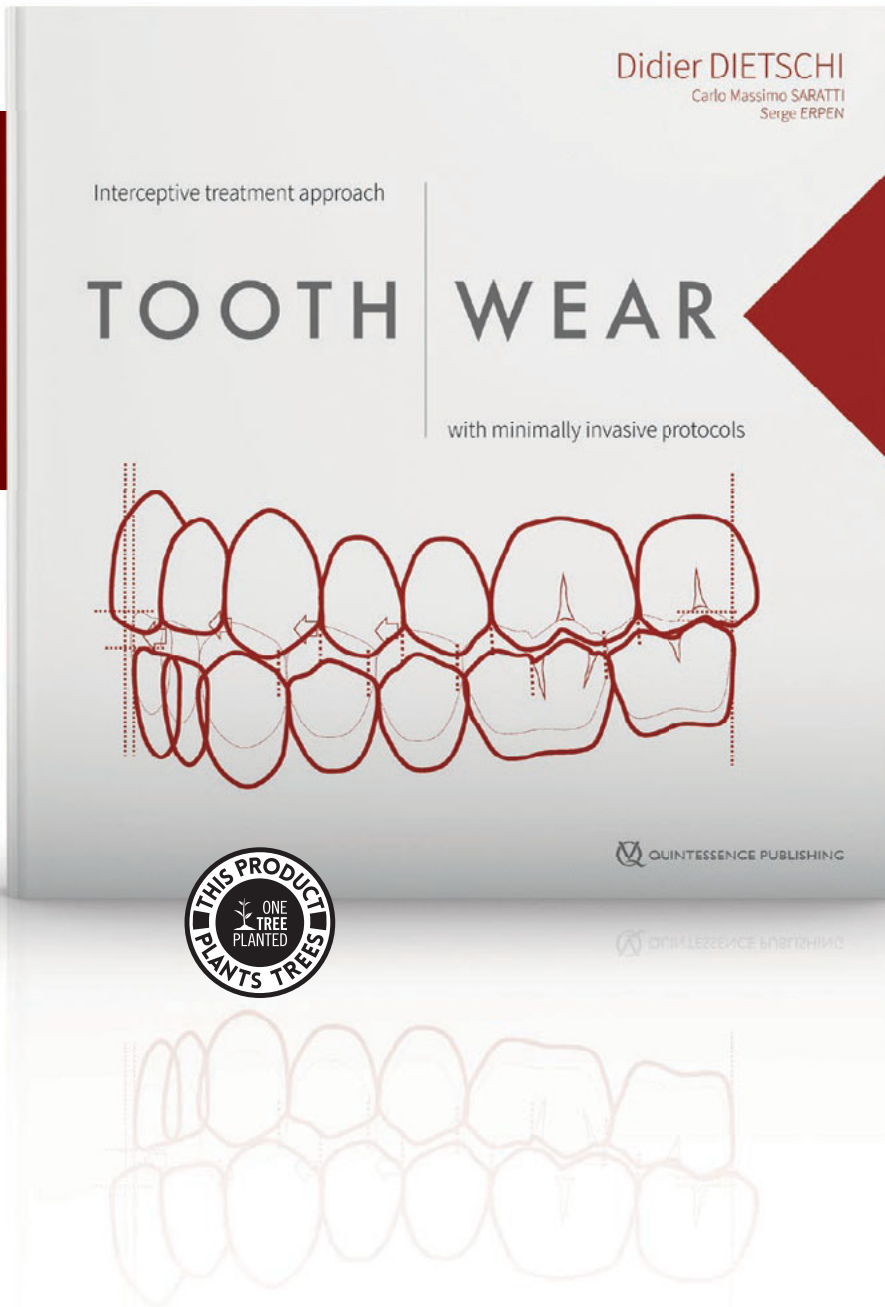
Drs Wen Xin ZHANG, Seyiti PAKEZHATI and Shu LIU collected data and draft the manuscript; Drs Xiao Feng HUANG and Guo Wen SUN provided clinical data and pictures; Dr Tie Mei WANG proposed revisions during the review of this paper. All authors agreed with the final version of the manuscript.

(Received Oct 31, 2022; accepted Feb 20, 2023)

## References

- Shang C, Feng L, Gu Y, Hong H, Hong L, Hou J. Impact of multi-disciplinary team management on the survival rate of head and neck cancer patients: A cohort study meta-analysis. *Front Oncol* 2021;11:630906.
- Choi JH, Ro JY. The 2020 WHO classification of tumors of bone: An updated review. *Adv Anat Pathol* 2021;28:119–138.
- Gong QX, Fan QH. Updates of the 2020 WHO classification of soft tissue tumors: part II [in Chinese]. *Zhonghua Bing Li Xue Za Zhi* 2021;50:314–318.
- Agarwal D, Pardhe N, Bajpai M, et al. Characterization, localization and patterning of lymphatics and blood vessels in oral squamous cell carcinoma: A comparative study using D2-40 and CD-34 IHC marker. *J Clin Diagn Res* 2014;8:ZC86–ZC89.
- Zhang MH, Hasse A, Carroll T, Pearson AT, Cipriani NA, Ginat DT. Differentiating low and high grade mucoepidermoid carcinoma of the salivary glands using CT radiomics. *Gland Surg* 2021;10:1646–1654.
- Yu K, Zhang Y, Yu Y, et al. Radiomic analysis in prediction of human papilloma virus status. *Clin Transl Radiat Oncol* 2017;7:49–54.
- Hartman DS, Choyke PL, Hartman MS. From the RSNA refresher courses: A practical approach to the cystic renal mass. *RadioGraphics* 2004; 24(suppl 1):S101–S115.
- Iavarone M, Piscaglia F, Vavassori S, et al. Contrast enhanced CT-scan to diagnose intrahepatic cholangiocarcinoma in patients with cirrhosis. *J Hepatol* 2013;58:1188–1193.
- Choi HH, Manning MA, Mehrotra AK, Wagner S, Jha RC. Primary hepatic neoplasms of vascular origin: Key imaging features and differential diagnoses with radiology-pathology correlation. *AJR Am J Roentgenol* 2017;209:W350–W359.
- Lutz J, Holtmannspötter M, Flatz W, et al. Preoperative embolization to improve the surgical management and outcome of juvenile nasopharyngeal angiofibroma (JNA) in a single center: 10-year experience. *Clin Neuroradiol* 2016;26:405–413.
- Wang G, Zhu S, Li X. Comparison of values of CT and MRI imaging in the diagnosis of hepatocellular carcinoma and analysis of prognostic factors. *Oncol Lett* 2019;17:1184–1188.
- Chen G, Wen X, Chen XJ, et al. Imaging features and pathological analysis of 43 parotid basal cell adenomas. *Comput Math Methods Med* 2021;2021:7906058.
- Wang H, Li QK, Auster M, Gong G. PET and CT features differentiating infectious/inflammatory from malignant mediastinal lymphadenopathy: A correlated study with endobronchial ultrasound-guided transbronchial needle aspiration. *Radiol Infect Dis* 2018;5:7–13.
- Papathanassiou ZG, Alberghini M, Picci P, et al. Solitary fibrous tumors of the soft tissues: Imaging features with histopathologic correlations. *Clin Sarcoma Res* 2013;3:1.
- Ren Y, Chen GZ, Liu Z, Cai Y, Lu GM, Li ZY. Reproducibility of image-based computational models of intracranial aneurysm: A comparison between 3D rotational angiography, CT angiography and MR angiography. *Biomed Eng Online* 2016;15:50.
- Wong C, Stylianopoulos T, Cui J, et al. Multistage nanoparticle delivery system for deep penetration into tumor tissue. *Proc Natl Acad Sci U S A* 2011;108:2426–2431.
- Su LX, Fan XD, Zheng JW, et al. A practical guide for diagnosis and treatment of arteriovenous malformations in the oral and maxillofacial region. *Chin J Dent Res* 2014;17:85–89.
- Corriere MA, Islam A, Craven TE, Conlee TD, Hurie JB, Edwards MS. Influence of computed tomography angiography reconstruction software on anatomic measurements and endograft component selection for endovascular abdominal aortic aneurysm repair. *J Vasc Surg* 2014;59:1224–1231.e1–e3.
- Zhao Y, Yang L, Wang Y, Zhang H, Cui T, Fu P. The diagnostic value of multi-detector CT angiography for catheter-related central venous stenosis in hemodialysis patients. *Phlebology* 2021;36:217–225.
- Swieton D, Kaszubowski M, Szyndler A, et al. Visualizing carotid bodies with Doppler ultrasound versus CT angiography: Preliminary study. *AJR Am J Roentgenol* 2017;209:1348–1352.

# EXPERT RECIPES FOR SUCCESS!



Didier Dietschi | Carlo Massimo Saratti | Serge Erpen

## Tooth Wear

Interceptive treatment approach with minimally invasive protocols

850 pages, 2,700 illus

ISBN 978-1-78698-115-8

€ 320

This publication is not a textbook but rather a comprehensive review of clinical procedures that can help the practitioner to select a proper protocol and suitable materials to more selectively treat the various forms of tooth wear. This "cookbook" is based on more than 20 years of experience in this ever-increasing pathology. The main focus is the prevention of tooth wear progression with the use of noninvasive and affordable procedures in the proper timeframe, bearing in mind that comprehending this pathology is a lifelong endeavor. If there was no opportunity to intervene early enough, you will also find the "recipes" needed for the proper use of indirect and CAD/CAM-produced restorations.



[www.quint.link/expert-recipes](http://www.quint.link/expert-recipes)



[books@quintessenz.de](mailto:books@quintessenz.de)



+49 (0)30 761 80 667

 QUINTESSENCE PUBLISHING

# Novel Digital Mouth Preparation Technique for Fabricating Implant-Retained Removable Partial Dentures with Distal Extension: a Case Report

Wan Rong WANG<sup>1#</sup>, Rui XIE<sup>1,#</sup>, Li Na NIU<sup>1</sup>, Zhi Hong FENG<sup>1</sup>, Yi Min ZHAO<sup>1</sup>

*Implant-retained removable partial dentures (RPDs) are commonly used to resolve the complications associated with traditional distal extension RPDs; however, this technology does not consider the necessity and importance of parallelism between the path of RPD insertion and the long axis of the implant. This clinical report presents a novel digital preparation technique that involves the preparation of parallel guiding planes on abutment teeth and implant insertion in the distal extension area using a computer-aided design and manufacturing template. This clinical case of implant-retained RPDs illustrates the fabrication and application of the digital template. Using this technique, the path of RPD insertion is parallel to the long axis of the implant. As a result, the components of the implant-retained RPD, including the abutment teeth, implants and attachments, can demonstrate greater longevity.*

**Key words:** *abutment teeth, digital preparation technique, distal extension, guide rods, guiding plane, implant, removable partial denture*

*Chin J Dent Res 2023;26(2):113-117; doi: 10.3290/j.cjdr.b4128029*

As the global population ages, the number of people with partial edentulism has increased<sup>1</sup>. Demand for removable partial dentures (RPDs) is high due to their low cost and wide range of indications<sup>2</sup>; however, the most common complaints related to distal extension RPDs are their lack of stability and retention, and other complications include irritation of the soft tissue under the connector or denture base<sup>3</sup>. Strategic placement of dental implants can minimise or eliminate all these difficulties<sup>4-7</sup>. Implant-retained RPDs provide favourable retention and stability for the denture base and

limit rotational movements. Many studies have reported patient satisfaction with implant-retained RPDs due to comfort, good retention, masticatory capacity, aesthetic appearance, ease of cleaning and significant improvements to speech<sup>8-10</sup>. In addition, a systematic review concluded that using an implant-retained removable dental prosthesis does not adversely affect the survival rate of the underlying implants<sup>11</sup>.

Nevertheless, flaws in the fabrication of implant-retained RPDs remain. Specifically, some scholars have not considered the necessity and importance of parallelism between the path of removable denture insertion and the long axis of the implant. The convergence or divergence of implant attachments and the path of removable denture insertion commonly accelerates the wear undergone by attachments. Moreover, RPDs cannot be placed passively, resulting in an excessive, unfavourable force on the natural abutment teeth. Although some scholars have noted this problem, no feasible solution has yet been developed<sup>12</sup>. With the application of computer technology in stomatology, insertion of implants using guides or navigation has become common; however, a comprehensive design for implant placement and preparation of the path of insertion of implant-retained RPDs has not yet been reported.

1 National Clinical Research Center for Oral Diseases, State Key Laboratory of Military Stomatology, Shaanxi Key Laboratory of Stomatology, Department of Prosthodontics, School of Stomatology, The Fourth Military Medical University, Xi'an, Shaanxi Province, P.R. China.

# These two authors contributed equally to this work.

**Corresponding authors:** Dr Zhi Hong FENG and Prof Yi Min ZHAO, Department of Prosthodontics, School of Stomatology, The Fourth Military Medical University, No.145, Changle West Road, Xi'an 710032, Shaanxi Province, P.R. China. Tel: 86-029-84776465; Fax: 86-029-84776465. Email: fengzhihong0516@163.com; zhaoyim@fmmu.edu.cn

This work was supported by the Innovation Capability Support Program of Shaanxi (2023-CX-PT-27) and New Technology and New Project Research Grant from the Third Affiliated Hospital of Air Force Medical University.



**Fig 1** The anterior reverse articulation is clearly visible on the maxillary and mandibular study casts on the articulator.



**Fig 2** Temporary radio-opaque dentures were used as a radiographic guide.

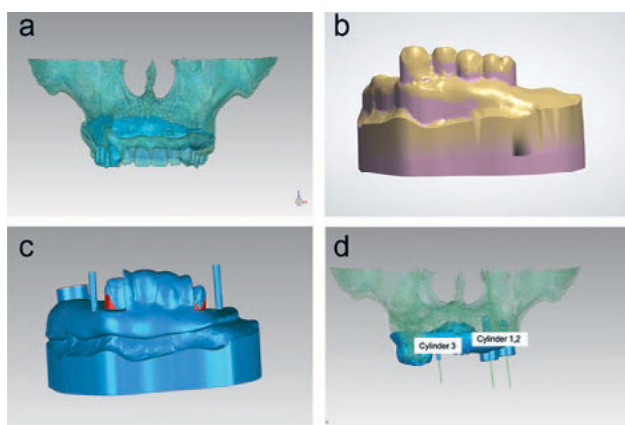


**Fig 3** Computer-aided design of the combined guide plate: (a) The master 3D model; (b) the direction of the path of insertion was defined; (c) a base plate with guide rod; (d) the axis of the implants (cylinders 1 and 2) was as parallel to the path of insertion of the RPD (cylinder 3) as possible.



**Fig 4** Resin guide plate with guide rods and guide rings.

To solve these issues, the present authors explored a novel digital technique: computer technology was used for model survey and analysis, and the path of removable denture insertion was determined. Subsequently, the orientation of the implant was designed based on the path of removable denture insertion, and a combined guide plate was designed and fabricated through CAD/CAM to ensure that the virtual design could be implemented intraorally.

**Case report**

All procedures were performed in accordance with the ethical standards of the Committee on Human Experimentation of The Air Force Medical University, Xi'an, China, and the use of the patient's pictures was approved by the ethics committee. The patient also voluntarily provided written informed consent.

A healthy 56-year-old man requested an RPD for partial edentulism in the maxilla. Intraoral examination revealed the absence of maxillary anterior teeth, left posterior teeth and the right second molar. An obvious anterior reverse articulation and lack of support for the upper lip precluded the fabrication of implant fixed partial dentures. After a comprehensive review of the patient's oral condition and communication with him and his family, the patient decided to proceed with an implant-retained RPD with a distal extension.

Maxillary and mandibular study casts were obtained, and the maxillomandibular relationship was recorded and transferred to the articulator. The anterior reverse articulation was observed more clearly on the cast, and the need for an implant-retained RPD instead of an implant fixed partial denture was confirmed (Fig 1). The study casts were scanned using Ceramill Map 600 (Aman Girschbach, Pforzheim, Germany) to obtain a 3D

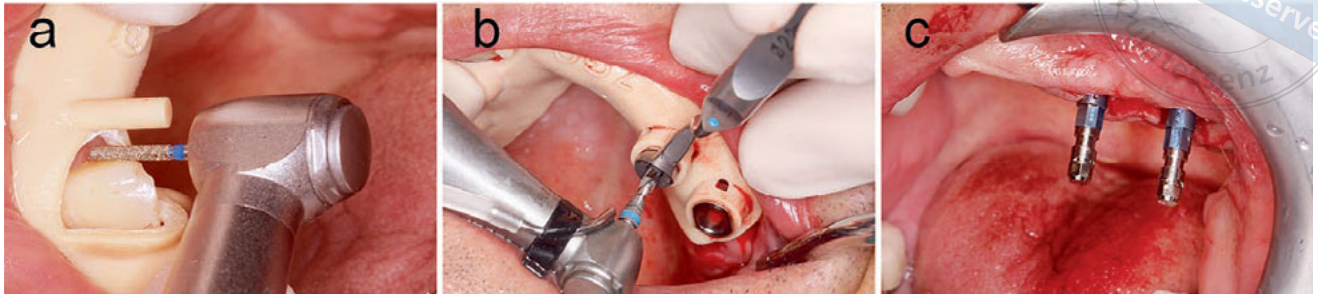


**Fig 5** Surgery with the combined guide plate: (a) the guiding plane was prepared according to the guide rods; (b) implant insertion surgery under the guidance of the combined guide plate; (c) visually, the two implants are completely parallel.

model of the dentures, which was saved as a standard tessellation language (STL) file.

Temporary radio-opaque dentures were fabricated on the study models and used as a radiographic guide (Fig 2). Dual CBCT was performed. Based on the CBCT data, 3D models of the maxilla and mandible, remaining dentition and artificial dentition were reconstructed and matched with the 3D models obtained by scanning the study models to set up the master 3D models in MIMICS 20.0 (Materialize, Leuven, Belgium). The model data were also saved as STL files (Fig 3a).

The 3D master models were transferred to the 3Shape Dental System 2020 software (3Shape, Copenhagen, Denmark) to survey the 3D model of the maxillary study cast to define the most advantageous position and path of insertion for an RPD. The undercuts were placed on the cast model (Fig 3b). A suprabulge circumferential retainer was designed on the maxillary first molar, and the infrabulge clasp on the maxillary right canine only played a stabilising role.

Thereafter, the 3D model of the maxillary study cast with the most advantageous position was input into MIMICS 20.0, and a model of the remaining teeth and support base plate was generated. Subsequently, guide rods with a diameter of 1.5 mm, completely parallel to the path of insertion of the final RPD, were designed on the base plate. The guide rods were placed 5 to 8 mm from the abutment teeth, and their height was the same as that of the abutment teeth. If the guide rods were too close or too high in relation to the abutment teeth, they would have hindered the accessibility of the handpiece during the preparation of the abutment teeth (Fig 3c).

Data related to the base plate were imported into Simplant 18.0 (Materialize). Based on the condition of the maxillary alveolar bone and the defined path of insertion of the RPD, the position, size and axial direction of the implants were determined. Accordingly, guide ring holes were designed in the same base plate, which served as the final guide plate, and the data

were saved as STL files. The long axis of the implant was completely parallel to the guide rods and path of insertion of the RPD. The key was to adjust the axial orientation of the implants to be as parallel to the path of insertion of the RPD as possible (Fig 3d).

Data of the final 3D template were transmitted to a 3D printer (Form 2; Formlabs, Sommerville, MA, USA) to fabricate the physical resin guide plate (Fig 4). The guide rings were positioned in the corresponding holes. The CAD/CAM resin guide plate was positioned and retained in the remaining maxillary teeth. The guiding planes on the abutment teeth of the RPD were prepared as indicated by the guide rods. The dental burs were completely parallel to the guide rods during preparation (Fig 5a). The other guiding planes were prepared in the same manner. Thus, all guiding planes were parallel to each other and the pre-designed guide rods.

Subsequently, at the same appointment, standard disinfection protocols were followed. The resin guide plate was dipped in 5% o-phthalaldehyde for 10 minutes and rinsed thoroughly with saline before being placed in the patient's mouth. Under the guidance of the resin guide plate, two implants were placed in the maxillary alveolar bone (Straumann BL 4.1 [Ø 10 mm] and Straumann BL 4.8 [Ø 8 mm]; Straumann, Basel, Switzerland) under local infiltration anaesthesia with primacaine, and cover screws were attached to the implants (Fig 5b).

At the time of surgery, the two implants were visually parallel (Fig 5c). After surgery, CBCT was performed and the 3D model was reconstructed. The parallelism between the long axis of the two implants and guide rods and the long axis of the pre-designed implant was confirmed (Fig 6). The results were in agreement with the expected design.

After 6 months, implant osseointegration was complete and the locator attachments were torqued in the implants at the pre-planned positions. The final RPD was fabricated and inserted intraorally (Fig 7).

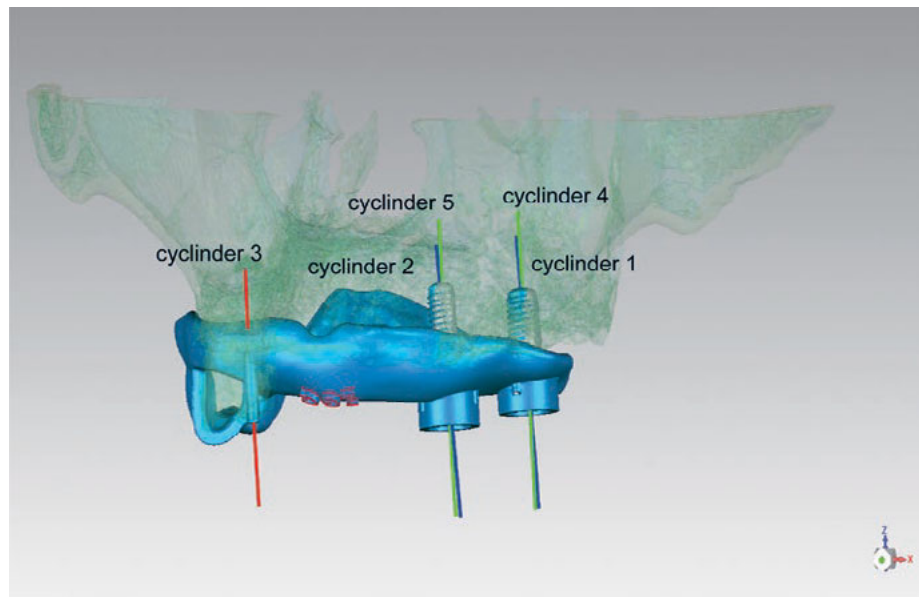


**Fig 6** Postoperative implants (grey) and pre-planned implants (blue); the blue axes of the two pre-planned implants (cylinders 1 and 2) are parallel to the green axes of the postoperative implants (cylinders 4 and 5) and to the expected path of insertion (red cylinder 3). Thus, the implants were accurately inserted into their positions and according to the ideal angle.

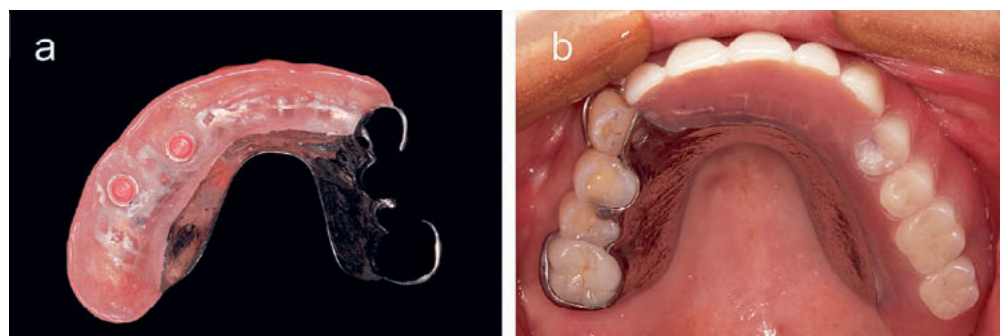


**Fig 7** (a) Final RPD and (b) insertion of the RPD.

Instructions for denture use were provided to the patient, including proper hygiene procedures and follow-up for possible annual relines.

**Discussion**

The present article describes a novel digital technique to ensure parallelism between the path of removable denture insertion and the long axis of the implant using a guide plate designed and fabricated through CAD/CAM.

In theory, implants are placed in the distal extension area and the attachment is used to connect the implant to RPDs to transform the free end into the non-free end, providing retention and stability for traditional RPDs while greatly reducing the non-axial force of the abutments. Implant-retained RPDs can, to some extent, reduce the stress on the alveolar bone under the base plate, the pressure on the alveolar mucosa and the probability of mucosal tenderness. Depending on the implant position and design of the RPD, this technique can also help eliminate the need for unsightly clasps

and improve the arch form if necessary. Compared with implant-supported fixed restorations, the number of implants can be reduced, and the economic burden on patients can be greatly alleviated; however, owing to the lack of unified planning between the design of the RPD and implant insertion, the aforementioned processes can result in many adverse events.

The path of RPD insertion has not been considered fully during implantation, resulting in a significant difference in the path of insertion and axis of implantation<sup>13-15</sup>. Through digital technology, the relevant information on the natural abutment teeth and alveolar bone can be considered comprehensively to design the RPD. In implant-retained RPDs, the implants mainly serve to provide retention and stability. Thus, when designing the axial direction of the implant, it should firstly be considered to be parallel to the insertion path of the removable denture; secondly, the axial direction of the implant should be within the range of available bone volume in the jaw; and finally, it should be coordinated with the position of the opposite dentition. This



can ensure that the path of RPD insertion is parallel to the long axis of the implant to achieve the best clinical outcome: when the RPD is inserted and removed along the direction of the insertion path, the negative and positive components of the implant attachment can move without crossing angles, thus reducing wear between components; the insertion and removal direction of the denture and implant attachment can be unified and the RPD can be passively positioned and removed smoothly without exerting a large lateral force on the natural abutment teeth, which is the most desired outcome when designing and manufacturing an RPD; and abutment tooth preparation and implant surgery can help coordinate the axial direction of the implant and direction of the masticatory forces as much as possible, reducing the unfavourable lateral forces on the implant, thus slowing bone resorption and extending the life of the implant. However, studies with longer follow-up are still needed to confirm this novel technique.

## Conclusion

This article presents a novel method that can help combine restoration-guided implantation with standard RPD design and tooth preparation through digital technology. It is possible to design and manufacture a combined guide plate for guide plane preparation on abutment teeth and for implantation using digital model surveying and alveolar bone analysis.

## Conflicts of interest

The authors declare no conflicts of interest related to this study.

## Author contribution

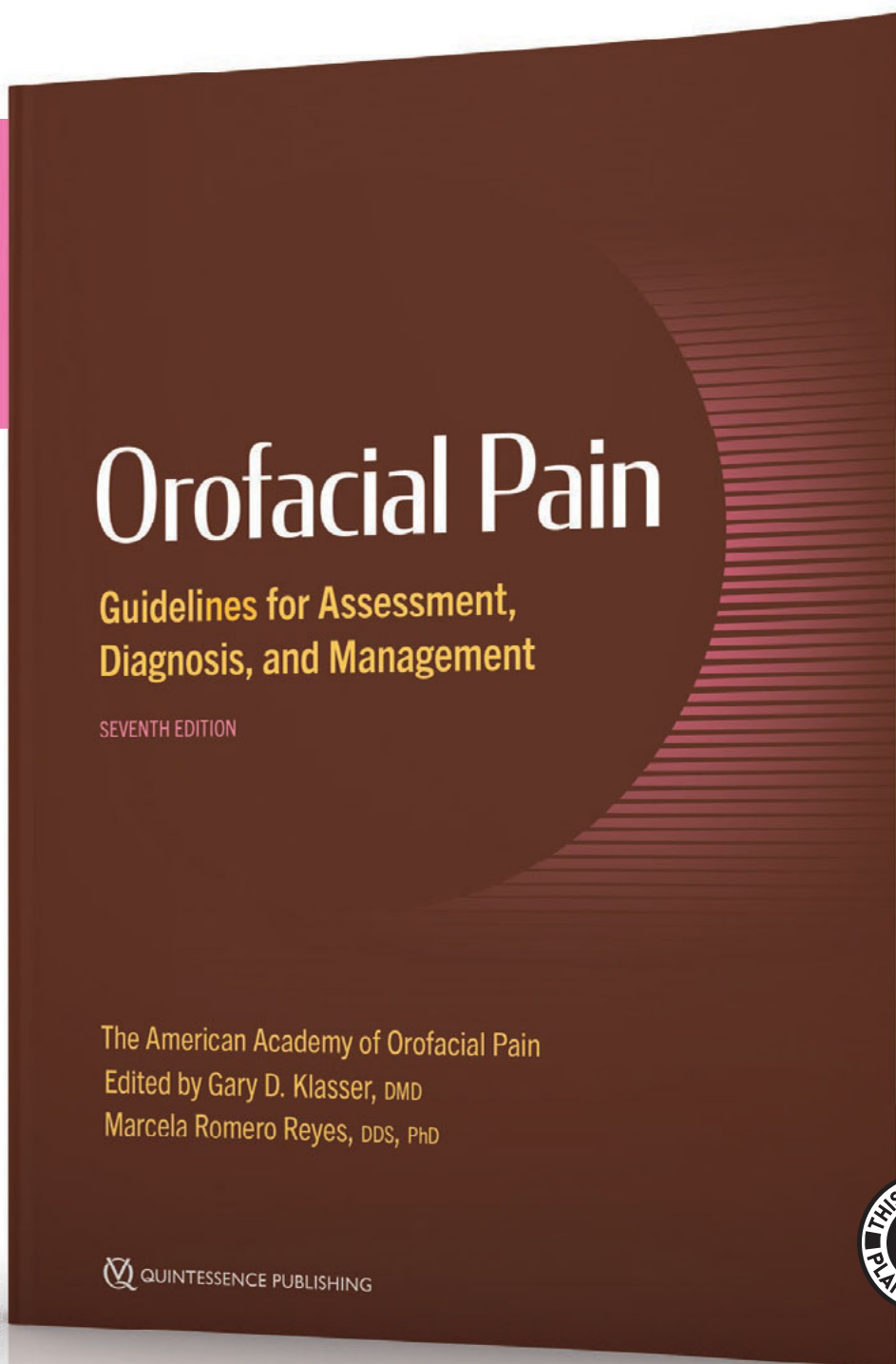
Dr Wan Rong WANG collected the data and drafted the manuscript; Drs Rui XIE and Zhi Hong FENG diagnosed and treated the patient; Drs Li Na NIU and Yi Min ZHAO revised the manuscript. All authors approved the final manuscript.

(Received Nov 07, 2022, accepted Feb 07, 2023)

## References

1. Campbell SD, Cooper L, Craddock H, et al. Removable partial dentures: the clinical need for innovation. *J Prosthet Dent* 2017;118:273–280.
2. Cooper LF. The current and future treatment of edentulism. *J Prosthodont* 2009;18:116–122.
3. De Kok IJ, Cooper LF, Guckes AD, et al. Factors influencing removable partial denture patient-reported outcomes of quality of life and satisfaction: a systematic review. *J Prosthodont* 2017;26:5–18.
4. Giffin KM. Solving the distal extension removable partial denture base movement dilemma: A clinical report. *J Prosthet Dent* 1996;76:347–349.
5. Lee JH, Kim SH, Yoon HI, Yeo ISL, Han JS. Implant-assisted removable prosthetic rehabilitation after distraction osteogenesis in a patient with ameloblastoma recurrence: A case report. *Medicine (Baltimore)* 2019;98:e18290.
6. Baek YW, Lim YJ, Lee JH, Ryu HS. Restoration of a partially edentulous patient with an implant-supported removable partial denture: A case report. *Quintessence Int* 2014;45:307–312.
7. Mijiritsky E. Implants in conjunction with removable partial dentures: A literature review. *Implant Dent* 2007;16:146–154.
8. Gonçalves TM, Campos CH, Garcia RC. Implant retention and support for distal extension partial removable dental prostheses: Satisfaction outcomes. *J Prosthet Dent* 2014;112:334–339.
9. Mijiritsky E, Lorean A, Mazor Z, Levin L. Implant tooth-supported removable partial denture with at least 15-year long-term follow-up. *Clin Implant Dent Relat Res* 2015;17:917–922.
10. Jensen C, Meijer HJA, Raghoobar GM, Kerdijk W, Cune MS. Implant-supported removable partial dentures in the mandible: A 3-16 year retrospective study. *J Prosthodont Res* 2017;61:98–105.
11. Zancopé K, Abrão GM, Karam FK, Neves FD. Placement of a distal implant to convert a mandibular removable Kennedy class I to an implant-supported partial removable Class III dental prosthesis: A systematic review. *J Prosthet Dent* 2015;113:528–533.e3.
12. Phoenix RD, Cagna DR, DeFreest CF. *Stewart's Clinical Removable Partial Prosthodontics*, ed 4. Chicago: Quintessence, 2008.
13. Bural C, Buzbas B, Ozatik S, Bayraktar G, Emes Y. Distal extension mandibular removable partial denture with implant support. *Eur J Dent* 2016;10:566–570.
14. Park JH, Lee JY, Shin SW, Kim HJ. Effect of conversion to implant-assisted removable partial denture in patients with mandibular Kennedy classification I: A systematic review and meta-analysis. *Clin Oral Implants Res* 2020;31:360–373.
15. Tribst JP, de Araújo RM, Ramanzine NP, et al. Mechanical behavior of implant assisted removable partial denture for Kennedy class II. *J Clin Exp Dent* 2020;12:e38–e45.

# OUT WITH THE OLD, IN WITH THE NEW!



Gary D. Klasser | Marcela Romero Reyes (Eds)

## Orofacial Pain

Guidelines for Assessment, Diagnosis, and Management

7<sup>th</sup> Edition, 368 pages

ISBN 978-1-64724-037-0

€68

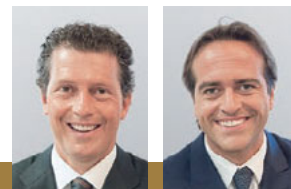
This new edition is the first to be released since orofacial pain was recognized as the 12th dental specialty by the American Dental Association. Although the structure resembles previous editions, including up-to-date evidence-based assessment, diagnosis, and management of orofacial pain conditions, significant changes have been made. The most recent International Classification of Diseases, Eleventh Edition (ICD-11) classification system is used, featuring new diagnostic codes and tables mapping differences between ICD-10 and ICD-11. Other revisions are the inclusion of cervical spinal disorders and associated headaches; extracranial and systemic causes of orofacial pain; greater emphasis on headache pathophysiology and management updates; and "newer trends" related to electronic cigarettes/vaping and the SARS-CoV-2 global pandemic.



# OPPORTUNITIES FOR SUCCESS



alessandroagnini  
andreaagnini  
CO-AUTHORS  
robertoapponi  
giuliabenedetti



Alessandro Agnini | Andrea M. Agnini

## The Digital Revolution 2.0

Clinico-Technical Applications in Daily Practice

448 pages, 1,240 illus


ISBN 978-88-7492-097-6

€179


## THE DIGITAL REVOLUTION 2.0

CLINICO-TECHNICAL APPLICATIONS  
IN DAILY PRACTICE



 QUINTESSENCE PUBLISHING



 QUINTESSENCE PUBLISHING

Technology has irreversibly changed our profession, ushering in a historical period full of challenges and opportunities. Leveraging digital tools to diagnose, design, plan, motivate, and execute corrective therapies is crucial for success in today's highly competitive business environment. Planning investments, creating partnerships, facing and overcoming the learning curve, involving the team, and making technology a daily routine by stepping out of one's comfort zone are just some of the challenges for success in contemporary dentistry that are covered in this book.



[www.quint.link/revolution](http://www.quint.link/revolution)



[books@quintessenz.de](mailto:books@quintessenz.de)



+49 (0)30 761 80 667

 QUINTESSENCE PUBLISHING

